



Virginia Commonwealth University
VCU Scholars Compass

Theses and Dissertations


Graduate School

2016

Non-Conventional Approaches to Syntheses of Ferromagnetic Nanomaterials

Dustin M. Clifford

Follow this and additional works at: <https://scholarscompass.vcu.edu/etd>

 Part of the [Atomic, Molecular and Optical Physics Commons](#), [Condensed Matter Physics Commons](#), [Design of Experiments and Sample Surveys Commons](#), [Inorganic Chemistry Commons](#), and the [Materials Chemistry Commons](#)

© The Author

Downloaded from

<https://scholarscompass.vcu.edu/etd/4205>

This Dissertation is brought to you for free and open access by the Graduate School at VCU Scholars Compass. It has been accepted for inclusion in Theses and Dissertations by an authorized administrator of VCU Scholars Compass. For more information, please contact libcompass@vcu.edu.

**Non-Conventional Approaches to Wet-Chemical Syntheses of Ferromagnetic
Nanomaterials**

A dissertation submitted in partial fulfillment of the requirements for the degree of Doctor of
Philosophy at Virginia Commonwealth University.

by

Dustin Michael Clifford

B.S., Baylor University, May 2007

Director: Everett E. Carpenter

Ph. D., Director of Nanoscience and Nanotechnology Program

Virginia Commonwealth University

Richmond, VA

May, 2016

Acknowledgements

I wish to thank many people for their continued support over the last four years at VCU. First, my fiancé for her relentless support and encouragement throughout the years of whom without, I could not have accomplished the work of this dissertation. Also I am very thankful to my family members who have all given their support. A special thanks goes to my advisor at VCU, Prof. Everett Carpenter, who has been a great mentor throughout my Ph.D. program. I'd also like to thank my colleague and friend, Dr. Carlos Castano, for his collaborative efforts, helpfulness and thoughtful critiques. Finally, I owe much gratitude to Dr. Dmitry Pestov and Prof. Massimo Bertino for their shared insight and time given in numerous instrumentation training sessions.

Table of Contents

List of Figures of	viii
List of Tables	xvi
Abstract.....	xvi
Chapter 1: Introduction	1
1.1 Introduction.....	2
1.2 Overview.....	2
1.3 Types of Magnetism.....	4
1.4 Ferromagnetism.....	4
1.4.1 Magnetic Domains.....	5
1.4.2 Anisotropy Energy.....	6
1.5 Magnetic Properties.....	8
1.5.1 Soft Magnet Properties.....	9
1.6 Nanoscale Magnetism.....	10
1.7 Soft Magnetic Materials.....	12
1.7.1 Fe, Co and FeCo Alloy.....	12
1.7.2 Nanocomposites and Amorphous Alloys.....	13
1.8 Polyol Process.....	15
1.9 High Throughput Experimentation.....	16
1.10 Continuous Flow Chemistry.....	17
1.11 Summary of Objectives.....	18
Chapter 2: Characterization Techniques.....	19

2.1 Introduction.....	20
2.2 X-Ray Diffraction (XRD).....	20
2.2.1 High Temperature X-Ray Diffraction (HT-XRD)	22
2.3 Vibrating Sample Magnetometry (VSM).....	23
2.4 Transmission Electron Microscopy (TEM).....	24
2.4.1 Selected Area Electron Diffraction (SAED).....	25
2.4.2 Dark-Field Microscopy (DF-TEM)	26
2.4.3 Electron Energy Loss Spectroscopy (EELS).....	27
2.5 Scanning Electron Microscopy (SEM).....	27
2.5.2 Focused Ion Beam.....	28
Section 1: High Throughput Experimentation: Polyol Process	29
Chapter 3: Polyol Synthesis of Cobalt Ferrite and Nanomaterials.....	30
3.1 Overview.....	31
3.2 Introduction.....	31
3.3 Experimental.....	32
3.3.1 Characterization.....	33
3.4 Results and Discussion.....	35
3.5 Conclusion.....	48

Chapter 4: Synthesis of High Aspect Ratio $\text{Fe}_1\text{Co}_{1-x}$ Nanostructures.....	49
4.1 Overview.....	50
4.2 Introduction.....	50
4.3 Experimental.....	51
4.3.1 FeCo Precursor Solution Preparation.....	51
4.3.2 Synthesis of FeCo MALCs.....	53
4.3.Characterization.....	53
4.4 Results and Discussion.....	55
4.5 Conclusion.....	66
Chapter 5: Size control of $\text{Fe}_x\text{Co}_{1-x}$ Chains using Nucleation Agents by DOE.....	68
5.1 Overview.....	69
5.2 Introduction.....	69
5.3 Experimental.....	72
5.3.1 Characterization.....	73
5.4 Results and Discussion.....	75
5.4.1 Mechanism for Assembly of FeCo Chains.....	87
5.4.2 Reaction Parameters and Responses.....	88
5.4.3 Control of FeCo Phase.....	88

5.4.4 Control of Fe_1Co_{1-x} Chain Morphology.....	89
5.4.5 Control of Fe_1Co_{1-x} Crystallite Size.....	89
5.4.6 Correlation of Physical and Magnetic Properties.....	90
5.5 Conclusion.....	91
Chapter 6: Synthesis of High Aspect Ratio Cobalt Ferrite Nanostructures.....	92
6.1 Overview.....	93
6.2 Introduction.....	94
6.3 Experimental.....	94
6.3.1 Precursor A: Oxidation of Triethylene Glycol.....	94
6.3.2 Precursor B: Dissolution of Metallic Salts.....	95
6.3.3 Synthesis of Cobalt Ferrite Micropillars.....	95
6.3.4 Characterization.....	95
6.4 Results and Discussion.....	96
6.5 Conclusion.....	107
Section 2: Continuous Flow: Polyol Process and Aqueous Reduction.....	108
Chapter 7: Co Nanoparticle Synthesis in a Microfluidic Reactor	109
7.1 Overview.....	110
7.2 Introduction.....	110

7.3 Experimental.....	111
7.3.1 Synthesis of Co Nanoparticles in Continuous Flow.....	112
7.3.2 Characterization.....	113
7.4 Results and Discussion.....	115
7.5 Conclusion.....	120
Chapter 8: FeCo Nanomaterial Synthesis in Continuous Flow.....	122
8.1 Overview.....	123
8.2 Introduction.....	123
8.3 Experimental.....	123
8.3.1 Synthesis of FeCo in Continuous Flow.....	125
8.3.2 Characterization.....	125
8.4 Results and Discussion.....	126
8.5 Conclusion.....	130
Chapter 9: Summary.....	132
References.....	136
Vita.....	140

List of Figures

Chapter 1.

Figure 1.1. Scheme depicting the types of magnetism and their representative spin moments in the direction of an applied field.

Figure 1.2. Ferromagnetic domains represented within crystalline grain boundaries (thick lines) of a poly-crystal in the absence of an applied field or mechanical stress. Modified from ref. (3).

Figure 1.3. Hysteresis loop of a typical ferromagnet showing basic properties of H_c , coercivity, M_r , remanence and M_s , saturation magnetization. Modified from ref. (5).

Figure 1.4. Partial hysteresis curve of a soft ferromagnet with virgin (black, dashed) and demagnetization (red, solid) curve and near zero-field region indicating magnetic properties

Figure 1.5. General relationship between particle size and coercivity indicating both the superparamagnetic (SPM) and ferromagnetic (FM) region

Figure 1.6. FeCo alloy body-centered cubic lattice structure representation for an ordered 50:50 Co:Fe (at. %). Fe atoms (red) and Co atoms (blue).

Figure 1.7. Co-Fe phase diagram with several phase transformations of a 68 % at. Co composition highlighted as well as 40 % at. Co transformation from B2 to A2 above 700 C. (modified from ref [6]).

Figure 1.8. Permeability and saturation magnetization relationships for a variety of premiere soft ferromagnetic materials with FeCo alloys shown. Modified from ref [11].

Figure 1.9. Generalized mechanistic route for polyol reductions using ethylene glycol and a divalent metallic precursor. First dehydration to aldehyde and subsequent oxidation to diacetyl and reduction to metal.

Chapter 2.

Figure 2.1. Scheme of incident and diffracted x-rays in a substrate depicting the components of Bragg's Law.

Figure 2.2. General schematic of VSM sample powder mounted inside chamber showing orientation to measuring field and pick up coils.

Figure 2.3. Scheme of various electron interactions in a TEM sample from high energy **electrons**.

Chapter 3.

Figure 3.1. Scheme of the Argonaut Process Synthesizer (a) used to perform the FeCo and CFO nanomaterial syntheses via polyol process. Photograph of a 5-reaction vessel bank on process synthesizer with in-process polyol reactions shown (b).

Figure 3.2. Representative XRD patterns of FeCo (green triangles) and Cobalt ferrite (black triangles) nanomaterial composite synthesized by polyol-process via high throughput format with CFO-rich in (a) and FeCo-rich in (b).

Figure 3.3. TEM image of an FeCo and cobalt ferrite composite (a) with SAED shown indicating both phases (b) and dark-field cone illumination of cobalt ferrite particle (c) and dark-field cone-illumination of FeCo particles along with cobalt ferrites (d).

Figure 3.4. SEM micrographs of FeCo nanomaterial (a) and FeCo/CFO (b) complementing TEM images from figure 3.3 (d). Cobalt ferrite particles are identified with red arrows in (b).

Figure 3.5. TEMs of increasing compositions of FeCo % and increasing saturation magnetizations from left to right of FeCo/CFO nanomaterial.

Figure 3.6. BFTEM image (c) with corresponding EFTEMs of C, Co and Fe colored maps in (a, b and d) and EELS spectrum showing energies from 560-1000 eV in (e) with labelled Fe and Co edges at around 708 and 780 eV respectively.

Figure 3.7. EF-TEM of typical CFO-rich sample showing distribution of Fe (red) and Co (blue) maps in EFTEM insets (right).

Figure 3.8. X-Y plot of saturation magnetization versus coercivity indicating distinct regions of plots based on total reaction volume.

Figure 3.9. Variation of [OH] with [Metal] and M_s (emu/g) showing $[OH] \approx 3$ and $[Metal] \approx 0.1$ to produce highest saturation values of FeCo-rich samples. Range bars shown.

Figure 3.10. Metallic salt precursor premixing with saturation magnetization in (a) and variation in [OH] with M_s (emu/g) with precursor premixing and condensation absorbent presence in (b). [OH] is color-coded with symbols in (a) and (b). Std. error bars shown.

Figure 3.11. Maximum precursor premixing temperature ($^{\circ}C$) in (a) and premixing time (minutes) in (b) with M_s (emu/g). Symbols shown for precursor premixing temperatures

Figure 3.12. Variation of Rx time (mins) with M_s (emu/g) showing shorter reaction times around 15 minutes ideal for producing highest saturation values of FeCo-rich samples. Condensation absorbent presence gives M_s enhancement as well. Std. error bars shown.

Figure 3.13. Relationship between FeCo alloy (determined by XRD) with magnetic properties of M_s (emu/g) and H_c (kOe).

Figure 3.14. M_s (emu/g) versus H_c (Oe) of >200 reactions (a) indicating the overall magnetic property distribution between FeCo-rich (b) and CFO-rich (c) samples as well as morphological difference.

Chapter 4.

Figure 4.1. Reaction vessel (Argonaut process synthesizer) scheme used to produce magnetically aligned linear FeCo chains via polyol via high throughput process synthesis. Oscillating permanent magnet shown provides the external field as well as vertical magnet stirring.

Figure 4.2. SEM image of FeCo MALCs (a) with chain diameter distribution shown in (b). Average chain diameter was about 220 nm for the sample shown in (a).

Figure 4.3. SEMs showing tangential cross-sections by FIB displaying the various crystallite orientations and microstructure within the FeCo MALCs. MALCs are shown consisting of segmented FeCo particles rather than continuous or high-aspect ratio FeCo crystallites.

Figure 4.4. BF-TEM image of FeCo MALCs in (a) and corresponding SADP in (b) indicating the (110), (200) and (211) planes of FeCo bcc.

Figure 4.5. XRDs of magnetically oriented FeCo MALCs with respect to the incident X-ray path, parallel to x-ray path in (a) and perpendicular to x-ray path in (b). Both orientations provide similar peak position and intensities indicating low to no intra-particle anisotropy.

Figure 4.6. VSM hysteresis curves acquired at 300 K (red/square), 1000 K (light blue vertical line), 300 K after anneal (blue/triangle) and separate sample prep of same batch at 50 K (yellow/diamond) of FeCo MALCs.

Figure 4.7. Thermomagnetic analysis of mass susceptibility χ_{mass} measured from RT to 1000 K of FeCo MALCs with magnetization steps indicating presence of two FeCo compositions, ≈ 68 and ≈ 40 atomic % Co. (Refer to Co-Fe phase diagram for highlighted corresponding phase changes in Ch. 1) Red circle $\approx 770\text{K}$ indicates unknown phase change.

Figure 4.8. HT-XRD waterfall plot of diffractograms acquired in order of increasing temperatures at 25 C, 225 C, 325 C, 500 C, 600 C, 727 C and 25 C (cooled) indicating formation of cubic FeO (wustite) at about 500 C.

Figure 4.9. SEM images of FeCo continuous microwires formed from FeCo MALCs after annealing at 1000 K for 30 minutes in (a) and FeO crystallites formed on surface in (b).

Figure 4.10. EDS point analyses of a FeCo microwire in (a), with EDS results in table (b) and of a FeO crystallite in (c) with EDS results in (d) showing varying O content.

Figure 4.11. SEM images of a single FeCo MALC synthesized in an external field (a) and FeCo particles synthesized with no external magnetic field in (b). Both samples were synthesized from the same experimental conditions.

Figure 4.12. EDS data taken of FeCo MALCs indicating an average composition $\approx \text{Fe}_{58}\text{Co}_{42}$.

Chapter 5.

Figure 5.1 A representation of a vessel from the Surveyor Argonaut Process Synthesizer: a suitable tool for combinatorial chemistry studies as well as DOEs.

Figure 5.2: Various nucleation agents of Ag, Ru and Pt at low (10⁻⁴) and high (10⁻²) [Seed]/[Metal] ratios and their effect on FeCo morphologies taken by SEM.

Figure 5.3. A representation of the (110) plane of FeCo alloy by XRD with profile fitting showing the FWHM value determined using HighScorePlus[®] software. These peak analyses were used for the average crystallite size determination.

Figure 5.4. XRDs showing 100 % FeCo (a) and combination of FeCo, Co (fcc) and CoFe₂O₄ (CFO) (b). These phases represent those synthesized throughout the DOE.

Figure 5.5. Chart showing relative abundances of morphologies observed in the DOE study for pure phase FeCo bcc.

Figure 5.6. Representative morphologies synthesized throughout the DOE with nanochains (less than 100 nm) shown in (a) and (b), Ag-seeded chains in (c), larger diameter, non-seeded chains in (d), chains and particle (red arrows/ellipsoidal stellated structures) (Co) mixtures in (e), C-coated

chains in (f), spheres (CoFe₂O₄) in (g) and particles in (h). All morphologies are 100 % FeCo unless secondary phase is noted.

Figure 5.7. TEM images of Ag-seeded FeCo chains in (a) and (e) and Ag-seeded nanochains in (b-d) and (f) and (g) with SAED indicating FeCo bcc alloy and (110) crystallites illuminated using dark-field cone-illumination in inset of (h).

Figure 5.8 Response surface models for % FeCo alloy composition (by XRD) in (a), mean crystallite size (by Scherrer) in (b) and chain formation quality (by SEM) in (c) and (d) all constructed using most significant p-values of independent variables or transformations between two significant variables.

Figure 5.9. [Ag]/[Co] vs. mean chain diameter (nm) (upper plot) for all FeCo alloy morphologies with corresponding [Ag]/[Metal] averages (lower plot) with std. error bars shown.

Figure 5.10. Various morphologies with representative MxH curves showing saturation magnetization values shown with chain (Δ), chain (no Ag seed), (\blacktriangle), chain + particle (\blacklozenge), particle (\blacklozenge), nanochain (\square), chain (carbon coated) (\odot) and sphere (\bullet).

Figure 5.11. Thermogravimetric analysis (black curve) coupled to FTIR absorbance spectra (TGA-FTIR) of carbon-coated chain sample in (a) and nanochain sample in (b) showing the difference in carbon content by mass loss.

Figure 5.12. Elliptical plots (90 % coverage) for FeCo alloy morphologies against physical (mean diameter (nm) and crystallite size (nm) and ratio) and magnetic properties of (H_c (Oe) and M_s (emu/g).

Figure 5.13: ICP results (normalized to nominal Co and Fe concentrations (50:50 molar) of reaction solution aliquots sampled at various time points during the reaction process.

Chapter 6.

Figure 6.1. XRD of as-synthesized micropillar sample indicating cobalt ferrite phase presence in (a) as compared with ref. scan (pdf: 01-079-1744) in (b).

Figure 6.2. TEM images of CFO micropillar (filtered 0.5 μ) shown in (a), (b) and (d) with SAED indicating CFO phase in (e) and SEM images in (c) and (f). Shadowgram given in inset of (d) with average particle diameter at 13 ± 9 nm (filtered with most magnetically responsive particles removed).

Figure 6.3. Hysteresis curves of CFO micropillars (filtered-0.5 μ and immobilized via formvar) indicating low- H_c and M_s of 33 and 36 emu/g when magnetically oriented perpendicular and parallel to the external measuring field all acquired at 300 K (filtered with most magnetically responsive particles removed).

Figure 6.4. UV-vis spectra overlay of magnetically oriented CFO MPs. Parallel (yellow), 45 degrees (green), perpendicular (red) and no orientation (black-dotted) of CFO MPs suspended in R-OH (filtered with most magnetically responsive particles removed).

Figure 6.5. Images showing light transmission with two magnet orientations of diluted and concentrated CFO micropillars suspended in various short chain alcohols (R-OH). Dilute CFO MPs in (a) and (b) with no magnet presence for dilute CFO MPs in (c) and concentrated CFO MPs in (d) and (e) (all samples shown were filtered with most magnetically responsive particles removed).

Figure 6.6. Optical microscope image taken of CFO micropillars (unfiltered, as-synthesized) showing the distinct high-aspect ratio morphology as well as a larger size distribution as compared with TEM and SEM images shown in figure 6.2.

Figure 6.7. TEM images at low magnification (a) and high-resolution (b) showing the nanostructured CFO particles of a single CFO micropillar. HR-TEM in (b) shows the (111) plane with d-spacing $\approx 0.48\text{nm}$ (unfiltered, as-synthesized).

Figure 6.8. Hysteresis overlays at 300, 250 and 200 K demonstrating relative exponential increase of coercivity at lower temperatures of the unfiltered, as-synthesized CFO MPs.

Figure 6.9. Reduced remanence curves, mIRM/mDCD (black/red), with delta M plots (green) overlaid using 2 second delay at 100 Oe steps (300 K) in (a), 10 sec delay at 300 K in (b), and 10 second delay at 320 K (c) performed on free CFO MP powder sample. Delta M indicates positive or negative particle-particle exchange interactions (sample was unfiltered, as-synthesized).

Chapter 7.

Figure 7.1. Microreactor assembly used to perform the continuous flow synthesis of cobalt nanoparticles.

Figure 7.2: The reaction scheme if given for the EHAS system used in this work to produce Co NPs.

Figure 7.3. XRD of as-synthesized Co NPs showing three phases, Co fcc, Co hcp and CoO.

Figure 7.4. BTTEM of Co NPs (as-synthesized) via continuous flow using the EHAS system (a-f) with inset of (d) showing Co EF-TEM.

Figure 7.5. XPS spectra of as-synthesized Co NPs indicating Co^{2+} around 786 eV rather than Co^0 attributed to an oxide layer on all particles.^b

Figure 7.6. Hysteresis curve of as-synthesized Co NPs possessing saturation magnetization of 125 emu/g and H_c of 170 Oe taken at 300 K.

Chapter 8.

Figure 8.1: Photo of the involved continuous flow (CF) reactor set-up shown with systolic and peristaltic pumps (top), mechanical stirrer (top-left), reaction vessel (far left-center) and product vessel/round bottom flask (left-center).

Figure 8.2: Photo of round bottom flask used in the continuous flow synthesis of FeCo/cobalt ferrite product with input tube (left) shown carrying synthesized nanomaterial to a holding vessel with the second tube (right) generating the partial vacuum.

Figure 8.3: XRD showing maximum FeCo % of 20 % and 80 % CFO possible via CF polyol synthesis using 1.75 mL/min flow rate of hydroxide precursor and 0.6 mL/min metal precursor.

Figure 8.4: SEMs of FeCo/cobalt ferrite composites using 18 M OH with flow rates at 0.4 in (a), 0.6 in (b), 0.8 in (c) and 1.0 mL/min in (d) with metal precursor flow rate kept constant at 0.6 mL/min. Scale bar are 10 μ m for all.

Figure 8.5: Hysteresis curve of 20 % FeCo/ 80% CFO mixture produced by CF which had an M_s of around 120 emu/g and H_c of about 500 Oe.

List of Tables

Chapter 1.

Table 1.1. Some applications and corresponding magnet types and their elements

Table 1.2. Demagnetizing factors N_D (SI) and respective internal magnetization direction. Modified from ref. (5).

Chapter 5.

Table 5.1. Effect summaries for all responses in the RSMs shown in figure 5.8 with p-values given for each variable (source) or transformation with other variables.

Table 5.2: Correlation probabilities (p-values) for all analyzed responses in the DOE.

NON-CONVENTIONAL APPROACHES TO WET-CHEMICAL SYNTHESSES OF FERROMAGNETIC NANOMATERIALS

By Dustin M. Clifford, Ph.D.

A dissertation submitted in partial fulfillment of the requirements for the degree of Doctor of Philosophy at Virginia Commonwealth University.

Virginia Commonwealth University, 2016

Director: Dr. Everett E. Carpenter

Professor of Chemistry

The work of this dissertation is centered on two non-conventional synthetic approaches to ferromagnetic nanomaterials: high-throughput experimentation (HTE) (polyol process) and continuous flow (CF) synthesis (aqueous reduction and the polyol process). HTE was performed to investigate phase control between $\text{Fe}_x\text{Co}_{1-x}$ and $\text{Co}_{3-x}\text{Fe}_x\text{O}_y$. Exploration of synthesis limitations based on magnetic properties was achieved by reproducing $M_s=210$ emu/g. Morphological control of $\text{Fe}_x\text{Co}_{1-x}$ alloy was achieved by formation of linear chains using an H_{ext} . The final study of the $\text{Fe}_x\text{Co}_{1-x}$ chains used DoE to determine factors to control $\text{Fe}_x\text{Co}_{1-x}$, diameter, crystallite size and morphology. $[\text{Ag}]$ with $[\text{Metal}]$ provide statistically significant control of crystallite size. $[\text{OH}]/[\text{Metal}]$ predict 100 % $\text{Fe}_x\text{Co}_{1-x}$ at > 30 . To conclude section 1, a morphological study was performed on synthesis of $\text{Co}_{3-x}\text{Fe}_x\text{O}_y$ using the polyol process. $\text{Co}_{3-x}\text{Fe}_x\text{O}_y$ micropillars were synthesized at various sizes. The close proximity of the particles in the nanostructure produced an optical anisotropy and was magnetically induced which is evidence for the magneto-birefringence effect.

The second non-conventional synthetic approach involves continuous flow (CF) chemistry. Co nanoparticles ($M_s=125$ emu/g) were newly synthesized by aqueous reduction in a microreactor and had 30 ± 10 nm diameter and were produced at >1 g/hr, a marker of industrial-scale up viability. The final work was the CF synthesis of Fe_xCo_{1-x} . The Fe_xCo_{1-x} was synthesized with limitation to the composition. The maximum Fe_xCo_{1-x} phase composition at 20 % resulted from the aqueous carrier solvent triggering oxide formation over Fe_xCo_{1-x} .

Chapter 1. Introduction

1.1 Introduction

This dissertation is aimed at exploration of the soft ferromagnetic nanomaterials of Co, FeCo alloy as well as hard ferrimagnetic cobalt ferrite via wet-chemical methods involving non-conventional formats. It is perhaps most suitable for industrial engineers who desire to better control the synthesis of useful ferromagnetic nanomaterials or for the inorganic synthetic chemist wanting to further understand the magnetic properties. For the material scientist, there is a strong focus on the characterization of the nanomaterials synthesized. This work ranges from elucidation on several subtle synthetic controls between Fe-based phases to demonstrations of continuous production using flow chemistry processes. To better understand and further appreciate the magnetic nanomaterials synthesized in this work, a general understanding of magnetism, (classifications, applications and types) as well as magnetism at the nanoscale and the wet-chemical synthesis routes is essential. These topics will be discussed in detail within this chapter.

1.2 Overview

Ferromagnetic nanomaterials are of current interest due to their property enhancements at the nano- and sub-micron scale lengths. These materials are generally classified as hard, (permanent magnets) or soft, (electromagnetic cores) and intermediate (magnetic data storage) which depend on the elemental composition, crystallography and the microstructure after thermal treatments. Hard ferromagnets possess an overall high resistance to demagnetization by an external field (H_{ext}) aligned antiparallel while soft ferromagnets have low resistance to demagnetization and are easily magnetized in the field direction.¹ Hard ferromagnets maintain a high spontaneous magnetization (remanence), or internal magnetic field, in the absence of an external field, and have the ability to magnetize objects in their surroundings. The magnetization

arises from spontaneously magnetized magnetic domains which will be discussed later in this chapter. Soft ferromagnets, on the other hand, commonly possess a smaller magnetization in the absence of an external field. The terms hard and soft are generalities which are intended to appease a wide audience of magneticians whom are typically interested in specific properties toward select applications. Table 1.1 below contains the two main magnet classifications (hard and soft), along with their general applications and a few magnetic material types.

Table 1.1. Some applications and corresponding magnet types and their elements.

<i>Classification</i>	<i>Soft Magnets</i>	<i>Intermediate</i>	<i>Hard Magnets</i>
<i>Application</i>	I-Motors, Reed Switches, MRI Contrast Enhancing Agents, Transformer Cores, Drug Delivery	Hard Disk Drives for recording devices, Magnetic tape (credit cards), Badges	PM-Motors, Permanent Magnets, Most Electronics and Appliances
<i>Commonly Used and some Potential Materials</i>	Fe, Co, Ni and their alloys, few Oxides of Fe and other Late-Transition Metal (LTM) Oxides, Fe-Si, Fe-Si-B	CoCr, CrO ₂ , carbides of Fe and Co	RE (rare earth) – Magnets, (NdFeB, SmCo), Ferrite, AlNiCo, Carbides of Co

As shown in Table 1.1, soft magnets are commonly based on Fe and Co and these ferromagnetic elements are required when demanding magnetic or thermal properties are required.¹ In most cases, soft magnetic nanomaterials of these compositions must undergo grain alignment, compaction and annealing similar to the processing of hard magnetic nanomaterials.² In this work, exploration of the magnetic properties of FeCo and cobalt ferrite is performed and these properties will be compared with the wet chemistry in which they were synthesized Co, FeCo

and the ferrimagnetic oxide, CoFe_2O_4 , may be classified as magnetically soft for the former two and hard for the latter; the former routinely possess high M_s coupled with low H_c (100-200 Oe) and moderate magnetic permeability (μ_m) depending on the composition and the latter possess low M_s but moderate H_c (≈ 1000 Oe).⁴⁻⁹

1.3 Types of Magnetism

There exists several types of magnetism and examples are shown in figure 1.1. Materials are paramagnetic if atoms have unpaired electrons which present intrinsic magnetic moments that align in the direction of an external field. These atomic moments are not ordered and the observed magnetization is generally weak as a result. Molecules and transition metals exhibiting paramagnetism at room temperature are NO, O_2 , Pd and Pt and above a certain critical temperature, Ni, Fe and Co.¹ Diamagnetism is similar to paramagnetism, with the exception that the spin moments are aligned anti-parallel to the applied field.

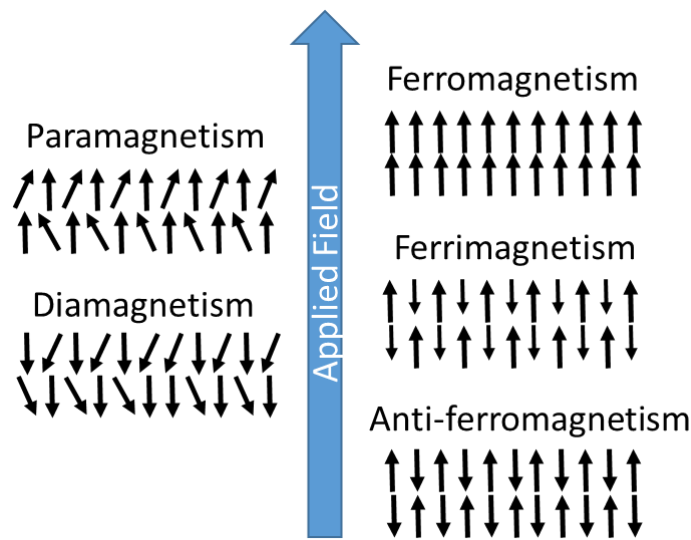


Figure 1.1. Scheme depicting the types of magnetism and their representative spin moments in the direction of an applied field.

In other words, paramagnets are attracted in the direction of an external field and diamagnets are repelled in the direction of an external field.

1.4 Ferromagnetism

Ferromagnetism is a form of cooperative magnetism that originates from the energy of exchange interaction between atomic moments. A representation of ferromagnetism along with ferrimagnetism and anti-ferromagnetism are given in figure 1.1. The exchange energy generates parallel alignment of electron spins in the direction of an applied field resulting in a spontaneous magnetization. The magnetization remains even after the external field is removed and the magnitude of this magnetization is known as remanence. Elements exhibiting ferromagnetic order above room temperature are the late transition metals of Fe, Co, Ni while elements from the lanthanide series Gd, Tb, Dy, Ho, Er and Tm and the actinide series, Cf, have ferromagnetic ordering at lower temperatures.³ Antiferromagnets have a net cancellation of moment because adjacent atomic moments in the sub-lattices are aligned anti-parallel. Ferrimagnets have similarly antiparallel-aligned atomic moments but the net moment from one sub-lattice is of different magnitude thus an overall net moment is observed.

1.4.1 Magnetic Domains

Atomic moments align parallel in a ferromagnet which act to reduce the exchange interaction energy. This alignment creates a magnetic field and subsequently increases the magnetostatic energy, otherwise known as the demagnetization energy or demagnetization field. The increase in magnetostatic energy results in formation of ferromagnetic domains, or regions of inter-atomic moment alignment, where the domains align anti-parallel to one another. The domains are spontaneously magnetized in orientations with respect to neighboring domains.

Below, figure 1.2 depicts the anti-parallel alignment of magnetic domains within a

polycrystalline particle in the absence of an applied field or stress.⁴ The magnetic domains arise due to unpaired electrons of unfilled orbitals where the electron spins are aligned parallel as a result from exchange interaction, a topic discussed later in this chapter.³

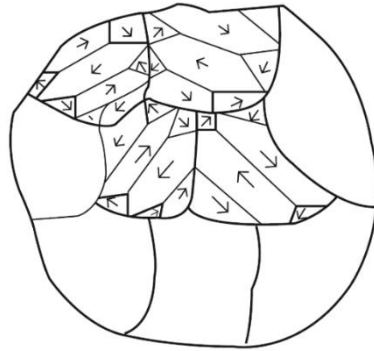


Figure 1.2. Ferromagnetic domains represented within crystalline grain boundaries (thick lines) of a poly-crystal in the absence of an applied field or mechanical stress. Modified from ref. (3).

1.4.2 Anisotropy Energy

Several anisotropy energies exist in magnetic solids. When considering the interactions within a ferromagnet, other than the exchange interaction, it is important to note that the anisotropies originate from multiple sources such as crystallinity, shape, surface, or stress. The crystalline anisotropy, or magnetocrystalline anisotropy, is dependent on the crystal structure of the magnetic material in units of energy density (energy per volume). Spin-orbit coupling between atoms induces a preferred crystallographic magnetization direction. Magneto crystalline anisotropy depends on the elements and their periodic arrangements within each sub-lattice. Materials containing crystallites of elements with high magnetocrystalline anisotropy often possess hard properties and will maintain internal magnetization. Shape does not affect magnetocrystalline anisotropy and it is proportional to coercivity making elements with high

magnetocrystalline anisotropy attractive candidates for permanent magnet synthesis. As mentioned previously the magnetocrystalline anisotropy is directionally dependent as the magnetization along the easy-axis gives the minimum magnetocrystalline energy (MAE) for systems with uniaxial symmetry. Cubic systems may possess equal MAE in several directions due to symmetry but with lower values in comparison. For example Fe and Ni possess cubic anisotropies while Co (hcp) possesses an increased uniaxial anisotropy along the c-axis.⁵ Shape anisotropy, the other most important anisotropy in magnetic nanomaterials has potentially the greatest effect on coercivity or magnetic hardness. Magnetostatic energies drive the mechanism in shape anisotropy and different shapes have different demagnetizing factors with a few basic shapes given below in Table 1.2.⁶

Table 1.2. Demagnetizing factors N_D (SI) and respective internal magnetization direction. Modified from ref. (5).

<i>Shape</i>	<i>Direction</i>	N_d
<i>Plane</i>	perpendicular	1
<i>Plane</i>	parallel	0
<i>Cylinder (l/d) = 1</i>	parallel	0.27
<i>Cylinder (l/d) = 5</i>	parallel	0.04
<i>Long Cylinder</i>	parallel	0
<i>Sphere</i>	n/a	1/3

The higher the demagnetizing factor, (N_D), the greater the magnetostatic energy within the single crystal magnet.

1.4 Magnetic Property Measurement

Hysteretic measurements, or M-H curves, are required in order to determine and evaluate the extrinsic and intrinsic properties of a ferromagnet. A hysteresis loop for a typical ferromagnet is shown below in figure 1.3.⁶

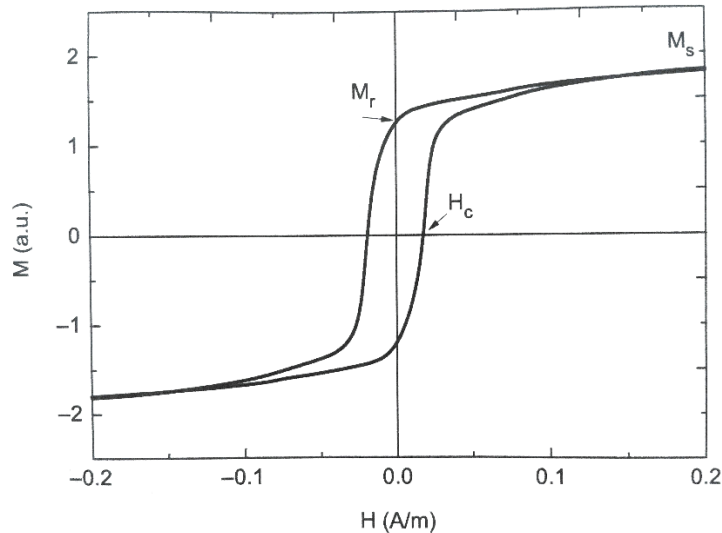


Figure 1.3. Hysteresis loop of a typical ferromagnet showing basic properties of H_c , coercivity, M_r , remanence and M_s , saturation magnetization. Modified from ref. (5).

Coercivity, H_c , is an extrinsic property which relates to the magnetic hardness of a material, that is, the larger the coercive field, the harder the magnet. Saturation magnetization is achieved in a sufficiently high external field where practically all spins are aligned parallel in the direction of the measuring field. This is observed as a plateau near the hysteresis loop closure at high field. The external field is reversed and the M measurement is resumed to saturate the material in the opposite direction in quadrant III. Remanence, M_r , is the magnetization of the material at $H_c = 0$ after saturation. In general, the higher the M_r , the higher the magnitude or measure of the spontaneous magnetization of a permanent magnet. Remanence values are intended to describe the magnetic behavior of a material after a field has been applied. It can be measured in a variety of ways. One way is by taking thermoremanent magnetization curves such

as an isothermal remanent magnetization curve (IRM) and a dc demagnetization curves (DCD). These measurements techniques are discussed in further detail in chapter 2.

1.4.1 Soft Magnet Properties

Soft magnets possess low coercivity values and high saturation magnetization values. Depending on the application, high maximum permeabilities, or responsiveness to an external field, may be desired. High permeability, for example, is important for transformer core applications where fast switching fields are required for minimal hysteresis loss due to AC currents. In addition, low coercivity values are important for ensuring minimal hysteresis loss. If the material possesses such a property, a minimization of energy loss will be achieved and undesired thermal effects can be avoided when the material is subjected to currents. High saturation magnetization values are necessary for handling high current loads without reaching the saturation induction of the magnetic core. Figure 1.4 below highlights several magnetic properties from an M-H curve of a soft magnetic material with data shown from the I and II quadrants.

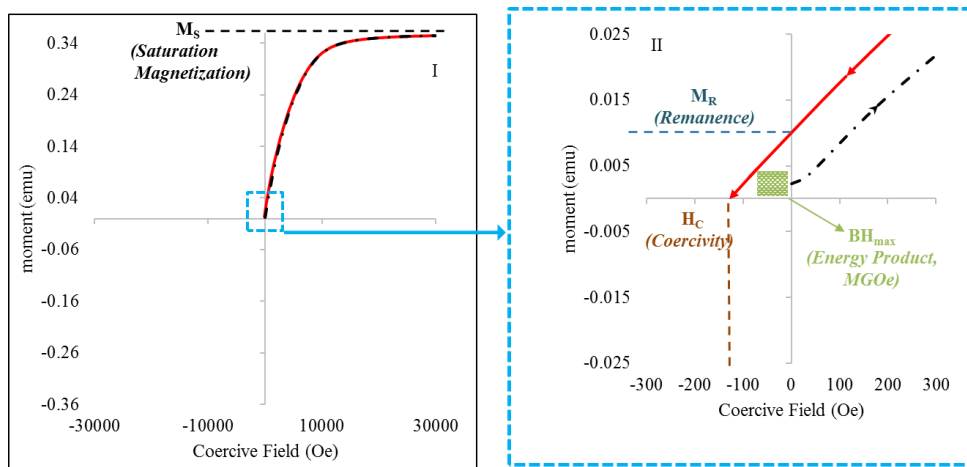


Figure 1.4. Partial hysteresis curve of a soft ferromagnet with virgin (black, dashed) and demagnetization (red, solid) curve and near zero-field region indicating magnetic properties.

It is worth mentioning the energy product, or magnetic energy density (BH_{\max}), is determined by calculating the maximum area possible in the demagnetization curve of the M-H loop shown by the green box in figure 1.4 above. Though not often a critical measure for soft magnets, the energy product is mandatory for determining the magnet performance for premiere hard magnetic materials such as SmCo, hexaferrites and NdFeB magnets.^{7,8} Nevertheless is important to understand in both magnet types.

1.5 Nanoscale Magnetism

Magnetism at the nanoscale is interesting for many reasons. A particular interest is the size effects on coercivity. Below is figure 1.5 which shows the variation in coercivity from superparamagnetic particle volumes up thru critical single domain volumes, vortex states and finally the largest sizes where multi-domain states are prevalent. Magnetization of particles having sizes near the single domain critical diameter (D_{SD}) can no longer fluctuate simply by domain wall rotation or motion. The reason is that this occurrence at larger particle sizes becomes energetically unfavorable at smaller particles sizes. Instead a uniform rotation of spins within the entire particle volume will occur; this effect generates the characteristic increase in coercivity observed.⁵

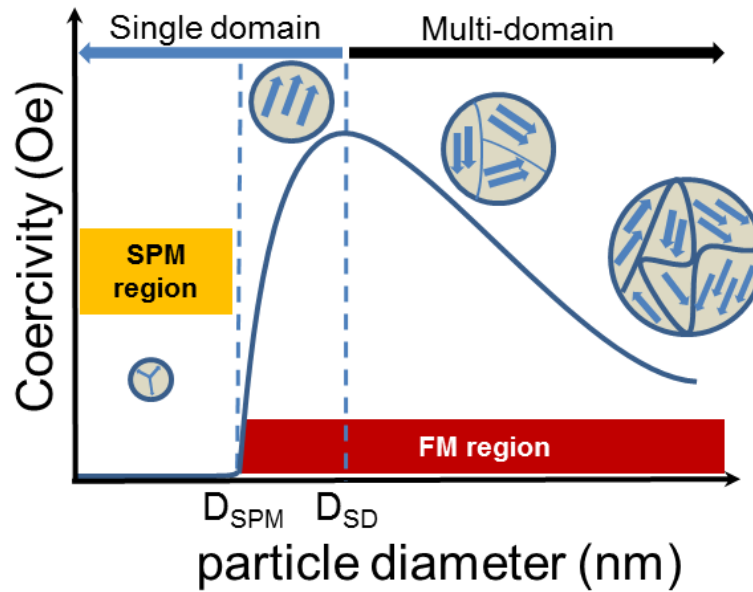


Figure 1.5. General relationship between particle size and coercivity indicating both the superparamagnetic (SPM) and ferromagnetic (FM) region.

Nanoparticles having diameters equal to or less than the critical superparamagnetic size limit (D_{spm}) are superparamagnetic. Larger particle sizes become single domain ferromagnets up to the single domain critical diameter (D_{sd}), Beyond the single domain region, particles may contain vortex and finally multi-domain structures.

The superparamagnetic regime describes particles as having sizes with volumes so small that they cannot maintain stable magnetization. This is a result of the product of the volume and the effective anisotropy K overcoming the thermal energy barrier (surpassing the volume dependent anisotropy energy barrier, ΔE) for the system. The relation is given below for a particle with uniaxial anisotropy with no external field presence in eq. (1)

$$\Delta E = KV = 25kBT \quad (1)$$

K , is the effective anisotropy constant, k_B , the Boltzmann constant and T , the temperature (K). This temperature is commonly referred to as the blocking temperature, (T_B) based on Neel theory.⁹

1.6 Soft Magnetic Materials

1.7.1 Fe, Co and FeCo Alloy

Fe, Co and FeCo are the premiere high magnetization (Fe and Co) and high Curie point (Co) soft magnetic material building blocks. Fe and Co are ferromagnetic elements at room temperature with Fe crystallizing in the bcc structure which provides the magnetic ordering and Co crystallizing in the hcp, fcc and epsilon structures. When Fe and Co are combined, they form a substitutional alloy with a bcc structure like Fe shown in figure 1.6 below. This ferromagnetic magnetic ordering in FeCo, commonly referred to as α_2 -ordered (B2) or at elevated temperature, α -disordered (A2), is lost completely at sufficiently high temperatures. Pure Fe undergoes a similar transition at a lower temperature. The critical temperatures or Curie points for Fe and Co respectively are 1043K and 1388 K where the transition from ferromagnetism to paramagnetism occurs.

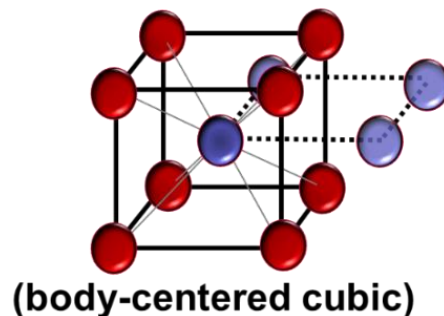


Figure 1.6. FeCo alloy body-centered cubic lattice structure representation for an ordered 50:50 Co:Fe (at. %). Fe atoms (red) and Co atoms (blue).

In figure 1.7, the phase diagram for Fe-Co is given showing the ordered α^1 B2 (bcc) structure transition to the disordered α A2 (bcc) phase above 700 C for a 50:50 Co:Fe at. %. Above 950 C, a phase change from the disordered α A2 (bcc) occurs to the non-magnetic

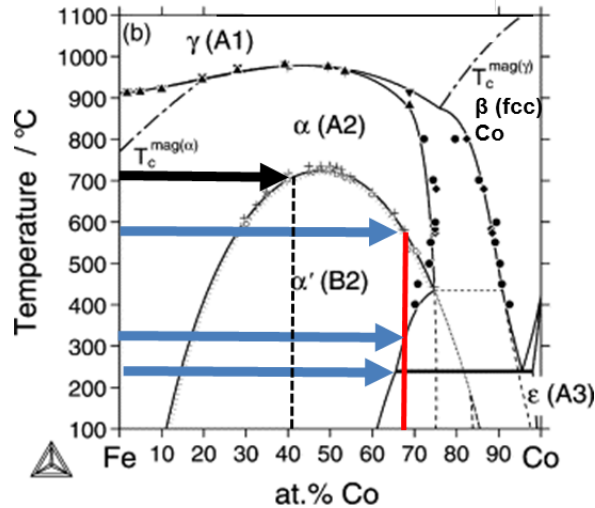


Figure 1.7. Co-Fe phase diagram with several phase transformations of a 68 % at. Co composition highlighted as well as 40 % at. Co transformation from B2 to A2 above 700 C. (modified from ref [6]).

(fcc) structure of FeCo.¹⁰ For Co-rich materials, depending on the synthesis, mixtures of (hcp) Co precipitates in ordered α^1 B2 (bcc) FeCo crystallites may be present. This is indicated by the red line in Figure 1.7 up to 225 C.

1.7.2 Nanocomposites and Amorphous Alloys

Several soft magnetic materials exist that have properties suitable for specific applications, though cost is a driving factor when considering commercial production. In transformer devices, substitutional alloys of Fe and Co with precipitated grains of Si and B are desirable, however one set back is the expense of Co. FeSi stress-annealed ribbons offer excellent soft properties exhibiting high permeabilities and moderately high saturation values with coercivities less than 1 Oe.¹¹ These materials are widely used as the material cost is somewhat cheaper although thermal and induction properties are not quite as competitive.^{12,13} In general, soft magnetic materials possess high permeability when their composition contains an amorphous phase and a

nanocrystalline phase.¹¹ These materials are known as nanocomposites. The amorphous or glass phase may be of B or Si elements while the nanocrystalline phase is typically Fe and Co based.^{11,14} Several relationships of these competitive soft magnetic materials are given below in figure 1.8.

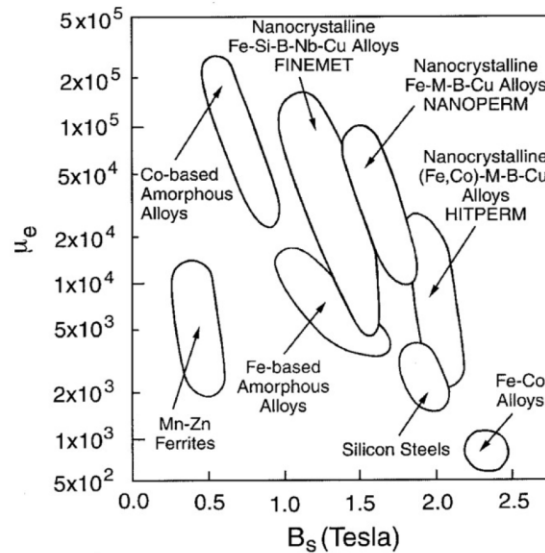


Figure 1.8. Permeability and saturation magnetization relationships for a variety of premiere soft ferromagnetic materials with FeCo alloys shown. Modified from ref (11).

FeCo-based nanocomposites have the advantage of high saturation induction values and high Curie points. However, they lack the high permeabilities such as Co-based amorphous alloys as well the commercial alloys of FINEMET and NANOPERM. Commercial alloys such as FINMET, NANOPERM or HITPERM are nanocrystalline amorphous composites that rely on either Fe, Co or both in an amorphous matrix in order to achieve their exceptional soft magnetic properties of high permeabilities up to $10^4 - 10^5 \mu_e$ (at 1 kHz) and high induction values up to 200 emu/g.^{11,14-19}

1.8 Polyol Method

The polyol process is a wet-chemical reduction process that uses a polyhydric alcohol such as ethylene glycol or triethylene glycol which acts as a reaction solvent and reducing agent. Several nanomaterial syntheses using the polyol process exist and these materials have a wide range of elemental compositions and applications including luminescent materials of ZnOS, noble metal nanoparticles of Au, Pt and Ag, core-shell nanoparticles of Cu@Ni and magnetic nanoparticles such as Fe, Co, Ni and their alloys.²⁰⁻³¹ Polyol syntheses are typically initiated by a hydroxide source which acts to deprotonate the polyhydric alcohol groups therefore increasing its reduction potential. It is worth mentioning that metallic tungstates, for example, may be reduced using the polyol process in acidic media as opposed to alkaline media.³¹ Temperature increase may also increase the reduction potential but should be moderated to achieve phase control or morphologies. Fernand Fievet coined the term polyol process and first made mention of it in his syntheses of Cu, Ni and Co NPs having isotropic morphologies.^{32 33} Fievet also described the polyol synthesis of these ultrafine metallic particles as via the mechanistic pathway shown below in figure 1.9.³²

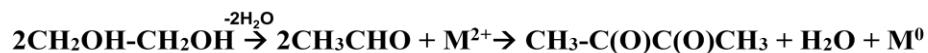


Figure 1.9. Generalized mechanistic route for polyol reductions using ethylene glycol and a divalent metallic precursor. First dehydration to aldehyde and subsequent oxidation to diacetyl and reduction to metal.

The oxidation of acetaldehyde into diacetyl is proposed as providing electrons for the reduction process. Wet-chemical methods such as the polyol process done in this work, uses a polyhydric alcohol, as opposed to monohydric ethanol, as a solvent and reducing agent and is employed to synthesize nanoparticles of FeCo alloy along with a plethora of transition metals

including Co, Fe, Ag, Cu and Ru, Pd and Pt.³³⁻³⁵ Other materials that may be synthesized using this technique include several magnetic compounds or alloys of some of the previously mentioned elements; polyol synthesis is also extended to several highly functional nanoscale materials such as ZnO, ZnS:Ag⁺, Cr₂O₃, TiO₂ and α -Fe₂O₃ to name a few.^{31,36} In addition, polyol methods are considered green synthesis methods. Polyhydric alcohols typically have low toxicity with the exception of ethylene glycol. Propylene glycol, for example, is approved for human consumption by the FDA.³¹

It is important to mention the care that should be taken when choosing precursors for polyol syntheses. For example, CoCl₂ does not readily form a reducible metal complex unlike cobalt acetate when considering synthesis of cobalt nanoparticles.²² For this reason, cobalt acetate was the cobalt precursor of choice for the work presented herein and FeCl₂ was the choice of Fe precursor as reduction are readily achieved at temperatures as low as 120 C..²²

1.9 High Throughput Experimentation

High throughput experimentation (HTE) approaches heavily rely on using reaction equipment or reactor configurations that can handle performing simultaneous reactions in order to generate a large number of data. This data may be used for fast screening of properties or statistical investigations by use of design of experiments (DOE). Combinatorial chemistry is a relatively recent field of study that involves HTE where several hundred to thousands of reactions may be performed for discovery of useful pharmaceutical compounds.³⁷⁻³⁹ These synthesized compounds may have excellent biological applications such as enhanced enzyme or receptor binding properties. They may also be used for specific organic compounds of a desired structure for a specific use.^{37,39} Process synthesizers such as the Argonaut Surveyor (by Agilent Technologies) may automate simultaneous reactions for the purpose of a new drug or material

discovery. Such equipment was utilized for much of the work performed in section one on the synthesis of Fe and Co-based nanomaterials. as it provided environmental control and capability to perform multiple reactions simultaneously.

1.10 Continuous Flow Chemistry

Continuous flow chemistry (CF) processes have the benefit of synthesizing molecular compounds or functional materials by efficiently consuming precursors, synthesizing products portably and precise control of tuning material properties.^{38,40-46} Relatively few CF processes exist in literature on syntheses of ferromagnetic nanomaterials.^{41,45-47} This is likely a result of clogging issues when synthesizing solid particles in equipment that typically possess mill- and even microscale internal dimensions.

Advantages are numerous for CF synthesis of functional materials. This can range from minimal precursor consumption with material flow rate control to portable flow reactors, which can be made to synthesize drugs for military soldiers in immediate need by the push of a button.⁴⁸ Another advantage for the materials chemist is the ability to tailor useful properties of a material. While work has yet to be done to explore this, magnetic properties of coercivity, for example, could be finely tailored by regulating the flow rate of an initiator into an aqueous reduction process. Of the CF work done in this dissertation, an Erhfeld ® Microreactor was used for the Co NPs synthesis and an improvised assembly of pumps, tubing and fluid lines was used for the CF synthesis of FeCo. More details are given on both CF methods in section 2.

1.11 Summary of Objectives

The major goal of this dissertation work is the general exploration of the ferromagnetic nanomaterials made up of late-transition metals of Fe and Co as well as their alloy and magnetic oxides using solely wet-chemical preparation methods. This goal was accomplished by undertaking the following objectives:

1. Explore significant factors and practical limitations in the synthesis of FeCo and cobalt ferrite nanomaterial using the polyol process for phase control and magnetic property enhancement with high-throughput experimentation (HTE).
2. Synthesize FeCo alloy nanomaterial using the polyol process to gain morphological novelty and magnetic property enhancement.
3. Control physical properties of high aspect ratio FeCo alloy nanomaterial using Ag as a nucleating agent by polyol chemistry. Conduct DOE to demonstrate statistical significance for control of magnetic properties, phase and morphology with high-throughput.
4. Synthesize cobalt ferrite nanomaterial using the polyol process for morphological novelty and magnetic property performance.
5. Continuous flow synthesis of Co nanomaterials using aqueous reduction for synthesis novelty and industrial scale-up viability
6. Continuous flow synthesis of FeCo nanomaterial using polyol chemistry for synthesis novelty and to explore synthesis limitations.

Chapter 2. Characterization Techniques

2.1 Introduction

Characterization of nanomaterials is mandatory when wanting to know about composition, morphology and properties. There are a wide variety of techniques out there, whether for study of the surface composition or internal microstructure. For synthesizing ultrafine metallic powders as in this work, the knowledge of final composition is paramount. One reliable technique for this is diffraction. Whether the diffraction beam source is an electron, X-ray or neutron, the crystallographic structure can be determined of crystalline nanoscale powders. Morphological study is important for determining nanoparticle shape and dimensions. Several imaging techniques are available and while the transmission and scanning electron microscopy modes are powerful tools for imaging, they often have optional capabilities that go beyond this. These instruments are capable of measuring chemical analysis whether by energy dispersive spectroscopy in SEM or electron energy loss spectroscopy in TEM. Magnetic property measurements are required when performing synthesis of magnetic nanomaterial. Since this work is focused purely on magnetic materials, it relies heavily on magnetic characterization by use of vibrating sample magnetometry. The heavily used characterization techniques as mentioned above are discussed in further detail in this chapter.

2.2 X-Ray Diffraction (XRD)

This technique is used to characterize and probe the crystalline structure of a material whether it be multi-phasic or a single phase of a powder sample having typically a nanoscopic or microscopic grain or particle size. A W filament is heated with a current where the work function of the filament surface is overcome and electron emission occurs. The emitted electrons are accelerated at a potential typically in the 40-60 keV range and are bombarded onto target, most commonly Cu, Ag or Mo. These high energy electrons eject core electrons, or

photoelectrons, from an inner K-shell from a metallic target following an electron from a higher energy state in an outer L-shell to fill the lower energy K shell. The loss in energy of the electron is released in the form of a characteristic X-ray wavelength of the target material. Cu was the anode materials used for x-ray analysis shown throughout this work. Cu has $K\alpha_1$ and $K\alpha_2$ wavelengths and the average of these two is used weighing their intensity ratios are 1:2. The averaged wavelength for a copper x-ray source is $K\alpha \approx 1.540 \text{ \AA}$ Bragg's Law is given below as

$$n\lambda = 2d\sin\theta$$

where λ = x-ray wavelength, $K\alpha \approx 1.540 \text{ \AA}$ and θ is the angle of x-ray reflection normal to the sample surface. Bragg's Law gives the condition for constructive interference when the change in total x-ray path length (incident and reflection) between two or more x-ray waves are an integer where $n=1, 2, 3$ etc. When a powder sample contains particles having long-range, ordered arrangements of atoms (i.e. crystalline), certain orientations at particular angles will produce constructive interference, or diffraction peaks, while angles between will result in x-ray scattering or will result in no to minimal diffraction peak intensity giving rise to non-constructive interference or overall cancellation of the x-ray intensity due to wavelength mismatch. Below, figure 2.1 gives a schematic of incident x-ray wavelength onto a sample substrate detailing the physical origin of variables of Bragg's law. Amorphous (non-crystalline) powder materials result in scattering with no diffraction peaks observable, while nanoscopic materials generally produce very broad diffraction peaks due to increased scattering at very small particle volumes.

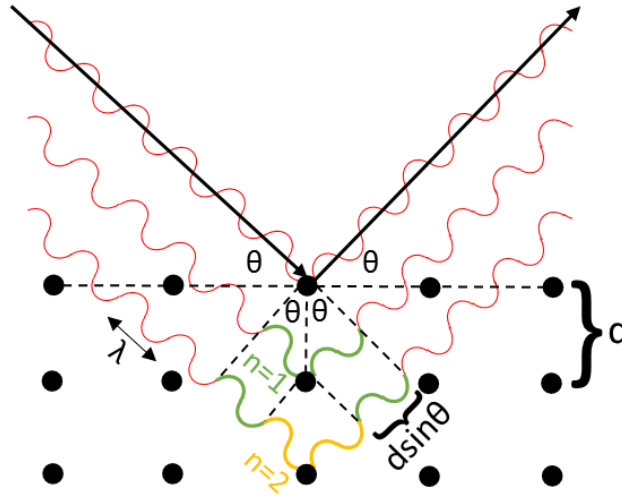


Figure 2.1. Scheme of incident and diffracted x-rays in a substrate depicting the components of Bragg's Law.

Scherrer crystallite size analysis follows the equation given below as

$$\text{Crystallite size} = \frac{K\lambda}{\beta \cos\theta}$$

where K is the shape factor of the material, (0.9 for sphere), λ is the x-ray wavelength, β is the FWHM for the plane and θ is the diffraction peak position in degrees all of which calculates an estimated crystallite size average of the sample for a particular plane or Bragg reflection.

2.2.2 High Temperature X-Ray Diffraction (HT-XRD)

High temperature XRD is performed to examine phase changes at elevated temperatures. These measurements can analyze phases with annealing in various environments such as nitrogen or air. Thermal expansion of the aluminum oxide heating element must be compensated for by adjusting the sample height to bisect the total x-ray beam at each temperature. Doing these steps between each temperature change produces a consistent baseline which reduces masking or augmentation effects of minor phases that may be present.

2.3 Vibrating Sample Magnetometry (VSM)

A sample is centered between two coils in a uniform magnetic field and vibrated at a constant frequency (i.e. 40 Hz with 2mm amplitude) as the measuring field is increased from 0 Oe to a maximum saturating field, often several Tesla. After the saturation field is reached in the positive direction, field reversal and subsequent magnetization measurement begins in the negative direction until the saturation field is reached. Finally, the field is reversed once more to a positive field until the saturation field is again achieved in the positive direction resulting in loop closure and alignment of magnetic domains in that direction. For ferromagnetic materials, this magnetization loop is referred to as a hysteresis loop (M-H) which in part represents the overall magnetic energy density of the material and total energy loss. A schematic of how the magnetic sample is placed within a VSM with respect to pick up coils and the applied field is given below in figure 2.2.

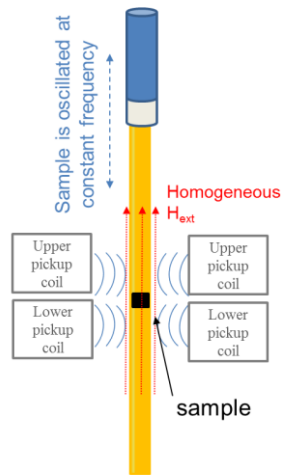


Figure 2.2. General schematic of VSM sample powder mounted inside chamber showing orientation to measuring field and pick up coils.

Other measurements that may be performed with the VSM include isothermal and dc demagnetization curves which are a measure of the materials remanence in different ways. The

former is acquired by placing a demagnetized sample into a VSM and applying incremental field steps at set time intervals then removing the field, performing the remanence (moment) measurement, and repeating the process until the material is saturated. The DCD curve is acquired by applying a positive field saturating the material followed by the process used to gather the IRM but with negative field increments. Extrapolating the two curves to find the change in magnetization (δM) will show positive exchange or negative exchange interactions between the particles or grains of the sample.⁶ Further, the reduced magnetization of the DCD (-1 to 1) and IRM (0 to 1) may be plotted. This is known as a Henkel plot and deviation from linearity indicates magnetic exchange interactions within the sample, similar to the change in magnetization plot.⁴⁹

2.4 Transmission Electron Microscopy (TEM)

This imaging technique relies on high energy electrons penetrating a sufficiently thin specimen typically < 100 in thickness where differentiation in contrast due to variation in sample morphology or thickness is detected onto a CCD camera and finally recorded as a digital image. Specimens must be electron transparent for this technique to be of usage and may be prepared in several ways depending on sample type. Drop-casting onto a sample grid is a preferred technique for imaging nanoscopic powders including magnetic nanomaterials synthesized in this work.

Figure 2.3 details the various interactions incident high energy electrons may have when bombardment with a specimen occurs inside of the TEM.

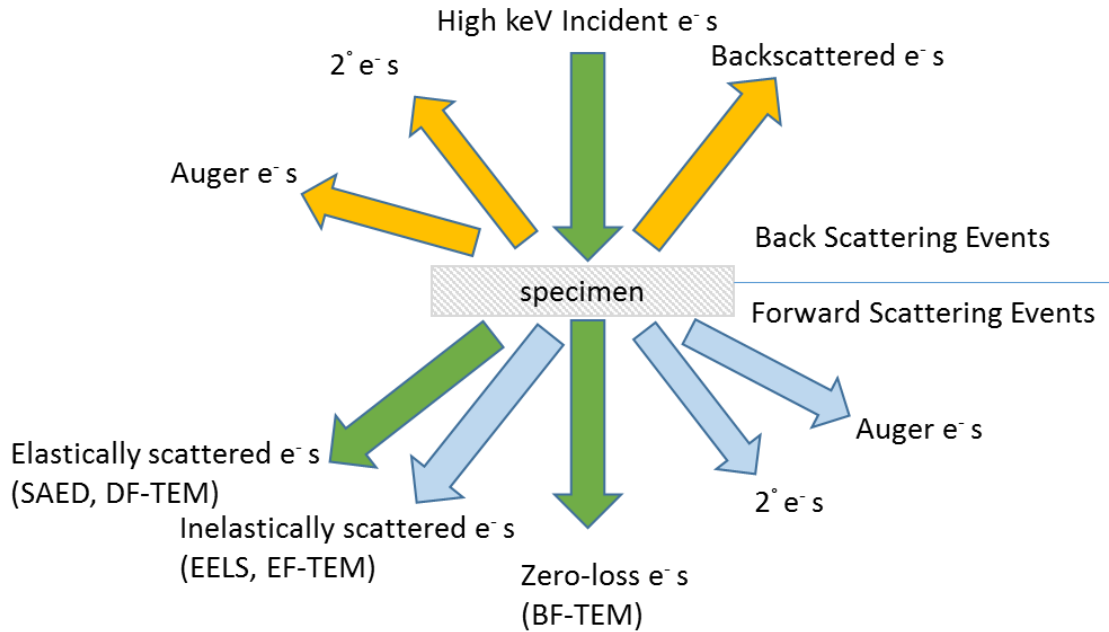


Figure 2.3. Scheme of various electron interactions in a TEM sample from high energy electrons.

Basic imaging modes rely on zero loss electrons and a portion of the plasmon and inelastically scattered electrons for image formation. If electrons were filtered to only transmit electrons having energies very near to zero energy loss, minimization of aberrations and imaging artifacts is achieved as well as contrast enhancement depending on the sample thickness.

2.4.1 Selected Area Electron Diffraction (SAED)

Electrons bombarding a TEM sample may undergo multiple interactions as show in figure 2.3. Electrons that form (selected area) diffraction patterns (SADPs) are referred to as elastically scattered electrons which do not lose energy however change direction. The ordered atoms in a material act to scatter incident electrons which lead to formation of periodic arrangements of bright spots observed depending on the crystal structure and orientation of the sample onto a TEM camera screen which is a projection of the reciprocal lattice. A single crystal Fe cube with the surface normal oriented parallel to the incident electron beam may produce an

array of diffraction spots equidistant from one another indicating that the (100) zone axis has been imaged. Polycrystals may exhibit SADPs that are more difficult to interpret where often multiple reflections may overlap. Important information to a material scientist researcher can be inferred by carefully analyzing the SADPs. This information may pertain to phase identification, nanostructure, microstructure, particle or sample morphology, lattice spacing, d-spacing as well as overall crystallinity, that is, whether the sample is amorphous, single crystal or polycrystalline material. Crystalline materials or particles on the nanoscale often display diffuse or smoothed Bragg reflections in SADPs which often appear as continuous rings while larger particle size can be observed as having reflections forming disjointed rings of larger spots. Particle populations should be sufficient in the analysis of TEM samples for SAED in order to form continuous SADPs so that all orientations of the particle having a particular Bragg reflection can be observed within the Debye cone. The selected area term arises because an aperture is inserted into the imaging plane to only pass those electron being diffracted from a selected region of a sample, cluster of NPs of interest or a single particle. When performing electron diffraction techniques, the beam is in a parallel illumination configuration. Using the selected area aperture often results in enhanced S/N ratios and sharper images of SADPs though it is not required in general to obtain a diffraction pattern.

2.4.2 Dark-Field Microscopy (DF-TEM)

Dark field imaging techniques rely on incident electrons becoming elastically scattered with atoms in the specimen. This occurs where the angle of gun tilt or incident electron beam forms a Bragg reflection depending on the phase of the material imaged, which generates an image of diffracted electrons of that given crystallographic plane. The contrast is reversed as compared to conventional BF-TEM where the crystalline material appears bright and all other

non-diffracting material appears dark. This technique is useful for confirming crystallinity in a particle for example and more elegantly, for visually identifying two or more different crystals within a single particle.

2.4.3 Electron Energy Loss Spectroscopy (EELS)

Electron energy loss spectroscopy relies on the electrons having specific energy losses which correlate directly to an element. These electrons form the inelastically scattered spectrum where for example electrons with energy loss around 285 eV correspond to a sample containing carbon and electrons having energy loss around 780 eV correspond to Co. Electrons with no energy loss are considered to be zero-loss electrons and these form an intense peak at the beginning of an EELS spectrum known as the ZLP (zero-loss peak). Filtering of the intense signal is necessary to prevent damage to the CCD detector and may be done so by introducing a slit-monochromator aperture. This aperture has a manually adjustable slit width (measured in eV) and may only allow electrons that are from a particular element provided there is no elemental edge overlap. This technique is used in energy-filtered imaging techniques (EF-TEM) for the purpose of generating detailed elemental mapping in TEM micrographs. Acquiring EF-TEMs are

2.5 Scanning Electron Microscopy (SEM)

Electron microscopy techniques such as scanning electron microscopy (SEM) detect secondary electrons that are emitted from the surface of a material. This photoemission is caused by an incoming high energy electron beam emitted from either a W or LaB₆ filament, though other filament types may be used. The most common acceleration voltages used in SEM imaging are from 1-30 kV. If higher energies are required, TEM imaging is the best option for

imaging. Surface sensitive imaging is best performed using SEM while TEM is best suited for analyzing the interior of a sample. Energy dispersive spectroscopy is a technique often employed in an SEM which is a destructive elemental analysis technique used to determine relative atomic or mass % of elements present on or near the surface. Characteristic X-rays of elements present are emitted from core shell ionizations. These x-ray energies are detected and quantitated through use of specialized software.

2.5.2 Focused Ion Beam (FIB)

Focused ion beam is a technique associated with SEM in which a FIB column emits heavy Ga ions at controlled currents to mill at materials making slices, cross-sections or lamella. It is often used in conjunction with TEM where the lamella may be welded using a Pt source to a special design index grid inside the SEM and then transferred to a TEM as the sample lamella is then sufficiently electron transparent. Inside the TEM, SAED and EELS and phase contrast imaging techniques may be performed which generate results and images of much higher accuracy and clarity respectively than an excessively thick or unprepared by FIB sample.

Section 1: High Throughput Experimentation: Polyol Process

Chapter 3. Polyol Synthesis of Cobalt Ferrite and Fe₁Co_{1-x} Nanomaterials

3.1 Overview

The motivation for this work was to determine significant factors, both environmental and parametric, to control the synthesis of the FeCo bcc alloy phase and cobalt ferrite phase nanomaterial. Maximization of the saturation magnetization of FeCo alloy phase and maximization of H_c of the cobalt ferrite phase was a goal for this work. The high-throughput experimentation (HTE) format for running these reactions was achieved by using a process synthesizer/reactor assembly. This eliminated the traditional requirement for bench-top/glassware set-up allowing for better control of environmental variables and the ability to run up to 10 simultaneous reactions. Furthermore, a motivation for performing several reactions using labor intensive HTE is having the perpetual opportunity for discovery of unique morphologies.

3.2 Introduction

FeCo alloy crystallizes in a body-centered cubic structure and has the highest saturation magnetization of any material at room temperature with induction values as high as 23,500 G (>240 emu/g) for a 65 % Fe composition.² Cobalt ferrite on the other hand, is the inverse spinel oxide CoFe_2O_4 , and is considered a hard magnetic material with saturation magnetization limits at around 80 emu/g but greater coercivity values up to 1kOe for as-synthesized nanomaterial using wet-chemical methods.⁵⁰ These two phases are routinely synthesized together when the goal is to synthesize pure phase FeCo when using the polyol method. This typically proves to be undesirable to the synthetic chemist when phase control is not achieved or well understood. Controlling the relative amounts of each phase, and more important -achieving phase selectivity- while maintaining optimum magnetic properties presents a challenge. On the contrary, synthesizing combinations of CFO and FeCo can be applicable for creating very soft inductor

cores having a high permeability after proper processing, annealing and compaction methods yet, controlling the relative phase amounts controls the intrinsic (bulk) saturation magnetization (by mass) and extrinsic property of H_c (Oe) of the final soft magnet. Synthesis of cobalt ferrite nanoparticles has been performed previously by methods of co-precipitation, solvothermal routes and thermal decomposition achieving a variety of morphologies with varying magnetic properties.⁵¹⁻⁵⁶

3.3 Experimental

A routine polyol process-based reaction that was performed producing a composite of FeCo alloy and cobalt ferrite (CFO) nanomaterial is as given below. To a PTFE reaction vessel (cylindrical tube, 40 mL total vol.), 25 mL of ethylene glycol (solvent) was added with the vessel mounted onto an Argonaut Process Synthesizer, (see figure 3.1 below) followed by addition of Iron (II) Chloride tetrahydrate and Cobalt (II) Acetate tetrahydrate salts to give a total molarity of metal, [Metal], equal to about 0.1 at about 35 % Fe (atomic). To initiate each reaction solution, sodium hydroxide was massed to give about 3.5 M [OH] followed by heating to 150 C using temperature controlled heating probes. Further variations in reaction time, [OH], [Metal] and Fe:Co molar ratios were studied in depth and discussed below using a one variable at a time approach (OVAT). This was done to screen for significant independent factors for phase control.

A scheme generalizing the surveyor reactor assembly used in this chapter as well as the next several chapters is given in figure 3.1 (a) below. Also, in figure 3.1 (b), a photograph is given of several polyol reactions running simultaneously inside PTFE reaction vessels.

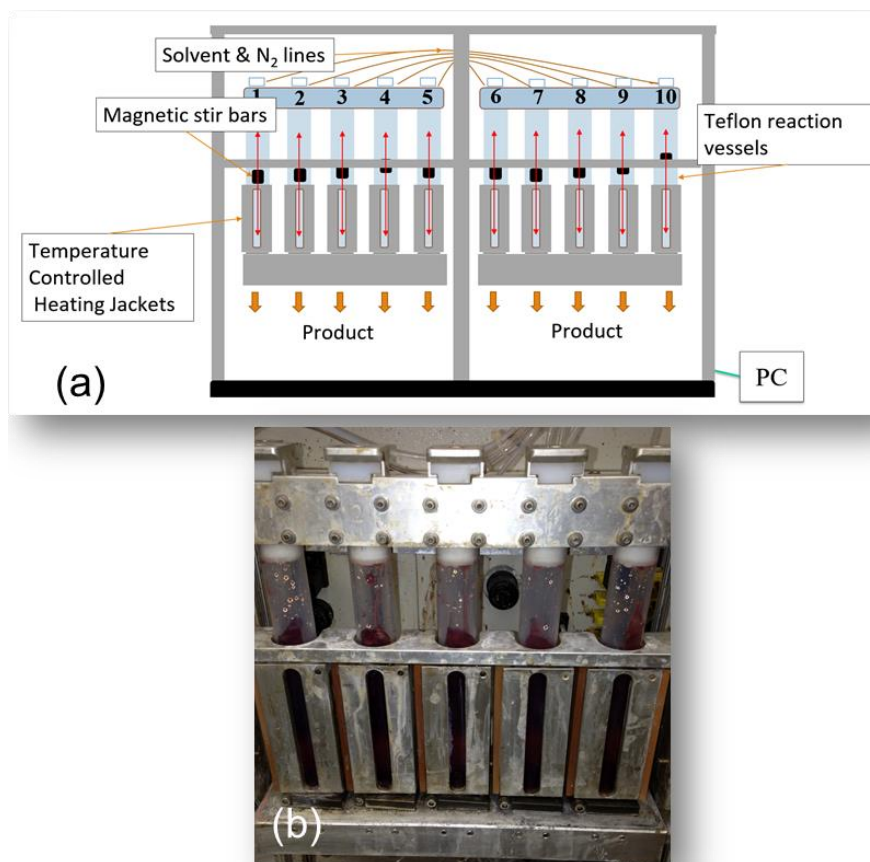


Figure 3.1. Scheme of the Argonaut Process Synthesizer (a) used to perform the FeCo and CFO nanomaterial syntheses via polyol process. Photograph of a 5-reaction vessel bank on process synthesizer with in-process polyol reactions shown (b).

3.3.1 Characterization

Material characterization techniques used for this work include XRD where several powders were analyzed in a Bragg-Brentano configuration with Cu K α radiation $\lambda \approx 1.54 \text{ \AA}$. All powders were centered onto low background oriented single crystal Si wafer and analyzed from 20-70 for phase ID and 20-85 for phase identification and percent phase composition to include all peaks of FeCo bcc alloy. SEM was performed using a Hitachi SU-70 FE-SEM and was used to characterize the morphology of the as-synthesized nanomaterial all performed at 5 kV, a generally moderate acceleration voltage, to generate images with enhanced surface or

topographical features. A TEM imaging was performed using a Zeiss Libra 120 kV TEM equipped with a LaB₆ single crystal filament as an electron source. TEM was used to further characterize the morphology of the material complementing the SEM imaging as well as acquire elemental mapping of the nanomaterial samples all performed at 120 kV and SAED (selected area diffraction) patterns to correlate crystal structure and morphology. DFTEM (dark-field imaging) was used to correlate the diffracted particle with the particular phase present in the SADP (selected area diffraction pattern). Precession around particular Bragg reflections allowed for DFTEM to be acquired and compared with BFTEMs. The EFTEM mapping technique was done so by only allowing Fe and Co electron energy loss edges to be filtered through to the camera by use of an omega filter. All samples imaged by TEM were first prepared by drop-casting 3x a dilute solution of nanomaterial in 100 % ethanol onto 300 mesh formvar-coated Cu grids followed by drying in vacuum oven for 24 hours.

Vibrating sample magnetometry (VSM) was employed to characterize every magnetic nanomaterial sample produced from the process synthesizer. The VSM used for this work was a Quantum Design VersaLab system equipped with a NbTi superconducting magnet capable of producing an external field strength up to 3 T. All as-synthesized powders were washed with MeOH and dried in a vacuum oven for at least 24 hours and carefully massed into polypropylene capsules. Each sample contained in each capsule was carefully centered onto a brass tube and mounted by compressing the walls of the holder reducing the need for adhesive tape with could introduce magnetic impurities. The magnetic signature of the brass sample holder is negligible as it is in the noise range of the moment of the VSM (10^{-6} emu). M-H curves, otherwise referred to as hysteresis curves or loops, were acquired for each sample by oscillating it in an external sweeping field, reversal field and finally back to saturation in the positive field. From this loop,

coercivity and saturation magnetization values were recorded and used in this study to probe for optimization of these values as well as relationships to phase variations from sample to sample.

3.4 Results and Discussion

Below in figure 3.2, a representative XRD overlay is given for two varying compositions of as-synthesized FeCo and CFO (cobalt ferrite) mixtures. The scan in (a) indicates a CFO-rich composition (> 80% cobalt ferrite phase) while scan (b) gives a relatively FeCo rich composition (>50 % FeCo phase).

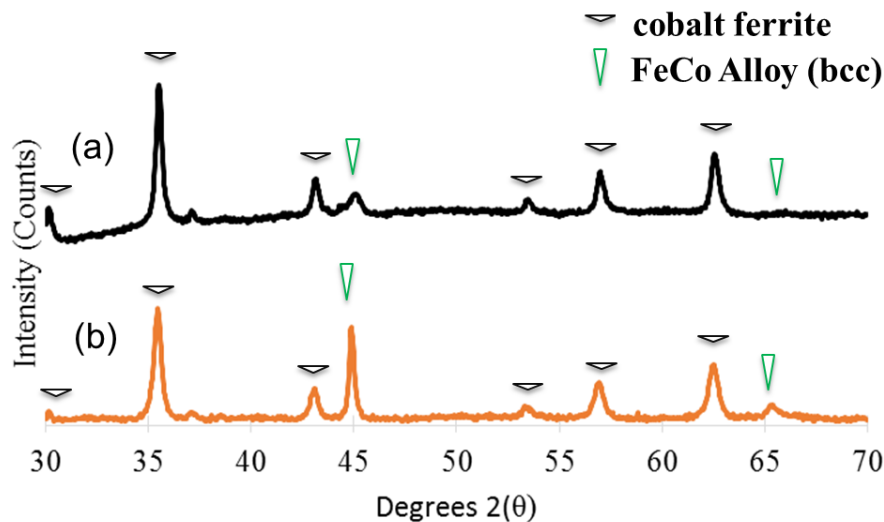


Figure 3.2. Representative XRD patterns of FeCo (green triangles) and Cobalt ferrite (black triangles) nanomaterial composite synthesized by polyol-process via high throughput format with CFO-rich in (a) and FeCo-rich in (b).

It is important to note that no other phases were observed by XRD; no oxides of Co, Co (fcc or hcp), Fe (bcc), or other oxides of Fe such as FeO or Fe₂O₃ were detected. Imaging by TEM was performed to probe for morphology as well as isolate various morphologies by DFTEM as shown below in figure 3.3 (a-d).

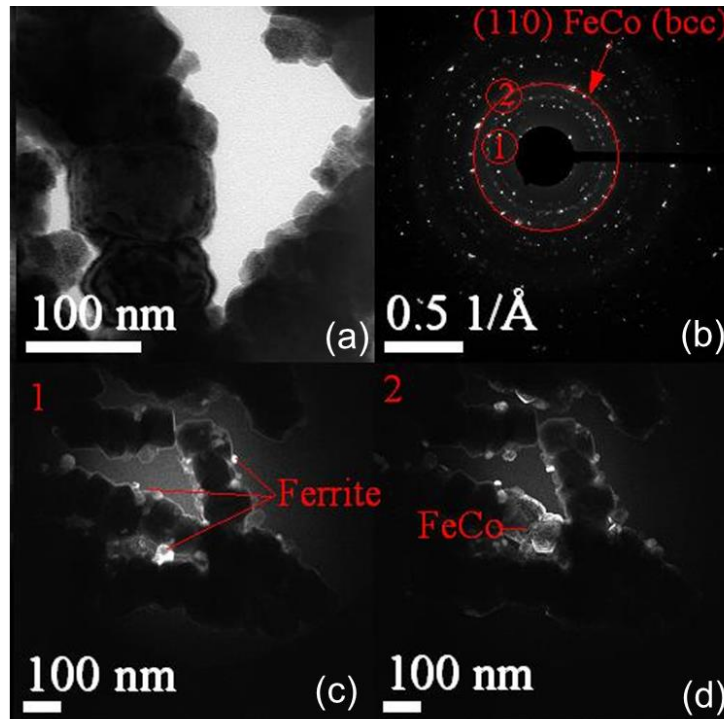


Figure 3.3. TEM image of an FeCo and cobalt ferrite composite (a) with SAED shown indicating both phases (b) and dark-field cone illumination of cobalt ferrite particle (c) and dark-field cone-illumination of FeCo particles along with cobalt ferrites (d).

Dark-field microscopy was performed in figure 3.3 (c) and (d) labeled with a 1 and 2 respectively showing the partial reflections from the (220) plane of cobalt ferrite in (c) and the (110) plane of FeCo bcc in (d). A few dark-field illuminations of CFO particles are observed in image (d) along with the larger (110) FeCo particles as the cone precession around the corresponding Bragg reflection labelled with a 2, (110) FeCo, was aligned where it included the (220) Bragg reflection from cobalt ferrite. This imaging artifact is due to a limitation of the objective aperture size and could not be avoided. In image (c) of figure 3.3, cobalt ferrite particles could be isolated and imaged due to the absence of FeCo reflections at a higher d-spacing (lower Bragg reflection angles).

Imaging of the FeCo/CFO nanomaterial was also performed by SEM as shown in figure 3.4 where image (a) shows a pristine FeCo, 100 % FeCo sample, and (b) shows as mixture of the

FeCo and CFO phases similar to the sample imaged by TEM in figure 3.3 (a). The red arrows in figure 3.4 (b) point toward cobalt ferrite particles and are of similar morphology as observed in the TEM image in figure 3.3 (c).

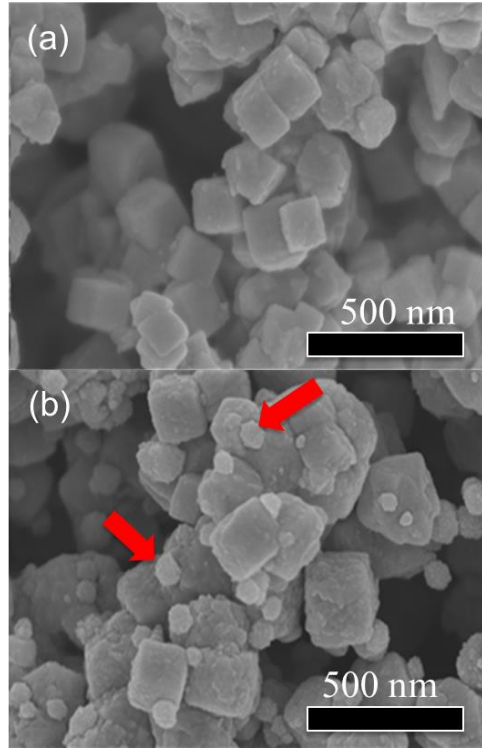


Figure 3.4. SEM micrographs of FeCo nanomaterial (a) and FeCo/CFO (b) complementing TEM images from figure 3.3 (d). Cobalt ferrite particles are identified with red arrows in (b).

The SEMs further substantiate the morphology and phase relationship explained previously by TEM analysis and compliment the DF-TEM images shown in figure 3.3 (c) and (d).

Another observational study by TEM was performed by imaging FeCo/CFO nanomaterials synthesized and ordering those images in increasing saturation magnetization values to visually probe for any well-expected morphology/magnetic property relationship shown in figure 3.5.

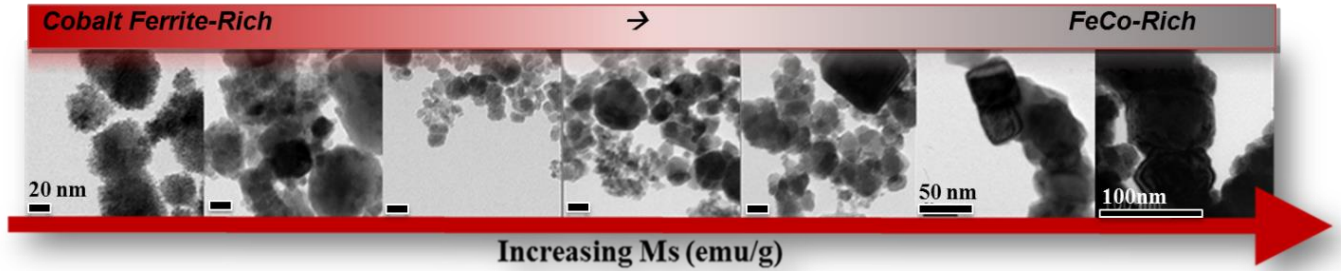


Figure 3.5. TEMs of increasing compositions of FeCo % and increasing saturation magnetizations from left to right of FeCo/CFO nanomaterial.

CFO/FeCo samples possessed M_s values as low as 65 emu/g (far left image in figure 3.5) to M_s values as high as 185 emu/g with M_s steps roughly around 20 emu/g for samples in TEM images shown between. In the low M_s samples, poorly crystalline to amorphous particles of cobalt ferrite are observable where no cubic structures pertaining to FeCo alloy are visible while for high M_s nanomaterials shown to the right, cubic structures are only present with minimal cobalt ferrite particles evident. It is important to mention that the presence of some amount of iron oxide impurities are expected when doing wet-chemical syntheses of nanoparticles from iron salts and are difficult to avoid completely. Energy filtered TEM images were acquired to confirm the FeCo alloy by probing for a distribution of Co and Fe throughout a cluster of cubes shown in figure 3.6 (c). The presence of Co and Fe were confirmed by the EELS spectrum shown in (e) of figure 3.6 with C, Co and Fe maps shown respectively in (a, b and d).

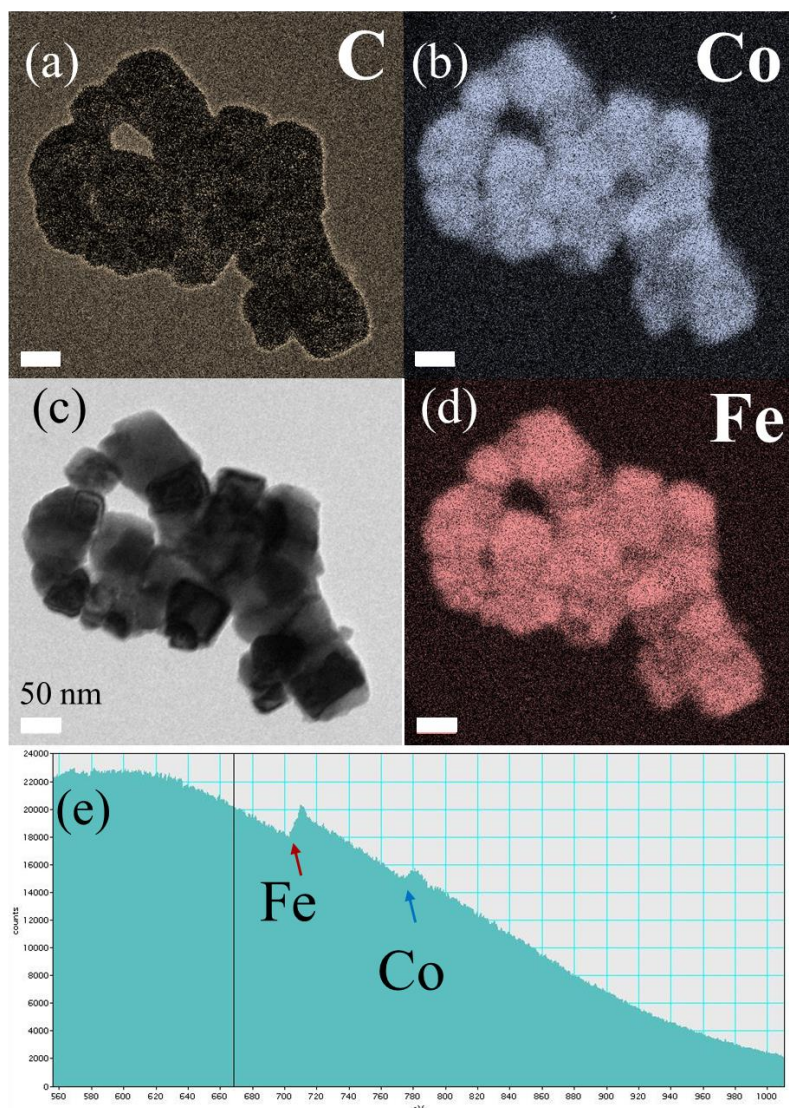


Figure 3.6. BFTEM image (c) with corresponding EFTEMs of C, Co and Fe colored maps in (a, b and d) and EELS spectrum showing energies from 560-1000 eV in (e) with labelled Fe and Co edges at around 708 and 780 eV respectively.

Carbon mapping was performed in (a) of figure 3.6 where the formvar (carbon) grid background is shown as light tan as well as the surface of the FeCo cubes via light brown halo. This is due to a thin passivation layer of carbon on the surface due to degradants of the reaction solvent, ethylene glycol, forming a thin film during the polyol reaction.

Energy filtered TEM images were also acquired to confirm presence of Co substituted into the iron oxide crystallites to support the XRD in figure 3.2 confirming qualitatively the presence of cobalt ferrite oxide (CoFe_2O_4) over magnetite (Fe_3O_4) and are given in figure 3.7. TEM image (a) in figure 3.7 was used as the BFTEM for the elemental mapping where the Fe map as generated (upper right inset, red) and the Co map (lower right, blue).

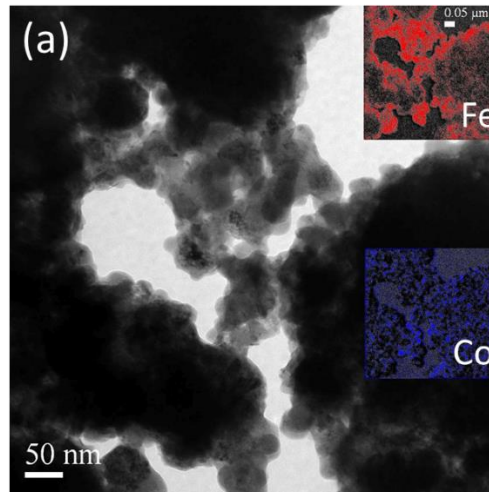


Figure 3.7. EF-TEM of typical CFO-rich sample showing distribution of Fe (red) and Co (blue) maps in EFTEM insets (right).

Presence of Fe and Co edge loss peaks were confirmed by EELS spectrum before taking each elemental map though spectrum is not shown.

Initially up to 150 polyol syntheses were performed using the surveyor process synthesizer and their corresponding VSM characterization were performed within 24-48 hours after each respective synthesis. The saturation magnetization and coercivity values of all reactions were plotted together in an X-Y plot shown below in figure 3.8. High throughput experimentation such as the type performed in this work is useful for creating forced magnetic property trends where the phases are limited to two or less. There are in general two trends or

regions highlighted first (using 90 % coverage elliptical plots) distinguished by reaction volume used in the PTFE vessel.

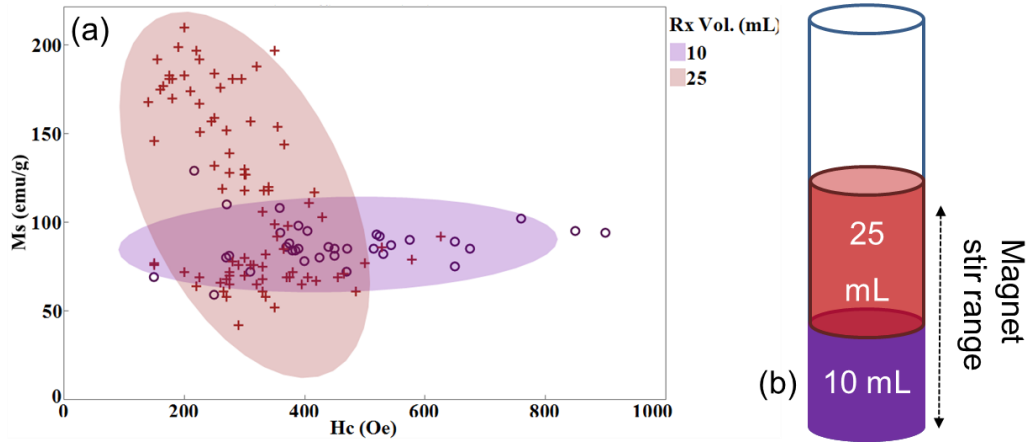


Figure 3.8. X-Y plot of saturation magnetization versus coercivity indicating distinct regions of plots based on total reaction volume.

Evidence that lower reaction volumes are attributed to nanomaterial possessing higher coercivity values and limited maximum saturation values NMT 100 emu/g even at similar concentration with 25 mL concentration of reaction media (i.e. NaOH, [Metal]. With concentration not acting as a most significant factor, the nature of the reaction vessel was examined. During the course of a reaction, it was observed that the cylindrical (and mounted vertically) reaction tube actively collects condensation as the reaction process starts to occur. This general dehydration mechanism was explained in part previously in chapter 1, figure 1.9. As the condensate (water) builds up, it can become reintroduced into the reaction media in particular by the vertical magnetic stir bar as it constantly splashes the reaction mixture, see (b) in figure 3.8 depicting the two relative volume heights with the magnetic stir bar range. The 25 mL volume is at sufficient height for the magnetic stir bar to not disturb the reaction media surface. Water is well known to catalyze oxidation of Fe to ferrite and promotes the CFO formation observed.⁵⁷ The magnetic property distribution of samples produced using 25 mL volumes is given in the right side of

figure 3.8 and indicates a linear trend from saturation values up 200 emu/g and H_c less than 200 Oe, still far from the theoretical maximum saturation values of FeCo which have been reported well over 240 emu/g for bulk samples for Fe:Co 65:35 atomic ratio.² In order to address this issue, a one variable at a time (OVAT) local optimization study was performed by running reactions at 25 mL volumes. Ranges of M_s values are shown with averages against total metal concentration and hydroxide concentration in figure 3.9.

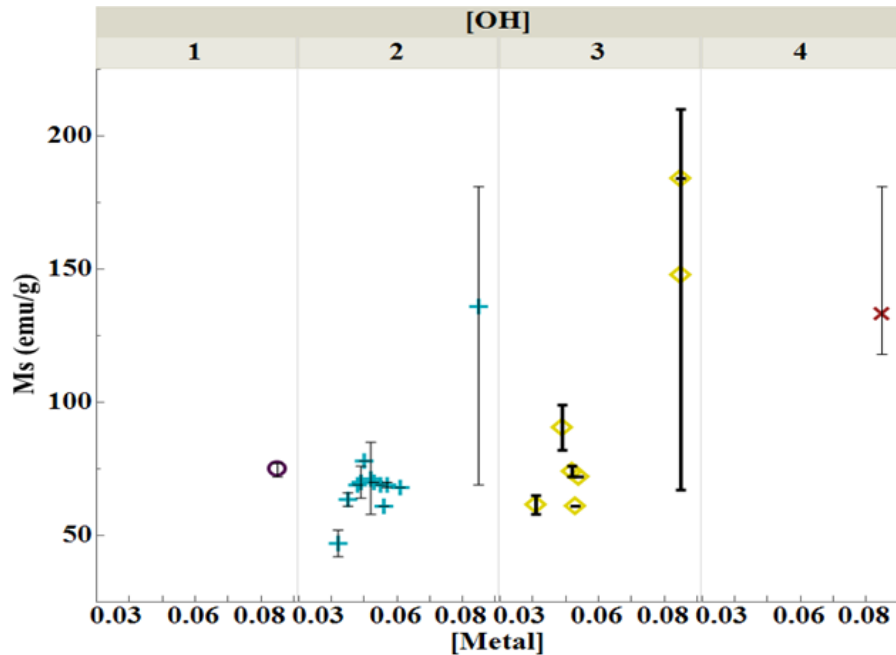


Figure 3.9. Variation of [OH] with [Metal] and M_s (emu/g) showing [OH] \approx 3 and [Metal] \approx 0.1 to produce highest saturation values of FeCo-rich samples. Range bars shown.

Figure 3.9 indicates highest M_s values achieved using 3 M OH and values near 0.09 [Metal] however they ranged from 70-205 emu/g. Exploration on how to maintain consistent yet high saturation magnetization values (over 200 emu/g), that is with minimal variability had to be employed for purpose of understanding how to achieve phase control.

Perhaps one of the most significant findings of this work was the reduction in variability in M_s and well as the achievement of high M_s values regardless of the $[OH]$ and reaction time when metallic precursor premixing treatments were performed shown in figure 3.10 (a) and (b).

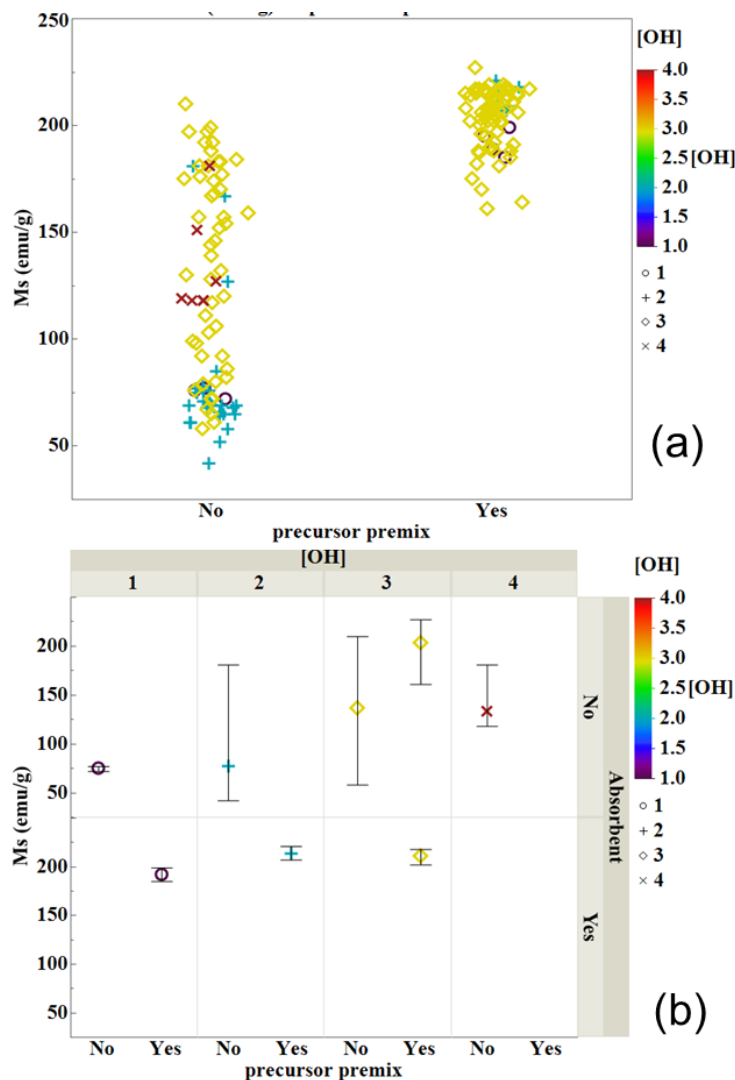


Figure 3.10. Metallic salt precursor premixing with saturation magnetization in (a) and variation in $[OH]$ with M_s (emu/g) with precursor premixing and condensation absorbent presence in (b). $[OH]$ is color-coded with symbols in (a) and (b). Std. error bars shown.

Figure 3.10 (a) shows the overall improve in range of M_s values obtained when premixing of the metallic salts in ethylene glycol is performed prior to running the reaction mixing all reactants simultaneously. This minimization in M_s variation is also shown to be insensitive to $[OH]$ in the

range of 1-4 M in figure 3.10 (a) while plot (b) again shows the enhancement of M_s by using an absorbent option when running the reaction. Several more reactions were performed with 3 M [OH], 0.09 M [Metal], using optimal precursor premixing times and temperatures around 60 minutes and 80 C were performed at 25 mL reaction volumes with varying reaction times from 15 – 45 minutes (temperature always kept and held at 150 C never in excess due to PTFE vessel malfunction) with data shown below in figure 3.11.

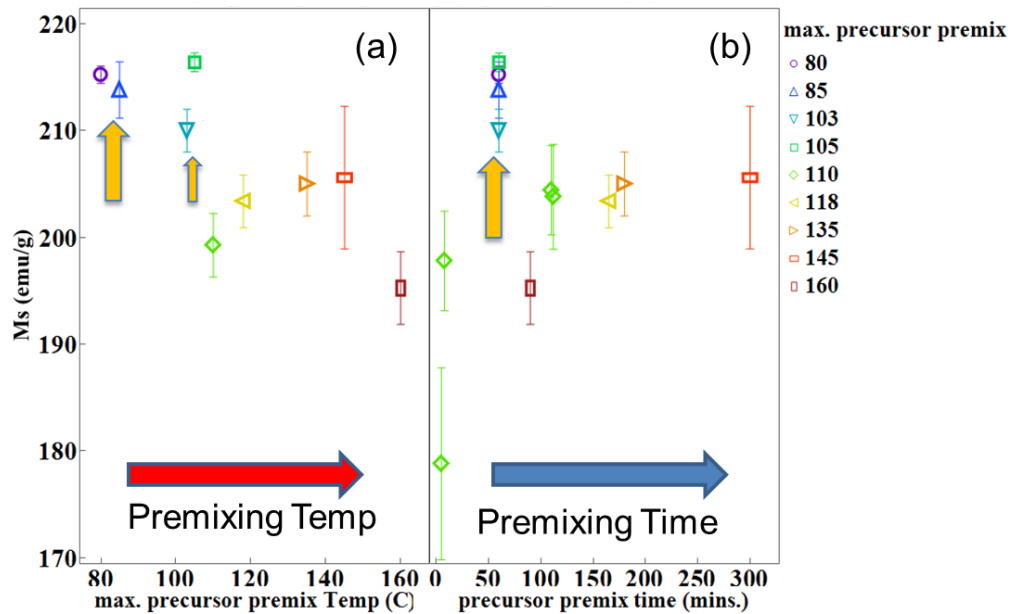


Figure 3.11. Maximum precursor premixing temperature (°C) in (a) and premixing time (minutes) in (b) with M_s (emu/g). Symbols shown for precursor premixing temperatures

Below from figure 3.12, it is apparent that the lowest reaction times (with reduction still occurring) produced the highest M_s values. In addition, there was a slight enhancement observed above 215 emu/g when moisture control was employed. Longer reaction times promoted lower M_s values and likely greater percentage of cobalt ferrite nanomaterial.

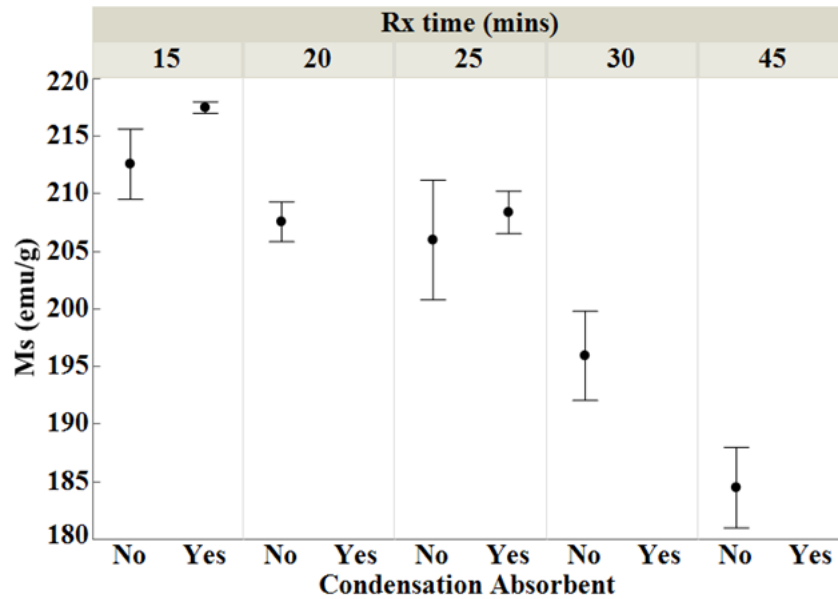


Figure 3.12. Variation of Rx time (mins) with M_s (emu/g) showing shorter reaction times around 15 minutes ideal for producing highest saturation values of FeCo-rich samples. Condensation absorbent presence gives M_s enhancement as well. Std. error bars shown.

These results altogether indicate shorter reaction times as favorable for synthesizing FeCo-rich nanomaterial. With hydroxide kept at 3 M, [Metal] at ≈ 0.1 M, reaction times at around 15 minutes, moisture control with absorbent and incorporation of proper precursor pretreatments (60-minute premix duration at 80 C), consistently high M_s values (over 200 emu/g) were achieved and demonstrated in this work.

In order to compare M_s values with % composition of FeCo phase, XRD phase compositions were acquired at various saturation magnetization values reported and plotted in figure 3.13. M_s values correlate linearly with increasing FeCo % as to be expected while the lowest values approach the theoretical limit for cobalt ferrite at above 80 % cobalt ferrite in figure 3.13. The coercivity was plotted with the same compositions generating a negative correlation up to around 80 % cobalt ferrite where different particle sizes and relative crystallinity are responsible for the variation between H_c values.

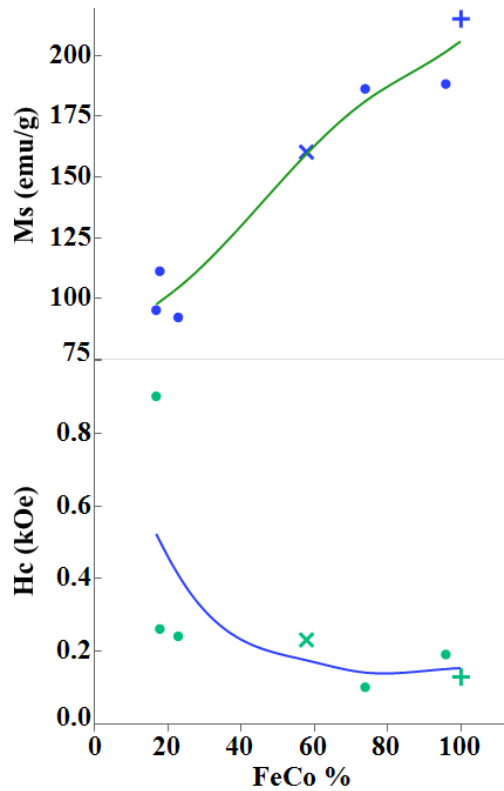


Figure 3.13. Relationship between FeCo alloy (determined by XRD) with magnetic properties of Ms (emu/g) and Hc (kOe).

Figure 3.14 (a) shows all reactions (≈ 250) performed using the high throughput experimentation with data points plotted representing their magnetic property relationships. From this X-Y plot, two local hot spot regions are highlighted, namely FeCo-rich nanomaterials represented by TEM image (b) and cobalt ferrite-rich nanomaterials represented by TEM image (c), figure 3.14, where both images show unique and distinguishable morphologies. In (b) of figure 3.14, high aspect ratio structures were observed in several sample sharing similarly high Ms values (dashed blue circle) and in (c) a few samples were plate-like structures (dashed yellow circle) of cobalt ferrite having high Hc values up to 900 Oe while samples with lower values of both properties indistinct particle morphologies in terms of phase as imaged by TEM in figure 3.5.

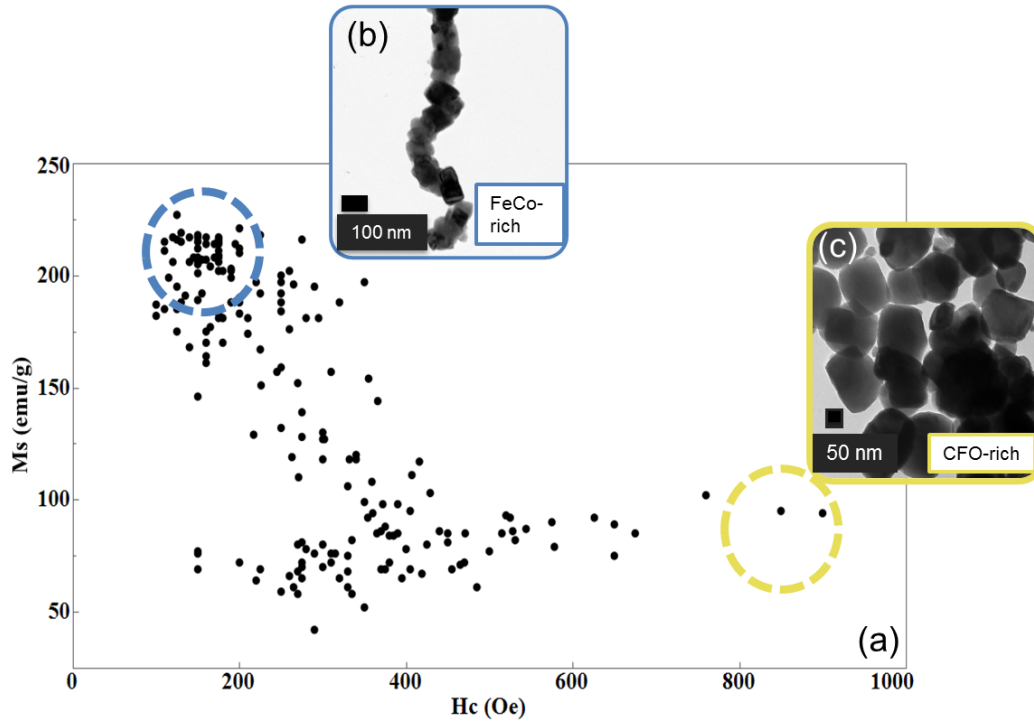


Figure 3.14. M_s (emu/g) versus H_c (Oe) of >200 reactions (a) indicating the overall magnetic property distribution between FeCo-rich (b) and CFO-rich (c) samples as well as morphological difference.

Using the magnetic property of M_s , and to some extent H_c , have been shown to prove meaningful in estimating and ultimately predicting phase composition for high throughput experimentation studies. FeCo-rich specimens were routinely synthesized once the controllable independent variables were understood. The first major environmental factor was the reintroduction of water into the reaction media. H_2O from condensation promotes oxide formation due to catalysis of Fe to iron oxide. The H_2O when introduced onto an Fe atom surface by adsorption, formation of an adsorbed hydroxide and hydrogen. If the temperature is above 107 C, then evolution of hydrogen gas may form leaving oxygen to adsorb with the Fe surface.⁵⁸ This process occurs on the Fe-based nanomaterials synthesized in this work when water is present in the reaction media and the oxidation is accelerated at elevated temperatures

such as the 150 C temperature used in this work. Compounding this issue, is the high overall surface area of the nanoparticles produced which provide increased surface adsorption sites.

3.5 Conclusion

Polyol reactions were performed using high throughput experimentation where several reactions were run simultaneously to synthesize FeCo and cobalt ferrite with the initial goal of synthesizing FeCo as a pure phase followed by enhancing the saturation values. CFO plates were synthesized having high coercivities up to 900 Oe by promoting accelerated oxidation with the constant reintroduction of condensation from the reaction. This was achieved with excessive splashing of the reaction media due to small volumes creating turbulent agitation cycles. FeCo structures above 200 emu/g were achieved by monitoring and controlling the precursor premix treatment conditions as well as initiator, total metal concentration and reaction time and control of condensation reintroduction. In addition, unique high-aspect ratio morphologies were observed in the FeCo-rich samples.

The large number of iterations in this work led to interesting morphologies having useful magnetic properties as well as an understanding of control of phase by tailoring the chemistry. It is still unclear as to how omnipresent the high aspect ratio FeCo structures were based on scarcity of findings from microscopy. Furthermore, the linear arrangement of FeCo particles is not well understood and requires confirmation of morphological continuity. Therefore, the goal of the next chapter is to answer these questions to confirm that the structures are not artificially generated post-synthesis by inadvertent magnetic alignment of the FeCo particle solution on a TEM grid or interparticle alignment via particle moments.

Chapter 4. Synthesis of High Aspect Ratio Fe₁Co_{1-x} Nanostructures

4.1 Overview

The motivation for this work is tied from the work performed in chapter 3 relating to the observation of high aspect ratio FeCo structures at the high Ms data points. These peculiar structures require structural confirmation through reproducing optimized syntheses of highly magnetic FeCo alloy particles. If successful, observation of the FeCo linear structures should be vast, rather than seldom observed by microscopy techniques as in chapter 3. In addition, a thorough structural characterization by FIB as well as a thermomagnetic study for monitoring phase change and structural change during and after annealing was sought. These questions, along with probing the formation of the linear FeCo structures, required a deeper understanding and leads the pursuit of their exploration in this chapter.

4.2 Introduction

As mentioned previously, FeCo alloy is a premiere soft magnetic material with unsurpassed magnetization induction at room temperature, high Curie point, low hysteresis and low eddy current loss.¹⁴ These properties are suitable for transformer core applications as well as magnetic switching devices.^{14,59} Forming morphological control using wet-chemical methods such as the polyol process in this work is not commonly reported where most observations are typical cubic structures as explained previously in chapter 3.²⁴ Further, this lack of morphological control in bottom up syntheses somewhat limits understanding of tailoring FeCo magnetic properties in non-cubic morphologies.

High aspect ratio structures such as nanowires of Ni and Co have been synthesized in the past showing interesting properties where coercivities of Co NWs were reported well above 2000 Oe based on orientation to the measuring field.^{60,61} These synthetic approaches involve either

electroless deposition of Co NWs on a substrate to porous aluminum membrane (PAM) template-assisted growth of Ni nanowires.

In particular, self-assembled chains of Co nanoclusters, or Co nanowires, have been demonstrated by template-free routes using an external magnetic field where the easy axis of the Co aligned to the direction of the magnetic lines of force.⁶² The diameters of the cobalt nanowires were approximately 500 nm, far larger than 100 nm which is a typical size limitation when referring to materials as having nanoscale dimensions. High aspect ratio structures of FeCo nanowires embedded in carbon nanotubes has been synthesized where the authors claim high coercivities up to 1 kOe although these FeCo nanostructures have the magnetic impurity of carbon encapsulation leading to lower overall moments.⁶³

The formation of high aspect ratio linear chains of FeCo alloy was realized in conclusion of the work in chapter 3 however questions remain on how the chains were formed as well as the need to fully characterize the chain structure physically, thermally and magnetically. This work aims to explain and develop these findings as well as provide details on the synthetic approach used to produce these interesting nanostructures.

4.3 Experimental

The optimal synthesis for FeCo MALCs was determined after several trials and involves the following two-step preparations:

4.3.1 FeCo Precursor Solution Preparation

The hydrated salts of Iron(II) chloride tetrahydrate and cobalt (II) acetate tetrahydrate

were massed and placed in a round bottom flask containing ethylene glycol for a total [Metal] concentration of NMT 0.7 M and a molar ratio of Fe:Co of approximately 1.5. Heating of the precursor solution A should be gentle and kept below 80 C to avoid excessive oxidation of the Fe^{2+} to higher oxidation states. This thermal pretreatment (i.e. accelerated dissolution) of precursor solution A should be performed for at least 1 h with magnetic stirring to ensure complete dissolution until a translucent fuchsia solution color was observed. If the resulting solution produces a yellow to brown color, then either water contamination or O_2 introduction or both have occurred. The process must be restarted if this problem occurs.

4.3.2 Synthesis of FeCo MALCs

Using a 25 mL class A pipette, 25 mL of the FeCo precursor solution (cooled to room temperature) was aspirated and transferred immediately to a nitrogen purged PTFE reaction vessel mounted onto a surveyor process synthesizer shown below in figure 4.1.

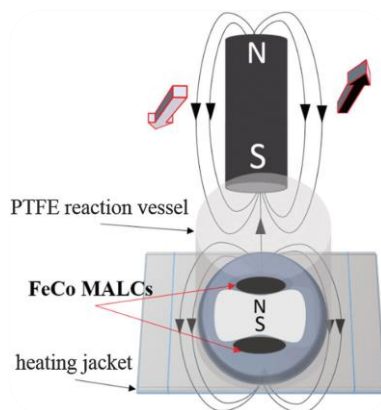


Figure 4.1. Reaction vessel (Argonaut process synthesizer) scheme used to produce magnetically aligned linear FeCo chains via polyol via high throughput process synthesis. Oscillating permanent magnet shown provides the external field as well as vertical magnet stirring.

Vertical magnetic stirring was initiated immediately after addition of precursor solution as well as gentle nitrogen bubbling using a rotameter. Every vessel possessed a dimension of

approximately 1 x 8 inches and all were equipped with K-type thermocouples at the reaction vessel base and temperature controlled heating elements that maintained direct contact with reaction media levels up to the first 30 ml. To the 25 mL of FeCo precursor solution, dry NaOH in pellet form was cautiously added to give a molarity of [OH] equal to approximately 3.5 M. Increasing the [OH] inhibits the vertical magnetic stir bar action. Temperature ramp rate should be kept in the range of 8-13 C/minute and the total reaction time should be in the range of 15-25 minutes depending on ramp rate used, with high rates ideal for shorter reaction times and vice-versa. The final temperature should be kept at 150 C never to exceed due to damage caused of the PTFE reaction vessel system and excessive oxidation of the FeCo nanomaterial. Condensation due to the reduction process should be carefully controlled used cotton absorbent preloaded into reaction tube before reaction start. This will prevent reintroduction of water into the reaction media which adversely affects the quality of the FeCo MALC nanomaterial as shown in chapter 3.

4.3.3 Characterization

X-ray diffraction analysis was performed on a MPD Panalytical X-ray diffractometer equipped with a Pixcel detector and Cu K α X-ray source ($\lambda=1.54 \text{ \AA}$). The FeCo powders were magnetically aligned using a rare earth magnet to where the length of the chain was either parallel or perpendicularly oriented with respect to the incident x-ray source. A low back ground silicon wafer was used to prevent unwanted parasitic diffraction from the substrate. The receiving slit and anti-scatter slit were set to 1 degree and the programmable divergence slit was set to 0.5 degree as a fixed slit width. A 15 mm mask was used as well. The scan range as from 20-90 to account for all major peaks of FeCo bcc and any oxides such as cobalt ferrite if present.

HT-XRD (high temperature XRD) was done by using an Anton-Paar 1200-N oven mounted into the XRD. The oven was capability of reaching 1200 C though up to 727 C was required for this work. The sample was added to an alumina substrate, making sure to fill the entire well to avoid parasitic diffraction and mounted finally inside the oven. A nitrogen stream purged the chamber for 15 minutes prior to analysis. The diffraction patterns were acquired as the temperature increased at a similar ramps rates to the VSM thermomagnetization measurements explained later. Sample height adjustment due to thermal expansion of the heating element was performed by using beam bisection of the total signal at each temperature interval.

TEM imaging was performed on a Zeiss Libra 120 operated at 120 keV. The powder sample was drop-casted on to a 300 mesh Cu formvar-coated TEM, dried for 10 minutes repeating the drop-casting procedure three times. The sample was vacuum dried for at least 24 hours prior to imaging. BFTEM images were acquired as well as selected area diffraction pattern of the FeCo sample. This was performed by inserting the SAED aperture to the sample-region of interest following the diffraction protocol. The SADP was acquired using a camera length of 283.5 mm working in overview mode at 0.33 in order to account for all major Bragg reflections within the digital SADP image.

Morphology studies were performed on a Hitachi SU-70 FE-SEM operated at 5 keV. A back-scattered detector was used to enhance contrast of the sample. Another SEM, Zeiss Auriga FE-SEM with FIB capability was used to perform the focused-ion beam milling of the FeCo chain sample. The was begun by locating a suitable area of the sample first, then perform milling in a trapezoidal-ramp configuration to at a sufficient angle to allow for detected by SEM imaging modes. The milling process took about 1.5 hours following fine milling steps to create a smoother cross-section. No lift-off technique was performed as the cross-section was able to be

imaged using TEM alone, in addition, the relative stability of the linear chains was compromised as they were as a freely stacked powder.

Magnetization studies were performed using a Quantum Design Versalab magnetometer capable of 3T fields and temperature in the sample chamber down to 50 K and as high as 400 K. Typical M-H curves were acquired of the FeCo by massing into a polypropylene capsule, centering the sample onto a low magnetic signature brass sample holder following mounting onto the sample rod and insertion into the VSM. M-H curves were acquired using the full field range of the VSM (-3 to 3 T) and were acquired at several temperatures. M-H curves performed at 50 and 300 K on the as-synthesized powders were mounted into capsules while measurements at 1000 K (Oven mode) and 300 K after annealing were done by mounting the sample onto a lithographic heating element. Zirconia paste was used to secure the sample followed by carefully wrapping the sample using pristine Cu foil over the heating element.

4.4 Results and Discussion

A successful reaction of FeCo synthesized MALCs (magnetically aligned linear chains) should form FeCo alloy as pure phase having high aspect ratios linear chain-like morphology as displayed in SEM image in figure 4.2 (a).

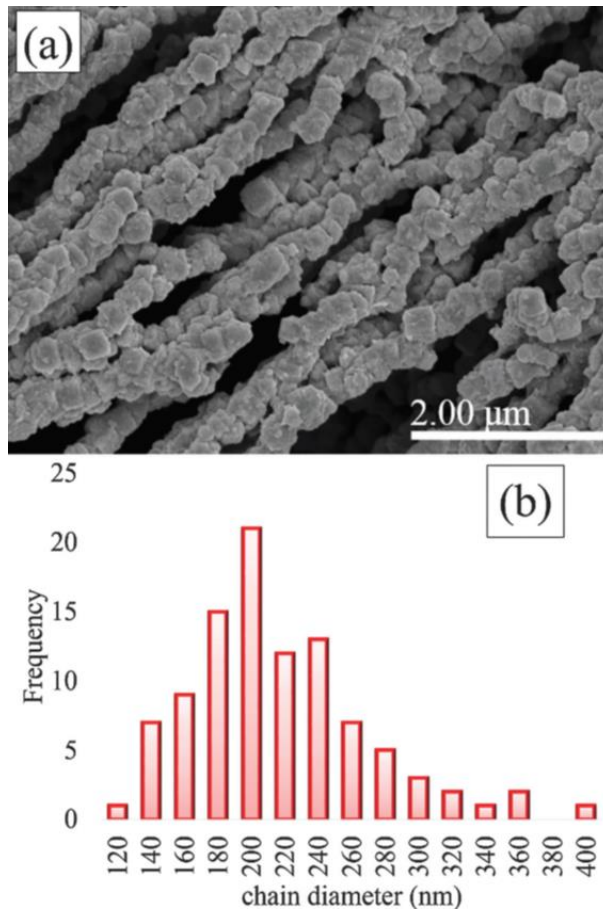


Figure 4.2. SEM image of FeCo MALCs (a) with chain diameter distribution shown in (b). Average chain diameter was about 220 nm for the sample shown in (a).

Aspect ratios varied widely from chain to chain and were hard to measure but typically range from 10:1 up to 25:1 with average diameters ranging from 150-250 nm. From figure 4.2 (b), this particular batch of as-synthesized MALCs possessed an average diameter of about 200 ± 30 nm indicating a rather large diameter distribution. Size control was not achieved nor was a goal of this work however it is reasonable to ascertain the difficulty in maintaining monodisperse diameters in this polyol process format without the aid of nucleation agents to promote particle size control. Average particles diameters of FeCo have been reported lower than 100 nm using noble metals as nucleation agents.²⁵ In order to further characterize the interior microstructure of

the FeCo MALCs, FIB cross-sectioning was performed using Ga ions and carefully controlled milling current to not damage the freely stacked FeCo MALCs.^a

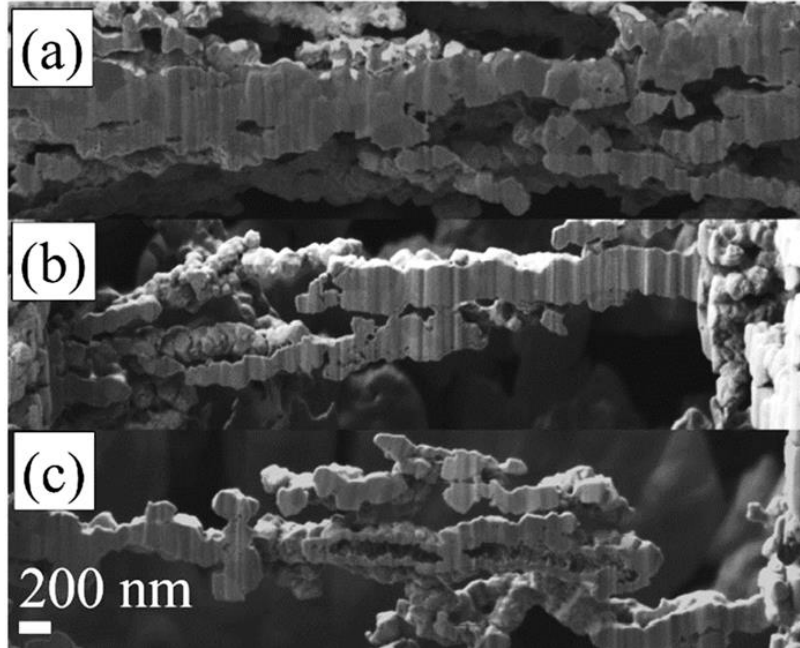


Figure 4.3. SEMs showing tangential cross-sections by FIB displaying the various crystallite orientations and microstructure within the FeCo MALCs. MALCs are shown consisting of segmented FeCo particles rather than continuous or high-aspect ratio FeCo crystallites.

The tangential cross-sections shown in (a-c) of figure 4.3 indicate random orientation of FeCo crystallites forming a linear parent structure or chain where contrast is slightly enhanced in (a) using back-scatter detection. An important observation is the discontinuity of the FeCo chains by distinct but fused, FeCo particle segments. This morphology gives a clue as to nature of formation into chain structures since the particle segments are grown into-or embedded-into one another.

TEM imaging was performed on the same sample of FeCo MALC and is shown below in figure 4.4 with BFTEM in (a) and SADP in (b) confirming the presence of the FeCo bcc alloy with the (110), (200) and (211) Bragg reflections indicated.

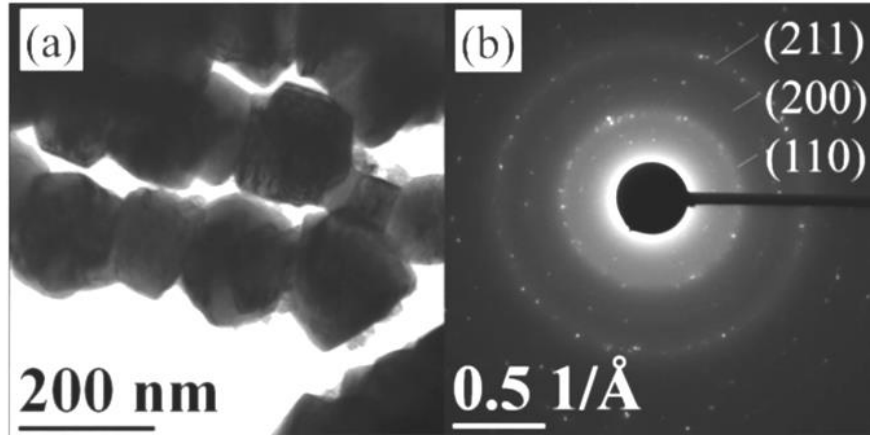


Figure 4.4. BF-TEM image of FeCo MALCs in (a) and corresponding SADP in (b) indicating the (110), (200) and (211) planes of FeCo bcc.

Similar microstructure is observed in figure 4.3 (a) corresponding to the FIB cross-sectioning discussed previously where the chains consist of multiple FeCo particles grown or attached together. These morphological observations indicate that nuclei for FeCo first form and align when they possess a significant volume magnetization following particle ripening and subsequent formation of converged linear arrangements or assemblies. Similar wire formation mechanisms have been observed for Co microwires using the polyol method with magnetic field assistance though they possessed much larger diameters up to 1-2 μm in diameter with questionable control over morphology.⁶⁴

Experimentation with two orientations of the FeCo with respect to the XRD beam path was performed with both diffractograms shown in figure 4.5 where (a) is a parallel orientation of the FeCo MALCs to the beam path and (b) is a perpendicular orientation to the x-ray beam path (top-down view). The MALCs were aligned using a rare earth magnet onto a low background Si wafer. The orientation in (a) has a slightly broader peak at $45^\circ 2\theta$ indicating and slightly higher $^\circ 2\theta$ position than the perpendicular orientation (see inset in figure 4.5). This is likely due to higher inter-particle surface area in the parallel orientation having slightly increased

incident x-ray scattering thus slightly reducing the diffraction intensity of the peak at 45 2θ as compared with the same peak position in orientation (b).

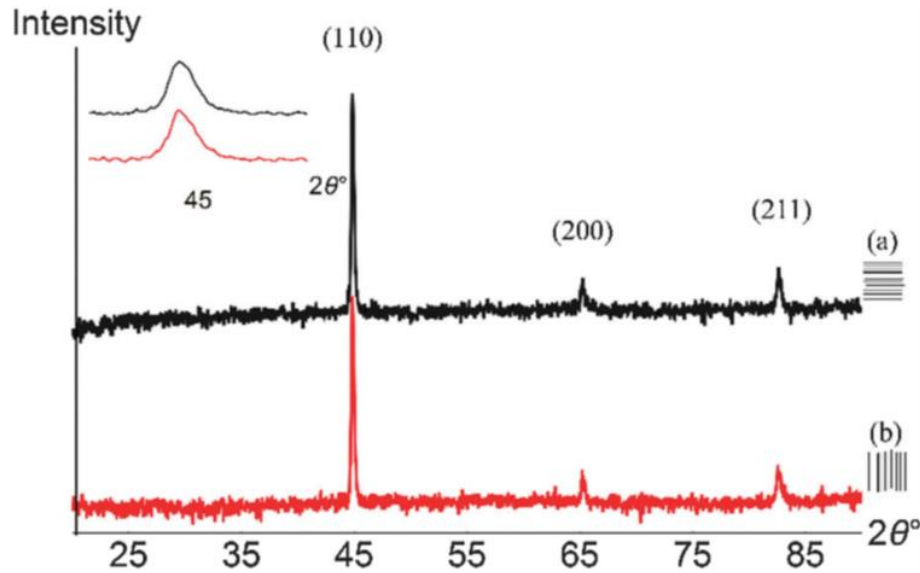


Figure 4.5. XRDs of magnetically oriented FeCo MALCs with respect to the incident X-ray path, parallel to x-ray path in (a) and perpendicular to x-ray path in (b). Both orientations provide similar peak position and intensities indicating low to no intra-particle anisotropy.

FeCo bcc phase was confirmed where the (110), (200) and (211) peaks are shown in the XRDs from figure 4.5 with no evidence of iron oxide impurities.

Magnetic characterization by obtaining several M-H curves at various temperatures was performed on the MALCs (as-synthesized) at 50 K, 300 K, annealed at 1000 K and 300 K after cool-down and are given in figure 4.6. At 50 K the magnetic saturation is 209 emu/g which is slightly higher than that of 205 emu/g at 300 K explained by the gradual increase in saturation magnetization versus temperature relationship of Bloch's Law for pure Fe disks where a similar 2.5% decrease in M_s is observed from 2 to 300 K.⁶⁵ Less thermal energy is present at low temperatures minimizing spin disorder in the ferromagnet.

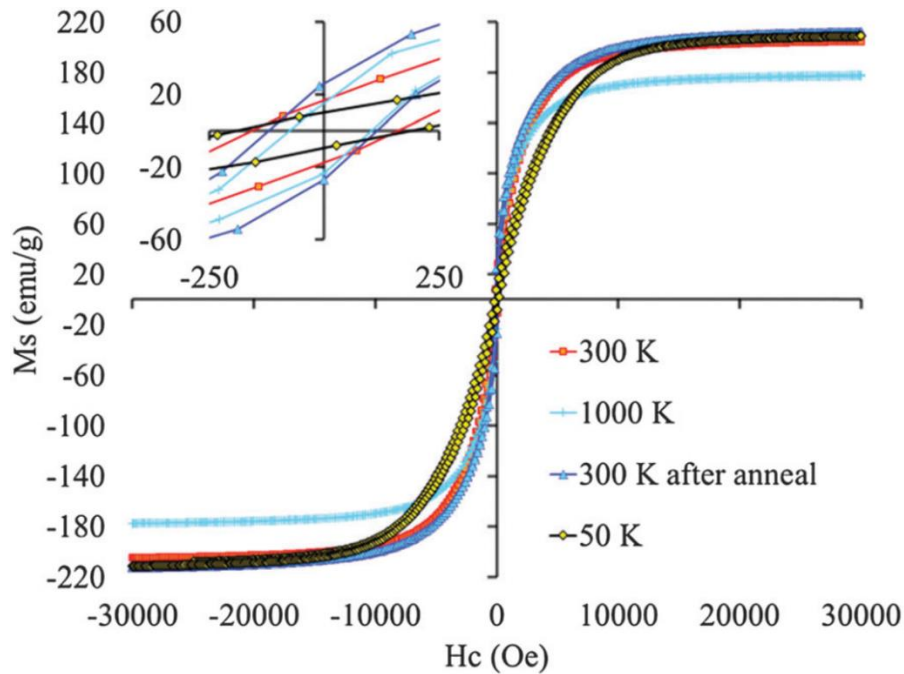


Figure 4.6. VSM hysteresis curves acquired at 300 K (red/square), 1000 K (light blue vertical line), 300 K after anneal (blue/triangle) and separate sample prep of same batch at 50 K (yellow/diamond) of FeCo MALCs.

At 1000 K, the saturation magnetization decreases significantly due to the thermal activation present which promote spin disorder and subsequent measurement of Ms at 300 K after cooldown resulted in a higher value of 212 emu/g, a 3.4 % increase. This is an effect from annealing the MALCs and promoting an enhanced distribution of Fe and Co to form the ordered α^1 transition and shown previously in the Co-Fe phase diagram in figure 1.7 of chapter 1.¹⁰ In addition, removal of any residual solvent from the zirconia paste and synthesis may have occurred as the annealing treatment was performed under high vacuum which may decrease the mass of the sample during the hysteresis measurement at 1000 K. Thermomagnetic measurement of FeCo MALCs monitoring the temperature dependent susceptibility, $\chi(T)$, was performed with magnetization plot given in figure 4.7. As the magnetization was recorded with increasing temperature from 300 K to 1000 K (maximum T of the VSM oven), multiple

magnetization steps were observed which required a careful analysis of the Co-Fe phase diagram for data interpretation.

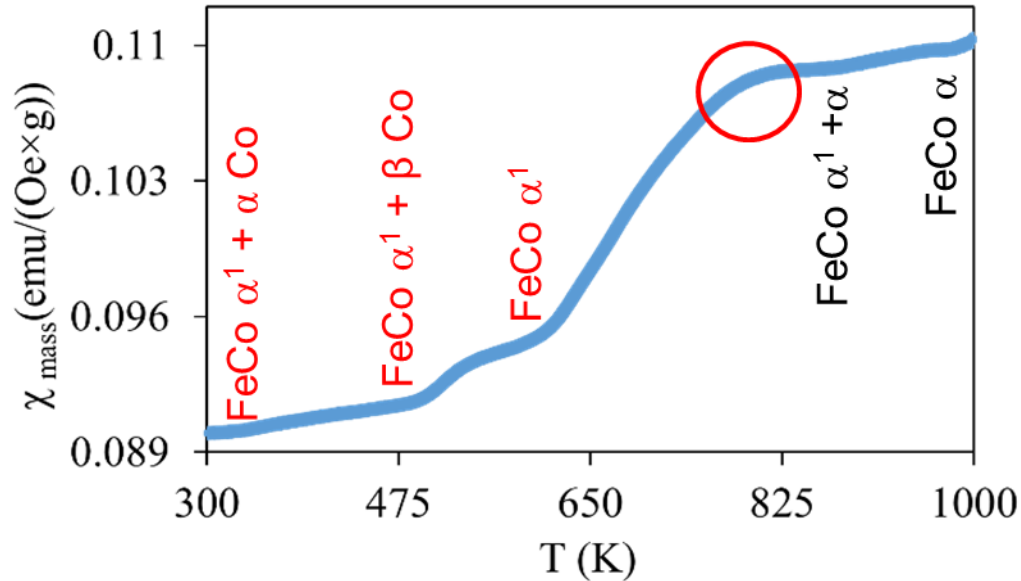


Figure 4.7. Thermomagnetic analysis of mass susceptibility χ_{mass} measured from RT to 1000 K of FeCo MALCs with magnetization steps indicating presence of two FeCo compositions, ≈ 68 and ≈ 40 atomic % Co. (Refer to Co-Fe phase diagram for highlighted corresponding phase changes in Ch. 1) Red circle $\approx 770\text{K}$ indicates unknown phase change.

From figure 4.7, steps in M are observed at just above 325 K, 500 K, 600 K, 775 K, 875 K and 985 K. Using the Co-Fe phase diagram and the observation of Fe-rich (cubic) and Co-rich (spherical) FeCo crystallite formation, in other words, presence of two compositions, the nominal Fe:Co atomic ratio of 60:40 and the other at 32:68. Presence of these two Fe:Co compositions are supported by the magnetizations steps where there is a transition from hcp Co/FeCo α_1 to (fcc) β Co/FeCo α_1 at 500 K and to the higher moment FeCo (B2) ordered structure α_1 at 600 K for Co rich segments $\text{Fe}_{32}\text{Co}_{68}$. The decrease in the M 775 K was not clear by simply referring to the Co-Fe phase diagram alone and required further analysis discussed later in this chapter. The small step at 875 K is from the initial transition into the (A2) disordered FeCo structure for a $\text{Fe}_{32}\text{Co}_{68}$ composition. The major composition of $\text{Fe}_{60}\text{Co}_{40}$ undergoes a single

phase transition from α_1 to $\alpha \approx 975$ K well below the Curie Point, T_C , for this composition at > 1200 K.

In order to investigate the step in magnetization or decrease rate of magnetization change at 775K from figure 4.7, HT-XRD was employed to monitor significant phase changes at an elevated temperature up to 1000 K shown in figure 4.8. Around 500 C or 775 K, formation of an iron oxide phase, specifically wustite, or FeO, was observation on through 1000 K. After cooling to room temperature, presence of the FeO phase remained.

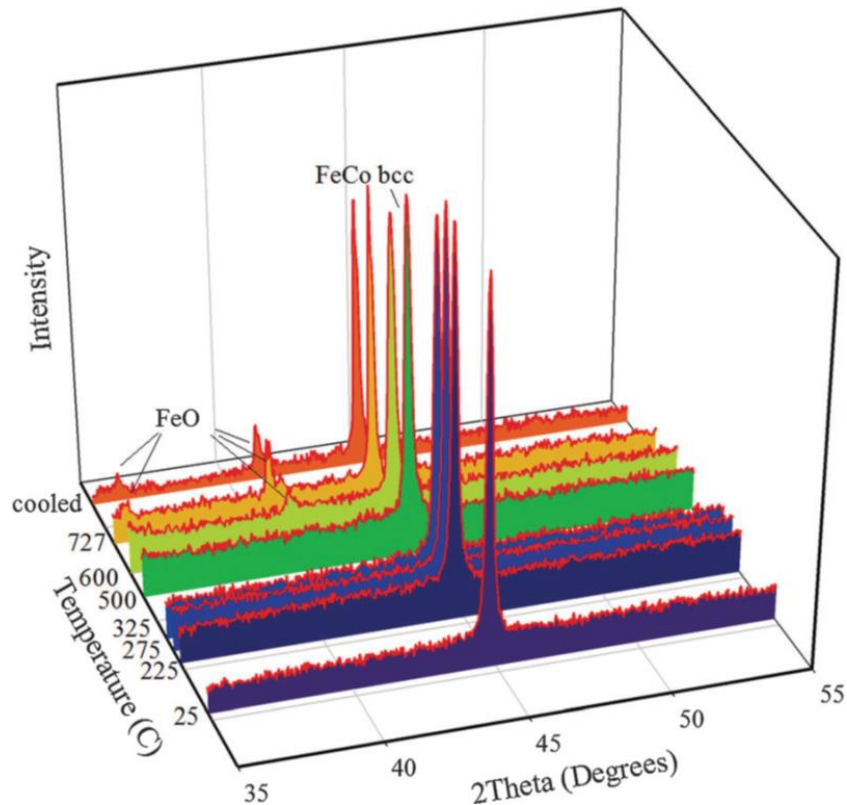


Figure 4.8. HT-XRD waterfall plot of diffractograms acquired in order of increasing temperatures at 25 C, 225 C, 325 C, 500 C, 600 C, 727 C and 25 C (cooled) indicating formation of cubic FeO (wustite) at about 500 C.

This formation of FeO in the FeCo MALC corresponded with the decreased rate of change of magnetization in figure 4.7 and is explained by a dilution of Fe from the $Fe_{60}Co_{40}$ major

composition that is present in the MALC sample. This removal of Fe further decreases the moment of the FeCo deviating the composition from the Slater-Pauling limit for FeCo alloy at 1.8:1 Fe:Co atomic ratio.² The annealed sample at 1000K was imaged by SEM to study any morphology changes as shown in figure 4.9. From the SEMs in (a) and (b), figure 4.9, it is clear a phase transition had occurred by the observation of several crystallites on the surface, in addition, the FeCo MALCs formed into continuous microwires.

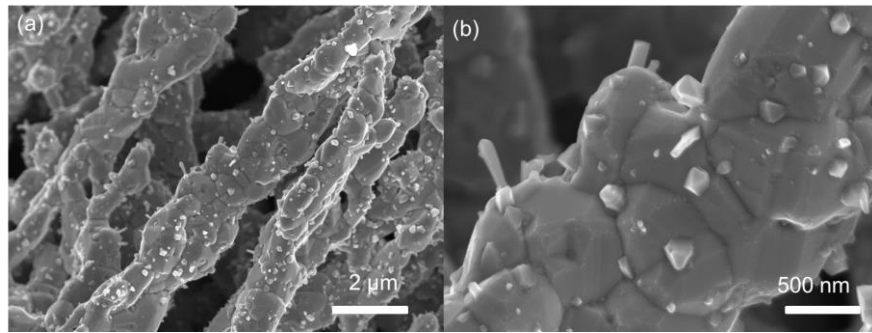


Figure 4.9. SEM images of FeCo continuous microwires formed from FeCo MALCs after annealing at 1000 K for 30 minutes in (a) and FeO crystallites formed on surface in (b).

The crystallites observed by SEM correlated with the FeO phase formed in the HT-XRD from figure 4.8 and are shown as having enhanced contrast or charging effects-another clue of oxide formation. To confirm oxide presence, point analysis by EDS (energy dispersive spectroscopy) was performed on a crystallite and on the FeCo microwire surface shown in figure 4.10 (a & b) and (c & d)

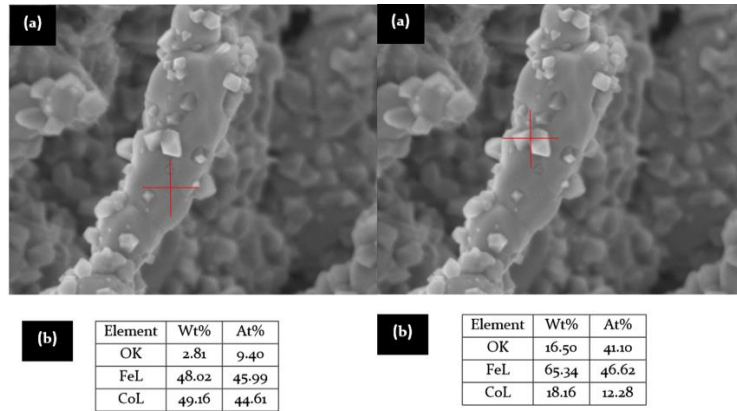


Figure 4.10. EDS point analyses of a FeCo microwire in (a), with EDS results in table (b) and of a FeO crystallite in (c) with EDS results in (d) showing varying O content.

A simple study to determine the formation mechanism of FeCo MALCs was performed. This test involved performing the MALC synthesis as given in the experimental with (a) presence of external oscillating magnetic field and (b) removal of all proximal magnetic fields, including the magnetic stir bar, relying simply on mechanical stirring for agitation with the SEM images of the synthesized materials given of each synthesis in figure 4.11. Formation of a well-formed FeCo chain is shown in (a) for comparison with the observance of no high ratio structure formation in (b). This indicates the necessity of an external magnetic field to form the FeCo linear chains.

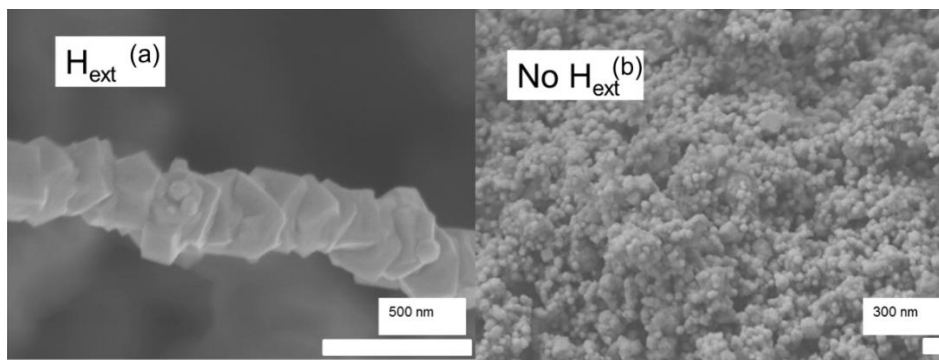


Figure 4.11. SEM images of a single FeCo MALC synthesized in an external field (a) and FeCo particles synthesized with no external magnetic field in (b). Both samples were synthesized from the same experimental conditions.

As mentioned previously in the microscopy portion of the results section, nuclei of FeCo first form and align within the magnetic flux lines of the oscillating AlNiCo magnet. As the particles begin to grow, they come together further continuing to grow into larger particles with interfaces embedded. This phenomenon locks each segment into place forming the chain structure.

Routinely, two distinct morphologies of FeCo nanoparticles are observed and discussed in literature: particles of a cubic shape possessing an Fe-rich (ordered) structure and particles with a spherical shape possessing Co-rich crystallites.^{66,67} To confirm the overall composition of FeCo, EDS was performed with summarized data given in figure 4.12 (b) taken at low magnification in region (a).

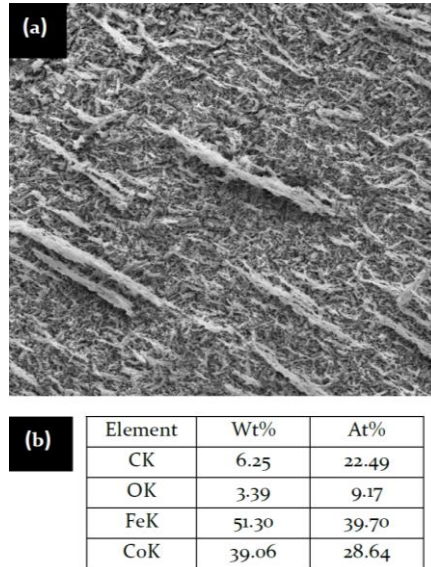


Figure 4.12. EDS data taken of FeCo MALCs indicating an average composition \approx Fe₅₈Co₄₂.

Similar high saturation values have been reported where 200 emu/g was achieved the FeCo MALCs in this work routinely possess higher vales up to 215 emu/g. With Ms values at \approx

90 % of the bulk theoretical value for FeCo (240 emu/g) while MALC diameters are well into the nanoscale range at 200 nm, shape anisotropy due to the elongated structure is compensating for the magnetization. These high aspect ratio nanostructures act as nanomagnets with oppositely polarized ends that direct and minimize stray magnetic flux throughout the length of each MALC-magnet. Proper compaction with thermal treatment and alignment of the FeCo MALCs can produce an enhanced overall magnetic anisotropy where the well-aligned grains may reduce the demagnetization, or magnetostriction energy, from within each chain. This effect will promote an enhanced permeability as well as higher saturation induction values for transformer core application at both low and high frequencies.

It is important to mention that the absence of pure Fe was confirmed as there was no knee observed from the magnetization curve near 1000 K where Fe has Curie point at around 1043 K much less than that of Co at 1043 K.² The FeCo MALC structures are expected to have magnetic anisotropy due to their high aspect ratio where a change in the MS values based on orientation to an external field should be observed, though no such study was performed (This magnetic anisotropy study was performed on high aspect ratio cobalt ferrite micropillars in chapter 6).

4.5 Conclusion

The goal of this work was to control the synthesis of linear chains of FeCo and examine their structure as well as magnetic properties at ambient and elevated temperatures. Linear chains of FeCo alloy discovered by OVAT-THE in chapter 3 were successfully synthesized in this work as a well-distributed high aspect ratio morphology with overall uniformity and carefully characterized using as many techniques as possible. The high throughput

experimentation in combination with presence of an external magnetic field led to these intriguing nanostructures.

The following chapter will attempt to further refine and control the size in one dimension of the FeCo MALCs. This will be done to indirectly control or manipulate the magnetic properties of the FeCo chains.

Chapter 5. Size control of Fe_xCo_{1-x} Chains using Nucleation Agents by DOE

5.1 Overview

Structural and magnetic characterization performed extensively on the FeCo linear chains in chapter 4, provides a satisfactory understanding of the chain formation or assembly as it may be referred to, which highlighted the morphological changes at high temperatures caused by phase transformation. Armed with this knowledge on FeCo linear chains, a final goal was to statistically control the physical properties of diameter (nm) and average crystallite size (nm). This work was to be completed using a DOE (design of experiments) in order to demonstrate statistical control of responses. Size control will be performed using nucleation agents.^{24,25}

5.2 Introduction

FeCo alloy nanomaterials offer unique properties as magnetically soft ferromagnets including high permeability (responsivity to an external field) and the highest saturation values (2.4 T, or 240 emu/g Fe:Co 80:20 at%) at room temperature of any ferromagnetic material known while having low magnetocrystalline anisotropy ($K_1=0$).^{3,68} Several applications based on the FeCo alloy system include high performance transformers, solenoid valves, transducers, starters and generators where usage in “more electric aircraft” (MEA) technology is increasing.⁶⁸ The MEA concept is based on conversion to all electric aircraft as opposed to mechanical and pneumatic devices. This cross-over could provide improved reliability coupled with minimal routine maintenance based on electrically driven, light-weight materials of high-energy density.⁶⁹ It is worth mentioning that several ternary or quaternary additions of elements are necessary depending on the application where for example V is added to FeCo (1-2%) to add mechanical hardness.² Nanomaterials of FeCo alloys of varied atomic ratios have been reported by multiple synthetic techniques including urea-assisted sol-gel routes to mechanical alloying (MA) by high energy ball milling.⁷⁰⁻⁷²

Furthermore, self-assembled (without human intervention) magnetic nanomaterials are of particular interest when their ordering creates novel morphologies that enhance any property of the material as in the case of self-assembled FeCo nanospheres for biomacromolecule loading where self-assembly of FeCo NCs (nanoclusters) by a polypeptide enhanced the overall response to a magnetic field.⁷³ Another report of self-assembled FeCo nanospheres by Al₂O₃ coated FeCo nanocapsules by the arc-discharge method reported enhanced EM (electromagnetic) wave absorption due in part to the shape anisotropy of the structure. In another recent finding, magnetite particles aligned within a polymer matrix by a magnetic field following removal of solvent possessed an induced magnetic anisotropy throughout the entire polymer garnering applicability for incorporation into what the authors referred to as soft-robot technology.⁷⁴ The parallel orientations of the magnetite particles have a higher permeability than those at perpendicular orientation providing selective actuation thru manipulation of an external field.

The aim of the work in this chapter is to identify the significant factors that control self-assembly of FeCo chains synthesized by a Ag-seed mediated polyol process as well as comprehensive investigation of factors that determine the physical properties of the chain, namely diameter (nm) and crystallite size (nm). A design of experiment (DOE) was performed taking into account all main effects and interactions between experimental factors.

DOEs are useful for investigation of global maxima or minima of product yield or material properties whether magnetic, structural or electronic. If the DOE is appropriate, the results may help in formulating sound predictions on the response (dependent variable) such as the minimization of the coercivity, or the maximization of magnetic saturation. Performing a DOE takes into account all interactions among factors as mentioned previously; this can reveal hidden hot spots in responses where the one variable at a time approaches (OVAT) fails to do so.⁷⁵ While

mandatorily used for commercial interest, fewer approaches exist in scientific literature using statistical methods for analysis of wet-chemical syntheses of inorganic materials, especially magnetic nanomaterials. This is apparently due to a combination of high cost, time, effort and lack of environmental control required to perform multiple syntheses.

In this work, a custom design DOE was created using JMP (SAS) statistical software since it minimized experimental trials. Controlled independent variables used were [OH], total reaction time (mins.), Fe:Co molar ratio, total [Metal] and [Ag] seed and stir rate (sec/stir cycle).

The DOE performed in this work was a custom design generated by using JMP (SAS) software for the purpose of generating response surface models (RSMs) of factors that are significant for controlling the properties mentioned previously. A representation of a typical reaction vessel used in this work is shown below in Scheme 1 where a Teflon vessel coupled with a temperature control probe, heating jacket, magnetic stir bar, nitrogen and a moisture absorbent are represented.

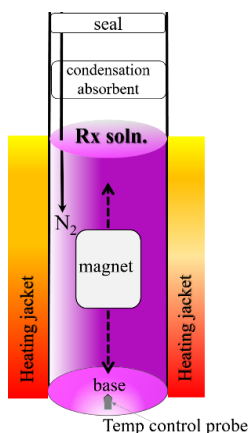


Figure 5.1 A representation of a vessel from the Surveyor Argonaut Process Synthesizer: a suitable tool for combinatorial chemistry studies as well as DOEs.

5.3 Experimental

Initially, Ag, Pt and Ru were experimented with and used as nucleating agents to control size. Their usage as nucleation agents has been reported in various wet-chemical techniques including the polyol process.^{25,33} General trials of metal to seed ratios were performed of Ag, Pt and Ru and SEMs are shown below in figure 5.2.

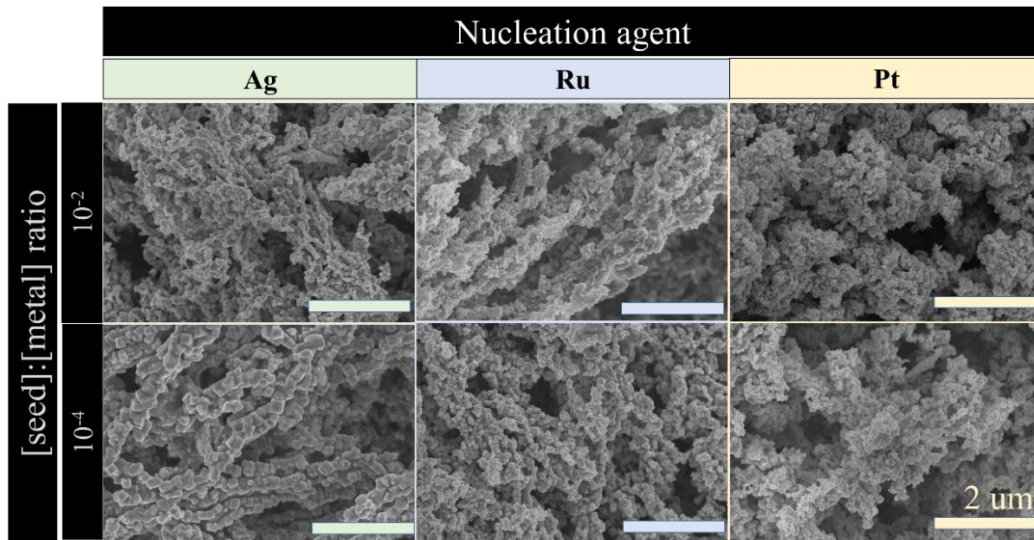


Figure 5.2: Various nucleation agents of Ag, Ru and Pt at low (10^{-4}) and high (10^{-2}) [Seed]/[Metal] ratios and their effect on FeCo morphologies taken by SEM.

The Pt and Ru nucleation agents proved too difficult to control the FeCo particles as shown by the SEM in figure 5.2. The Pt and Ru along with other noble metals reduce more easily in practice than Ag which has been shown in previous reports of ethylene glycol reduction of Pt.^{30,76,77} For this reason, Ag was chosen as the nucleation agent in this work as the particle size could be more easily tailorable; in the SEM of the low concentration (10^{-4}) of Ag from figure 5.2, SEM, the particle sizes were largest around 150-200 nm as compared with the other nucleation agents.

5.3.1 Characterization

X-ray diffraction was performed on a Panalytical X'Pert Pro diffractometer equipped with a Pixcel detector in a θ - 2θ configuration. All samples synthesized in the DOE were done so from a scan range of $20 - 85 2\theta$ to account for all phases which included Co (fcc), cobalt ferrite and FeCo alloy. Each sample was leveled into a depression on a low background Si wafer prior to mounting into the XRD. The X-ray source used was Cu K_{α} with $\lambda=1.54 \text{ \AA}$. Scherrer analysis was performed where the formula is given in chapter 2. The protocol for determining the average crystallite size is given below in figure 5.3

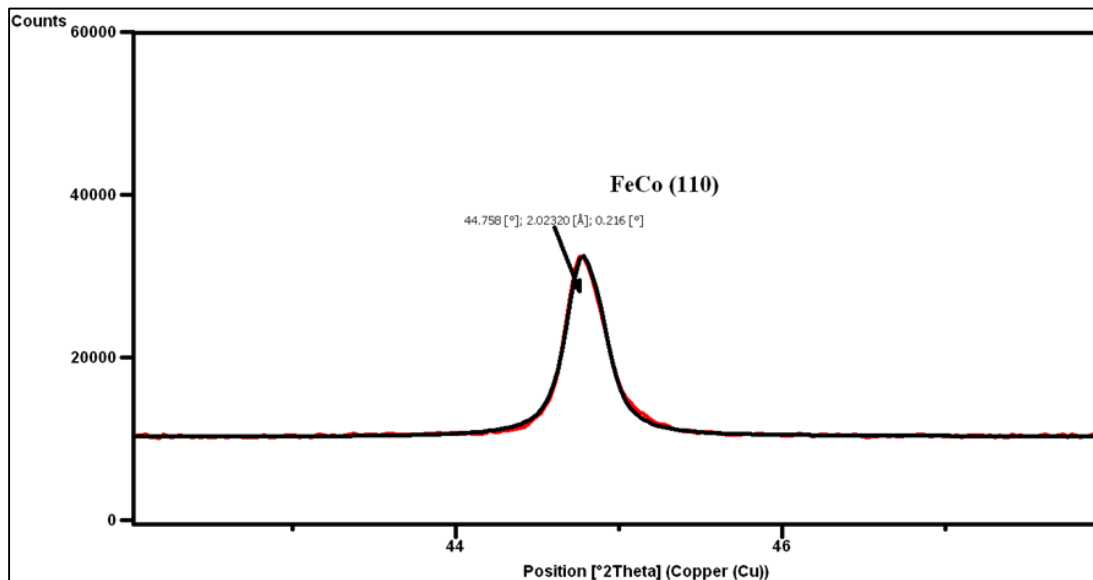


Figure 5.3. A representation of the (110) plane of FeCo alloy by XRD with profile fitting showing the FWHM value determined using HighScorePlus ® software. These peak analyses were used for the average crystallite size determination.

TEM was done to investigate the morphology and microstructure of the various morphologies synthesized in this work. The TEM was operated at 120 keV and was a Zeiss Libra 120. Each sample imaged was prepared by the drop-cast method where a dilute suspension of powder sample was added by pipette dropwise three times with 15 minutes drying intervals. The TEM

grids used were Lacey (formvar coated) grid with 300 mesh Cu support. SAED was performed to confirm phase identification as well as cone-illumination to reflect crystallinities at a particular Bragg reflection. This was done to highlight microstructure and the crystallinity of the sample by DFTEM.

Morphology study of the surface was performed using SEM on a Hitachi SU-70 FE-SEM operated at 5 keV in field free mode. Each powder sample was adhered to an aluminum substrate using carbon paste with MEK as a solvent. The paste was allowed to dry for at least 30 minutes and a rare earth magnet was used to remove stray magnetic particles.

Magnetic characterization of all samples was performed using a vibrating sample magnetometer (Quantum Design Versalab). M-H curves were generated in a sweeping field from 3 to -3T. All samples were prepared in a consistent manner. First the dried powders were massed into polypropylene capsules and centered onto a brass sample holder having low magnetic signature (10^{-6} emu). The sample holder was threaded onto a sample rod and inserted into the VSM chamber following multiple purge cycles to achieve partial vacuum down to 10 Torr.

5.4 Results and Discussion

Phase identification by XRD was performed on every as-synthesized sample. All indicated at least some formation of the FeCo bcc phase while 90% of the samples possessed 100 % FeCo composition (note: FeCo alloy will refer to the 100 % composition for the remainder of chapter 5 unless noted). XRD scans representative of the pure phase FeCo is given in figure 5.4(a) as well as a representative composite of cobalt ferrite (CFO) and FeCo in (b). The pdf: 01-071-5029 matches the FeCo bcc major peak shown around 45, 65 and 83 $2\theta^\circ$ respectively by the asterisk symbol in figure 5.4 (a) and (b).

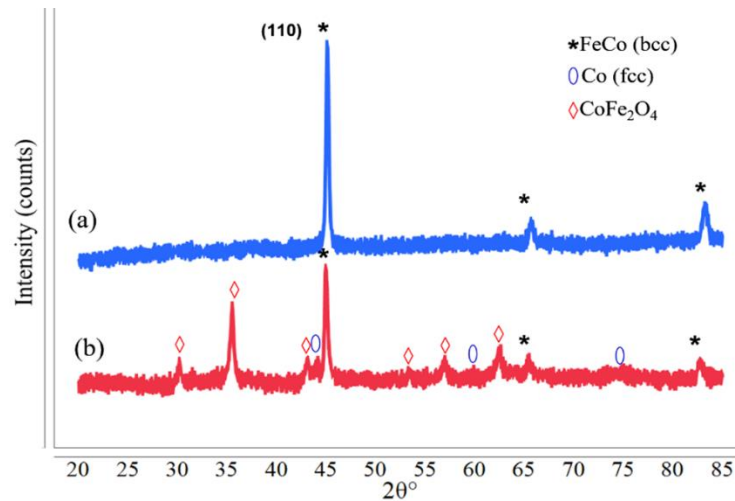


Figure 5.4. XRDs showing 100 % FeCo (a) and combination of FeCo, Co (fcc) and CoFe₂O₄ (CFO) (b). These phases represent those synthesized throughout the DOE.

All as-synthesized samples were probed for morphology variation and classified using SEM. Several morphologies were found under the experimental design space and are shown in figure 5.5 where (a) and (b) are nanochains (< 100 nm mean diameter), (c) Ag-seeded chains, (d) non-Ag seeded chains, (e) chains + ellipsoidal particles of Co, (f) carbon-coated chains, (g) CFO spheres and (h) particles. The spheres in figure 5.5 (g) were the only morphology with a partial cobalt ferrite composition.

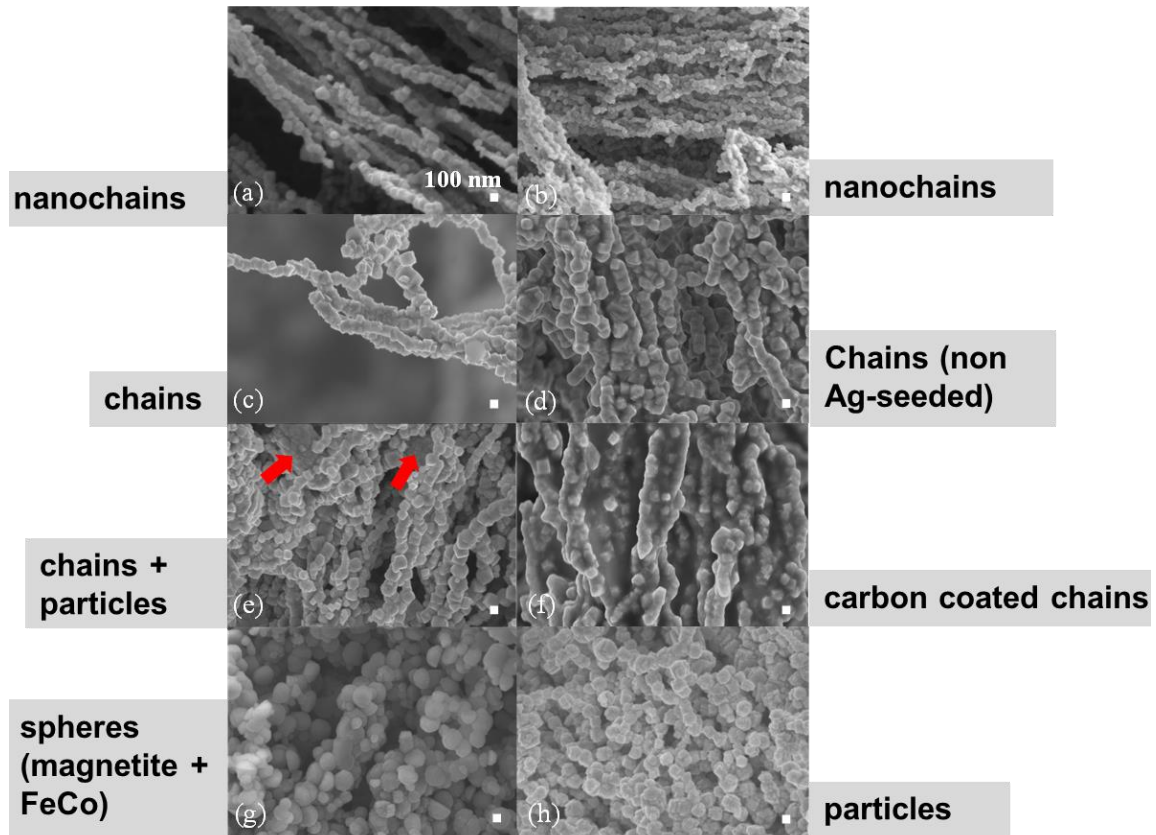


Figure 5.5. Representative morphologies synthesized throughout the DOE with nanochains (less than 100 nm) shown in (a) and (b), Ag-seeded chains in (c), larger diameter, non-seeded chains in (d), chains and particle (red arrows/ellipsoidal stellated structures) (Co) mixtures in (e), C-coated chains in (f), spheres (CoFe₂O₄) in (g) and particles in (h). All morphologies are 100 % FeCo unless secondary phase is noted.

For all pure FeCo samples, chains (Ag-seeded) were most prevalent at 45% followed by nanochains (13 %) with all others at 11 % shown in figure 5.6 below.

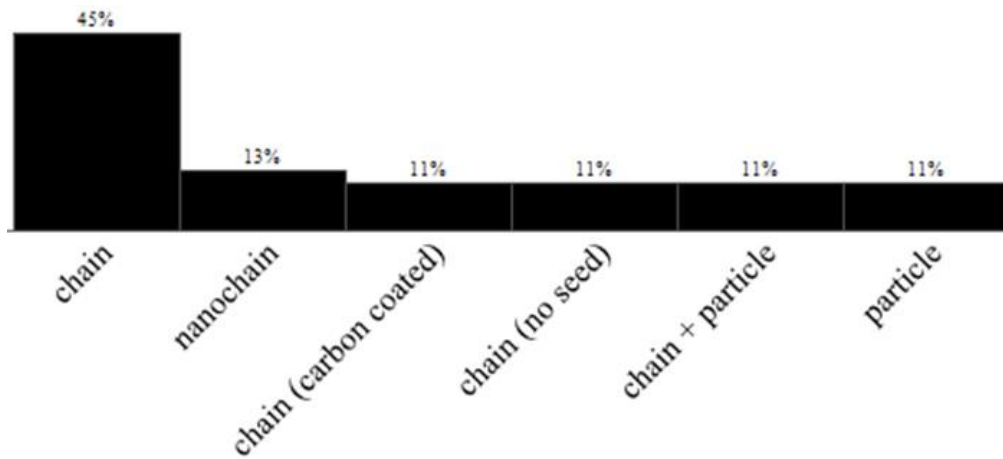


Figure 5.6. Chart showing relative abundances of morphologies observed in the DOE study for pure phase FeCo bcc.

SEM images of the nanochains shown in figure 5.5 (a) and (b) have mean diameters (D_m) of 99 and 75 nm respectively and represent the largest and smallest diameters for all nanochains synthesized. The nanochains overall had $D_m = 80$ nm. D_m for the chains in figure 5.5 (c) was 130 nm while chains synthesized using no Ag seed had $D_m = 173$ nm shown in (d).

Figure 5.7 below contains TEM micrographs taken for the FeCo nanochains (b-d, f, g) as well as Ag-seeded chains (a, e) with SADP taken of nanochains further confirming the FeCo (110) phase in (h). From the inset in (h) of figure 5.7, nanochains are shown by DFTEM having multiple crystallites making up the internal chain structure. This is in opposition to the one-by-one particle morphology commonly observed in FeCo MALC in chapter 4 as well as the other nanochains observed in (b, c, f and g) from figure 5.7 in this work. This could be explained in part by the Co-rich composition which promotes smaller crystallite sizes (by Scherrer analysis, see Table 5.2 for correlation probabilities and discussion below).

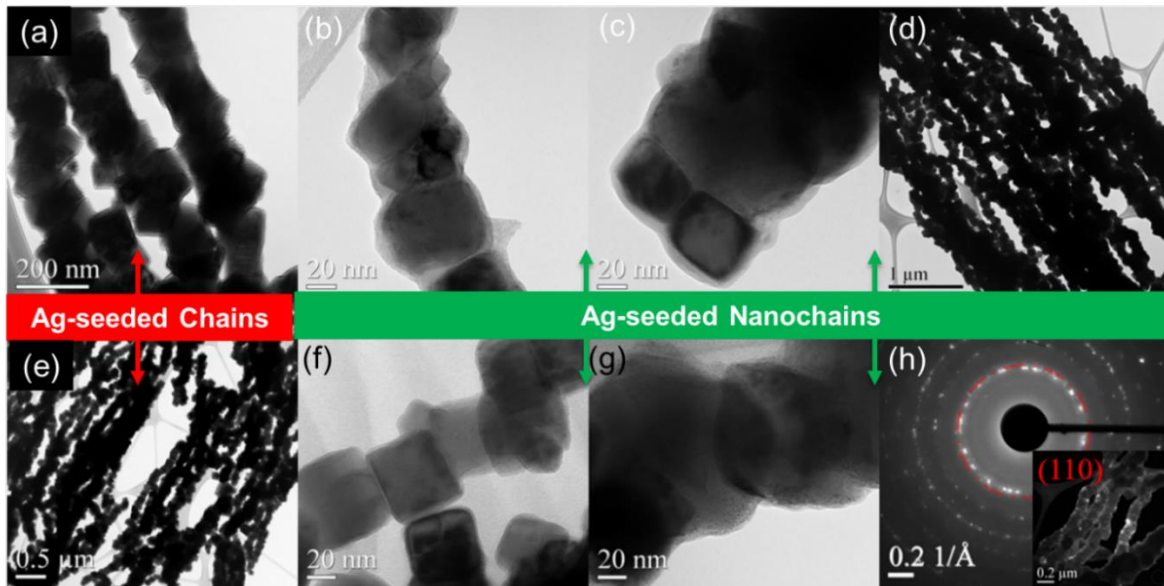


Figure 5.7. TEM images of Ag-seeded FeCo chains in (a) and (e) and Ag-seeded nanochains in (b-d) and (f) and (g) with SAED indicating FeCo bcc alloy and (110) crystallites illuminated using dark-field cone-illumination in inset of (h).

Table 5.1 below, provides the effect summaries for all response surface models generated indicating the significance by p-values assessment of all independent variables. All independent controlled variables are shown as having significant p-values (with the exception of only partial significance ($0.05 < p\text{-value} < 0.1$) of the Fe:Co (2^{nd} order-crossed) and (3^{rd} order-crossed) in the chain formation and crystallite size respectively. These are p-values are shown in the effect summaries given in table 5.1.

Table 5.1. Effect summaries for all responses in the RSMs shown in Figure 5.8 with p-values given for each variable (source) or transformation with other variables.

FeCo % Composition Source	LogWorth		PValue
[OH]/[Metal]*[OH]/[Metal]	4.851		0.00001
Fe:Co molar ratio*[OH]/[Metal]	2.265		0.00544
[OH]/[Metal]	1.985		0.01035
Fe:Co molar ratio	1.732		0.01853
Fe:Co molar ratio*Fe:Co molar ratio	1.568		0.02706
Chain Formation Rating Source	LogWorth		PValue
[OH]/[Metal]	1.974		0.01063
[OH]/[Metal]*Rx time (mins)	1.904		0.01248
Fe:Co molar ratio	1.423		0.03779
Fe:Co molar ratio*Fe:Co molar ratio	1.030		0.09336
Crystallite Size (nm) Source	LogWorth		PValue
Fe:Co molar ratio	4.705		0.00002
Fe:Co molar ratio*[Ag]/[Metal]	1.975		0.01060
Fe:Co molar ratio*Fe:Co molar ratio*Fe:Co molar ratio	1.176		0.06666

XRD was performed on all samples to investigate the percent phase composition of FeCo alloy (bcc). A response surface model (RSM) was generated for FeCo alloy % as a response, presented in figure 5.8 (a), where p-values were shown to be significant of [OH]/[Metal] and Fe:Co (molar ratio) as well as their interaction shown in Table 5.1. For high [OH]/[Metal] ratios above 30, the FeCo alloy formation may be predicted within the Fe:Co design space (0.5-2.5). In contrast, for lower [OH]/[Metal] values, several phases are predicted where oxides and Co (fcc) may form at high Fe:Co ratios and Co (fcc) with FeCo alloy for lower Fe:Co ratios. Increasing the [OH]/[Metal] > 60 becomes problematic as the magnetic stirring can bind. In addition, polymerization of the ethylene glycol may occur if [OH] is not kept ≤ 7 M.⁷⁸

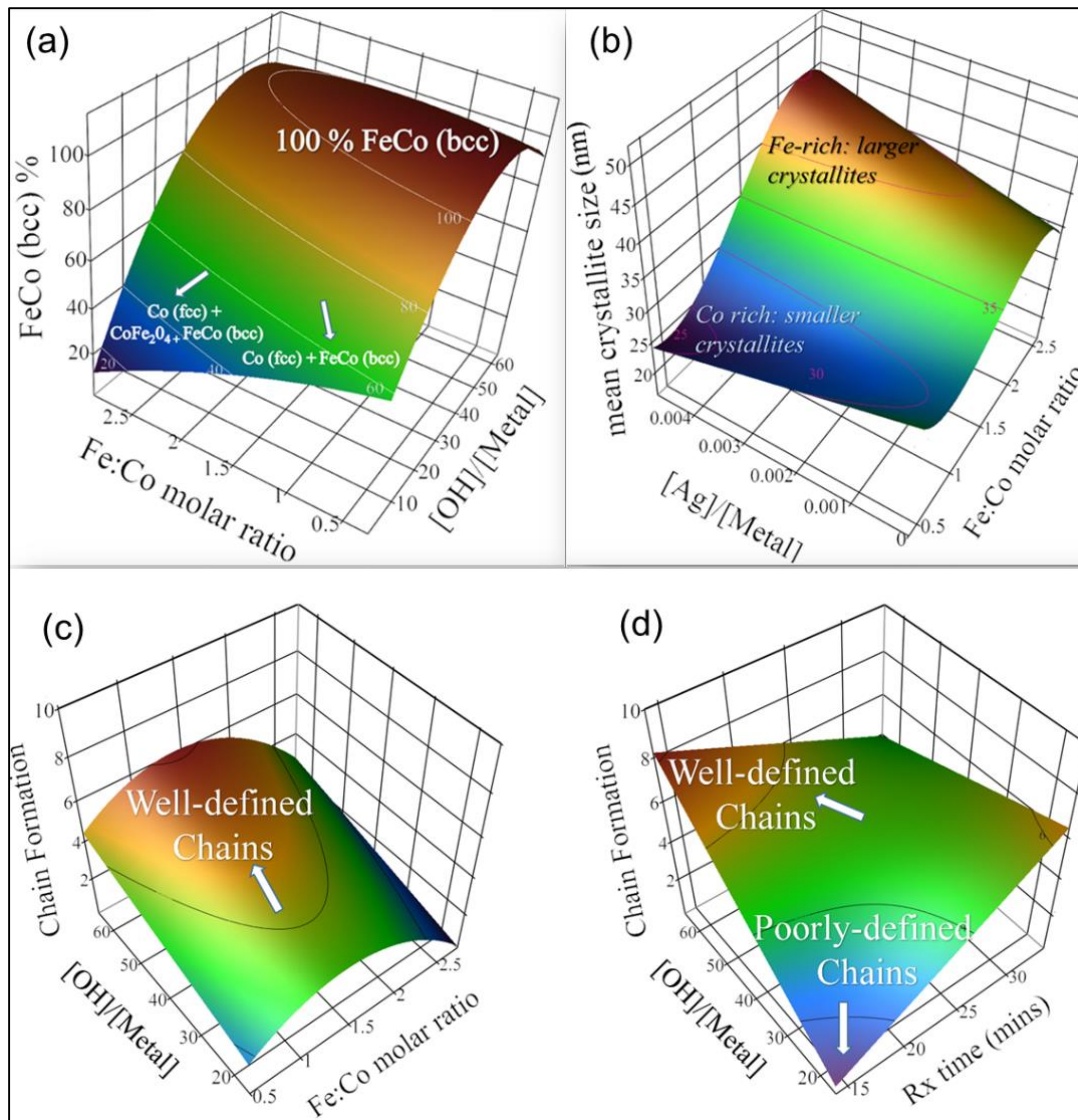


Figure 5.8. Response surface models for % FeCo alloy composition (by XRD) in (a), mean crystallite size (by Scherrer) in (b) and chain formation quality (by SEM) in (c) and (d) all constructed using most significant p-values of independent variables or transformations between two significant variables.

FeCo (bcc) alloy samples were morphologically assessed based on evidence by SEM of self-assembled high aspect ratio structure formation otherwise generally referred to as linear chains. Chains, chains (no Ag seed), chains + particles, particles, nanochains, and carbon coated chains were included in this study. Multiple SEM images at similar magnifications were gathered and an assessment of chain formation was determined, rated and transformed into a response (chain

formation) with increasing values representing well-defined chain morphologies. Figure 5.8 (c and d) contains two RSMs representing interactions between three significant factors (see p-values in Table 5.1) against chain formation as a response which are (a) Fe:Co molar ratio with $[OH]/[Metal]$ and (b) total reaction time (mins) with $[OH]/[Metal]$. Chain formation value at 10 (represented by SEM, Figure 5.5 (a)) represents a well-defined linear chain formation while a value of 0 represents an absence of chain morphology with in intermediate values assessed on relative chain presence in each sample versus other morphologies, as well as aspect ratio and linearity. It is important to note that a strong correlation between the chain formation values and M_s (emu/g) ($p=0.0237$, see Table 5.1) indicate that the chain formation assessment method used is meaningful since linear chain morphologies (includes chains, chains (non Ag-seeded), chains (carbon coated) on average possess the highest M_s .

Fe:Co molar ratios around 1.5 with increased $[OH]/[Metal]$ ratios as seen in figure 5.8 (c) indicate well-defined chain formation explained by these alloys having molar ratios near the Slater-Pauling limit (highest theoretical moment: 65 % Fe and 35 % Co).^{2,14} These alloy compositions promote unimpeded self-assembly into chains since the particles typically contain M_s well above 170 (emu/g). Low reaction times at 16 minutes with high $[OH]/[Metal]$ in figure 5.8 (d) indicate well-defined chains where low $[OH]/[Metal]$ result in poorly-defined chain formation to total absence of chains.

Several factors were explored in determining the mean crystallite size (nm) as a response since it is very strongly correlated with saturation magnetization (emu/g) (see Table 5.2 below). It was found that the $[Ag]/[Metal]$ ratio when interacted with various Fe:Co molar ratios are both significant independent variables and meaningful in controlling the mean crystallite size (nm) allowing for indirect control of M_s (emu/g). Intriguingly, it was found that in Fe-rich FeCo alloys,

an increase in $[Ag]/[Metal]$ generates larger crystallite sizes (nm) while in sharp contrast, Co-rich produced smaller crystallites represented by the RSM in figure 5.8 (b). The routine for determination of mean crystallite size was discussed previously in this chapter.

The mean diameter of the FeCo alloy morphologies were measured and determined from SEM images and plotted in a meaningful representation in figure 5.9 (upper plot). It was determined that the lowest mean diameter just above 100 nm was obtained when the $[Ag]/[Co]$ molar ratio (in the Fe:Co molar ratio design space, 0.5 -2.5) was kept between 6.3×10^{-5} and 5.9×10^{-4} demonstrating diameter control of all morphologies where a mean diameter ≈ 170 nm of chain (no Ag seed)

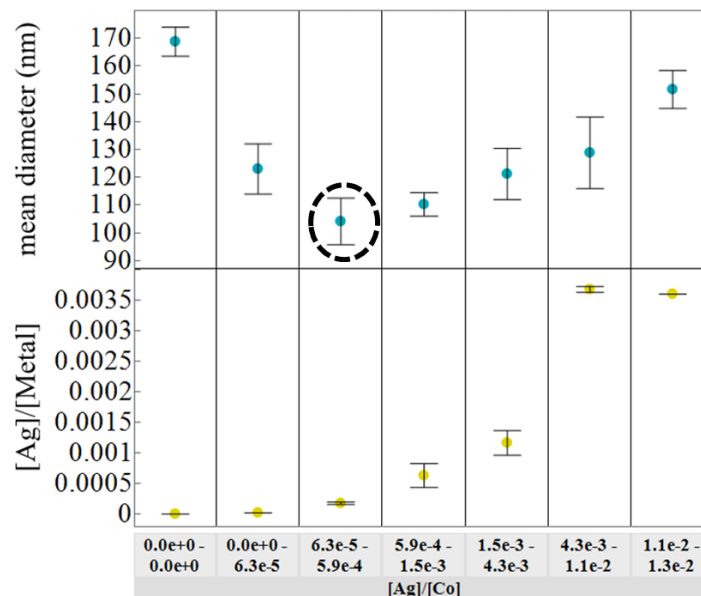


Figure 5.9. $[Ag]/[Co]$ vs. mean chain diameter (nm) (upper plot) for all FeCo alloy morphologies with corresponding $[Ag]/[Metal]$ averages (lower plot) with std. error bars shown.

representing the highest value. This finding is significant for this work since coercivity (H_c) correlates strongly with mean diameter (nm) (p -value < 0.0001) (see Table 5.2) indicating another example of indirect control. From figure 5.9 (lower plot), the mean $[Ag]/[Metal]$ ratio is given

corresponding to the [Ag]/[Co] ranges showing [Ag]/[Metal] is optimal for decreased diameters below $5e^{-4}$. (see Table 5.1 for p-values).

Saturation magnetization (emu/g) and coercivity (Oe) values were obtained for all morphologies by VSM and the hysteresis curves are shown in figure 5.10 with legend ordered by increasing to decreasing saturation values corresponding to each curve. While spheres (●) possess the lowest saturation due to oxide formation, Ag seeded chains (△) and unseeded chains (▲) share similar M_s values indicating that the presence of Ag in small concentrations does not impact the overall

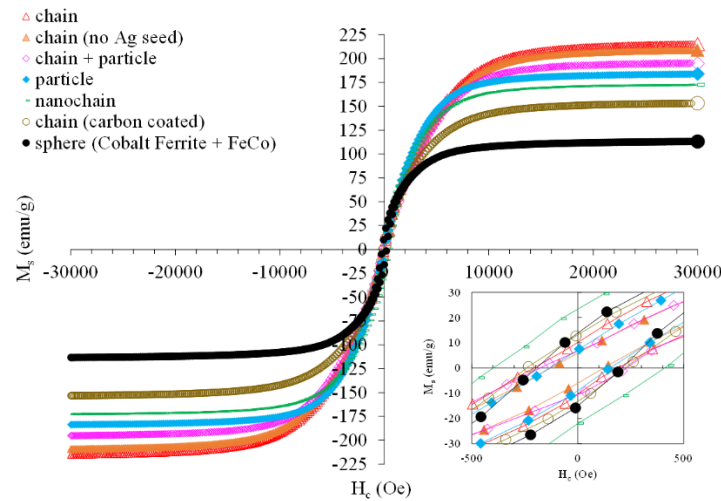


Figure 5.10. Various morphologies with representative M-H curves showing saturation magnetization values shown with chain (△), chain (no Ag seed), (▲), chain + particle (◇), particle (◆), nanochain (□), chain (carbon coated) (○) and sphere (●).

moment. The presence of carbon in the coated chains (○) was confirmed by EDS, (results not shown). This material on average possessed the second lowest M_s value just above 150 emu/g since it acts as a non-magnetic mass. Intriguingly, nanochains (□) in figure 5.10 possess the highest value of H_c at 400 Oe and $M_s \approx 175$ emu/g with no detectable presence of Ag by EDS (not shown).

TGA-IR plots were acquired to further confirm carbon presence on the carbon-coated chains shown in figure 5.11 below. Plot (a) is of the TGA-FTIR analysis of the carbon coated chains and indicates CO₂ evolution, (up to 7 % mass loss) an indication of carbon presence on the surface. Plot (b) indicates similar evolution of CO₂ (only 2 % mass loss) (band near 2300 cm⁻¹) (2, 3-butadione) formation 200-250 C in both plots but (b) losses only 25 % of the mass of the carbon coated chains in (a). It has been reported that 2, 3 butadione is formed onto particle surfaces as an oxidation product of ethylene glycol reductions and is acts to keep nanoparticles from agglomerating due to the electron pairs.²²

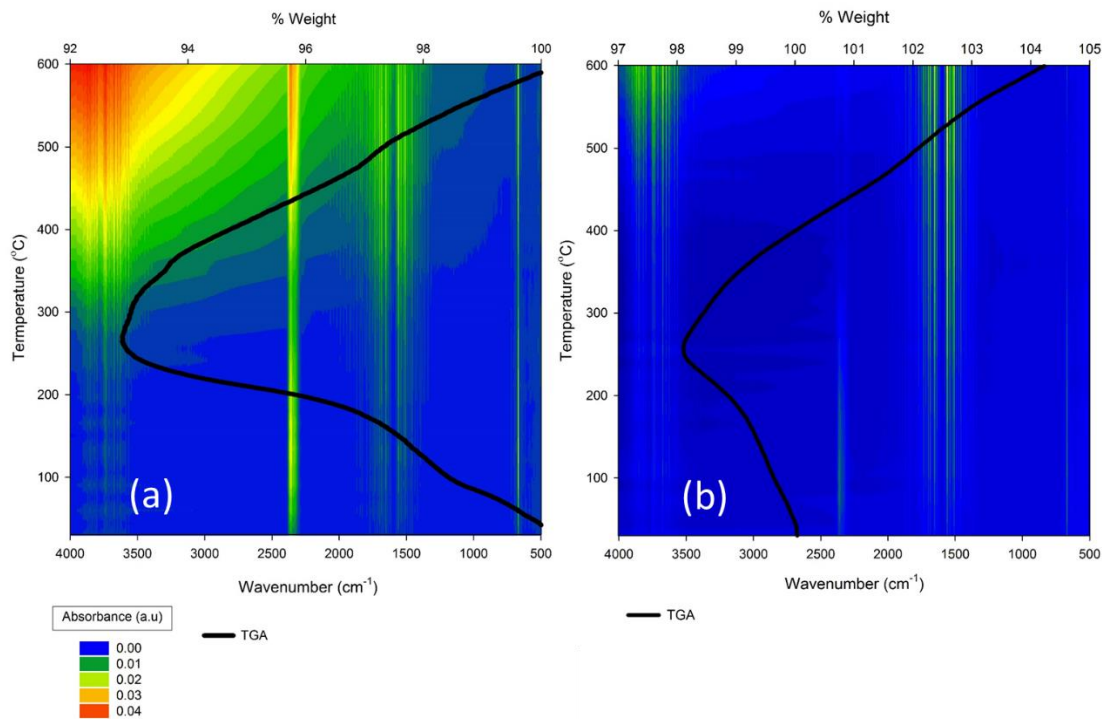


Figure 5.11. Thermogravimetric analysis (black curve) coupled to FTIR absorbance spectra (TGA-FTIR) of carbon-coated chain sample in (a) and nanochain sample in (b) showing the difference in carbon content by mass loss.

Elliptical plots representing 90 % coverage of all data points against their physical (mean diameter, crystallite size and their ratio (y-axes)) and magnetic properties (x-axes) and H_c (Oe),

M_s (emu/g) were plotted for every FeCo alloy morphology shown in figure 5.12. Ag seeded nanochains possessed H_c as high as 400 Oe while chains possessed the highest M_s values > 210 emu/g. Significant correlations exist between H_c and diameter as well as M_s and crystallite size for all morphologies shown in table 5.2. Variation of M_s (emu/g) in the carbon coated chains is attributed to varying amounts of carbon on the surface.

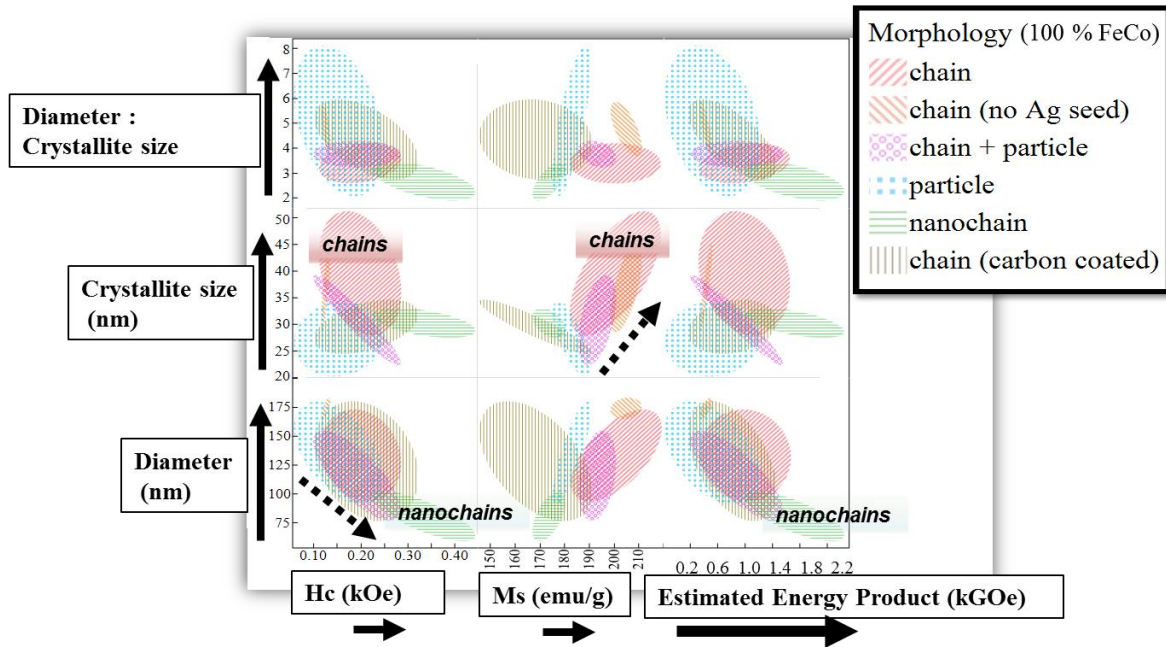


Figure 5.12. Elliptical plots (90 % coverage) for FeCo alloy morphologies against physical (mean diameter (nm) and crystallite size (nm) and ratio) and magnetic properties of (H_c (Oe) and M_s (emu/g)).

Correlation probabilities are given below in table 5.2 of all responses measure throughout this entire study.

Table 5.2: Correlation probabilities (p-values) for all analyzed responses in the DOE.

Responses	H_c (kOe)	M_s (emu/g)	diameter (nm)	crystallite size (nm)	chain rating
H_c (kOe)	<.0001	0.0012	<.0001	0.1704	0.6127
M_s (emu/g)	0.0012	<.0001	0.0003	<.0001	0.0237
mean diameter (nm)	<.0001	0.0003	<.0001	0.0054	0.9419
mean crystallite size (nm)	0.1704	<.0001	0.0054	<.0001	0.0125
chain rating	0.6127	0.0237	0.9419	0.0125	<.0001

To monitor the FeCo composition variation over the course of a typical reaction, aliquots were cautiously removed from the live reaction at various time intervals. This was performed on a 50:50 Fe:Co molar ratio preparation, using 3.5 M OH, 0.1 M [Metal] and no addition of [Ag] seed. Any captured magnetic particles were magnetically separated from the aliquots. The aliquots were diluted using Class A volumetric glassware analytically and were dissolved into aqua-regia media (NMT 5 % acid) and were prepared for inductively coupled plasma-optical emission spectroscopy (ICP-OES). ICP-OES was used to probe for relative variation of the reaction media in Co:Fe concentrations. Any change in the two would give indication on the relative reduction rates of the two metal precursors. Figure 5.13 below, represents the normalized (nominal concentration of Fe and Co, 50:50 atomic) molar ratio of Co:Fe on the y-axis against the reaction times in minutes. An observed decrease in Co concentration relative to Fe in the reaction solution is shown by the data points. This suggests that the Co nuclei are forming before Fe nuclei by evidence of the Co depletion over the Fe depletion in the reaction solution over time. The

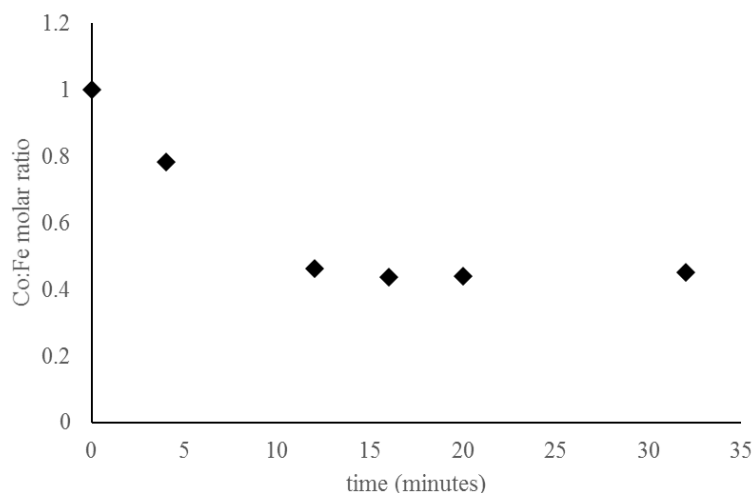


Figure 5.13: ICP results (normalized to nominal Co and Fe concentrations (50:50 molar) of reaction solution aliquots sampled at various time points during the reaction process.

This indicates that Co nuclei are the first to form in the reaction which correlates with the lower reduction potential of Co versus Fe. Studies in the polyol synthesis of Ag nanoparticles using ethylene glycol as a solvent have showed that glycolaldehyde forms in the presence of oxygen. It is

expected that some level of oxygen is present in the reaction performed in this DOE as the sealed PTFE reaction system has obvious limitations in creating a perfectly air-free environment.

Furthermore, the study performed on the mechanism indicates that ethylene glycol oxidation to glycolaldehyde increase exponentially above 150 C to 160 C. This finding substantiates why the temperature is to be maintained at 150 C in of the FeCo HTE work presented in this dissertation.

5.4.1 Mechanism for the Assembly of FeCo Chains

The prevalence of linear chains, which possessed three diameter ranges in order of increasing diameter: nanochains, chains and non-seeded chains, have been explained by the presence of an external magnetic field.⁷⁹ These structures first form by the field magnetic flux lines aligning the high moment FeCo nuclei locking them into linear arrangements. As the magnetically-linked nuclei continue to grow into particles, their interfaces become embedded into one another creating a continuous structure indicated by TEM in previous work.⁷⁹ This similar mechanism occurs for the entire range of Fe:Co molar ratios where chains containing higher moment Fe-rich particles are characterized by their well-defined cubic facets (≈ 1.5 Fe:Co molar ratio). The cubic particles forming the chains appear as to stem from one another out of plane from the (100) face indicating discontinuity of the bcc lattice, from TEM in figure 5.7 (c). Further, Scherrer analyses indicated a polycrystalline nature since most mean diameter to crystallite ratios were well above 2 in all samples, figure 5.12 (upper left). It is important to note that these cubic particles are often observed linked either through the space diagonal of the cube (corner to corner), face diagonal (edge to edge), or corner to edge before growing into one another. This phenomenon could be explained by the fact that when polarization occurs, the relative change in magnetic flux density are greatest at corners and edges of materials, hence, inter-particle attraction is stronger in these regions. Surprisingly, most chains do not appear to form through the easy-axis of

magnetization $\langle 100 \rangle$ indicating that nuclei first form and grow into one another since the easy axis of magnetization has a minimal effect on interparticle growth formation at very small particle volumes.

5.4.2 Reaction Parameters and Responses

The DOE performed in this work is centered on six independent variables (factors) namely Fe:Co molar ratio, [OH], [Metal], stir rate (sec/cycle), total reaction time (mins.), and [Ag] resulting in several morphologies categorized primarily by diameter and shape. Independent variables were identified for significantly controlling FeCo phase formation, chain formation assessment and their physical properties of mean crystallite size and diameter (nm) through statistical analysis. While some variables alone were significant for some responses, their transformations with other variables, as in the case of [Ag]/[Metal] or [OH]/[Metal], were found to have stronger interactions thus generating more meaningful models. Most responses analyzed strongly cross-correlate supporting the methods of analysis performed (see supplemental, Reactions Parameter Notes).

5.4.3 Control of Fe₁Co_{1-x} Phase

For control of alloy phase %, the larger values of [OH]/[Metal] ratios shown in figure 5.8 (a) were optimal (RSM) since with increased hydroxide, the strength of the ethylene glycol solvent as a reducing agent is increased as to overcome the activation energy required to form the alloy.⁸⁰ In addition, the RSM in figure 5.8 (a) predicts that for Co-rich samples synthesized with < 30 [OH]/[Metal], Co (fcc) and FeCo composites form while for Fe-rich, addition of cobalt ferrite (CoFe₂O₄) is expected. These observations may be explained by the lower reduction potential of Fe (-0.44 V) where Co (fcc) formation is favored.²²

5.4.4 Control of Fe₁Co_{1-x} Chain Morphology

An advantage of the self-assembly of FeCo chains in the work is an observed increase in the saturation magnetization values over single particle morphologies of FeCo. This enhancement is due to the entire linear chain acting as a single high aspect ratio nanomagnet of which the internal magnetic field lines may pass through the poles minimizing stray flux.⁸¹⁻⁸³ RSMs representing assessed chain formation in figure 5.8 (c and d) were created using [OH]/[Metal] with Fe:Co molar ratio (a) and reaction time (mins) (b) where well-defined chain formation is promoted ≈ 1.5 Fe:Co molar ratio and high [OH]/[Metal], while shortest reaction times at 16 mins and high [OH]/[Metal] produced well-defined chains. The Slater-Pauling limit composition has an Fe:Co molar ratio is ≈ 1.85 , (for theoretical max. moment), near 1.5, supporting the model in figure 5.8 (c) because particle self-assembly into chains is driven primarily by the average moment per particle in an external field. Figure 5.8 (d) indicates well-defined chains form sooner in reaction conditions with high 40-60 [OH]/[Metal] which drives FeCo alloy formation over ferrites and Co⁰ (fcc). Chains are likely susceptible to fragmentation and oxidation at increased reaction times up to 32 minutes and high [OH]/[Metal], while lower [OH]/[Metal] and high reaction times (32 mins) promote enhanced chain formation. Lowest reaction times ≈ 16 minutes and low [OH]/[Metal] restrict 100 % FeCo formation resulting in mixed morphologies and minimal chain formation.

5.4.5 Control of Fe₁Co_{1-x} Crystallite Size

From figure 5.8 (b), there is a significant reduction in crystallite size for Co-rich samples for large [Ag]/[Metal] while Fe-rich samples show a significant marked increase. This finding is may be attributed to the lower reduction potential (-0.28 V) of Co than Fe (-0.44 V) compounded with the presence of Ag nucleation agents.²² This could lower the activation energy (E_a) for Co crystallite formation. In another report, Cu was used as a nucleating agent and was shown to

reduce E_a for FeCo alloy crystallization events.¹⁴ This similar phenomenon is expected for Ag as a nucleating agent generating Co crystallites thru which controlling the total number of nucleation sites, or [Ag], the population of crystallites are regulated. For the Fe-rich alloys (Fe:Co > 1), Co are first to form nuclei and grow into clusters before co-precipitating with Fe. This results in decreased availability of [Co] for formation into the bcc FeCo lattice during later stages of particle growth. As a result, relatively fewer defects within each particle are incorporated as compared with Co-rich compositions. This generates an overall improved magnetic ordering of the bcc lattice resulting in increased crystallite volumes higher moments since the spin dilution effect is reduced.

5.4.6 Correlations of the Physical and Magnetic Properties

[Ag]/[Co] around $1e^{-4}$ provided the lowest mean diameters and this trend substantiates the preferential nucleation of Co over Fe as seen from figure 5.9 (top plot). Coercivity is increased in smaller grain sizes allowing for domain wall pinning to occur. In the case of linear chains, the average grain size may be approximated as the chain diameter where the smallest diameter structures possess the highest values as shown in the nanochains (figure 5.12, bottom left).⁶ Another meaningful correlation is the mean crystallite size (nm) with M_s (emu/g) (p-value < 0.0001, see supplemental, Table S1). The largest crystallite sizes lead to fewer domain wall interfaces, therefore less magnetostriction in for similar particle volumes.⁶ Physical limitations on the synthesis of self-assembled FeCo chains are expected for particle sizes well below 100 nm. This may be caused by spin dilution and decreased crystallite size throughout the FeCo particle segments thus negatively impacting magnetic susceptibility within the external field. Altogether, these findings indicate indirect control of magnetic properties by directly controlling

the physical properties of crystallite sizes and diameters both achieved through Ag seed mediation.

5.5 Conclusion

In this work, demonstration of control of the physical properties of unique self-assembled FeCo chains was performed. These findings can be used to tailor the magnetic properties within the theoretical limitations of FeCo alloy using statistical analysis to support these claims. Applications for the self-assembled Ag-seeded FeCo linear chains as well as the various FeCo morphologies observed are expected to be numerous and varied from enhanced selective actuation for soft-robot technology to EM absorbing materials or improved solenoid devices since the magnetic properties of H_c and M_s are tunable.

An understanding and demonstration of FeCo alloy magnetic property correlation and crystallite size control was achieved by judicious tailoring of Ag seed to metal ratios dependent on alloy composition while compositionally independent Ag seed to Co molar ratios were found for minimizing the chain diameter all performed by a DOE. Future work will employ other noble metal nucleating agents such as Pt and Rh to achieve even smaller grain sizes.

Alternatively, increasing permeability and decreasing coercivity of wet-chemically synthesized FeCo alloys will be explored through seed-mediation and ternary alloy inclusion for usage in magnetic cores in transformers where nanocomposites of ferrite and Fe-based alloys are currently being explored for this purpose.¹¹ By using the polyol process method, response surface models were constructed based on the synthesis factors to produce pure phase FeCo alloys with different morphologies, size ranges and aspect ratios and ultimately magnetic responses.

Chapter 6. Synthesis of High Aspect Ratio Cobalt Ferrite Nanostructured Pillars

6.1 Overview

This work was motivated by the desire to synthesize high aspect ratio structure from the cobalt ferrite phase a well-known magnetic material after having had success synthesizing high aspect ratio FeCo chains. This presented a challenge as cobalt ferrite has inherently lower moment and is thus harder to magnetize and grow into linear chains as performed in chapter 4.

6.2 Introduction

Cobalt ferrite (CoFe_2O_4), nanomaterials have been of interest in recent years due to their catalytic oxidation properties, magnetic recording devices and usage in ferrofluids.^{53,84,85} They are also crucial for data storage technology and potential magnetic carriers for drug delivery.⁸⁶⁻⁸⁸ The spinel structure for ferrites is given by $M\text{Fe}_2\text{O}_4$ (M =Late Transition metal). Cobalt ferrite in particular has an inverse spinel structure where Co^{2+} occupy octahedral sites and Fe^{3+} are in tetrahedral and octahedral sites. CoFe_2O_4 has an anisotropy constant at $2.2 \times 10^5 \text{ J/m}^3$ for nanoparticles less than 10 nm in diameter at 90 C, and even higher at room temperature than magnetite, Fe_3O_4 , is at $-1.1 \times 10^5 \text{ J/m}^3$ a room temperature The self-assembly of magnetic nanostructures comprising of cobalt ferrite in whole or part are of interest when their resulting morphologies provide magnetic, electric, physical, or mechanical property enhancement. For example, self-assembly of a magnetic material onto a conductive material has been reported where CoFe_2O_4 nanopillars were grown onto a SrRuO_3 substrate generating a large magnetoresistance effect due to the interface.⁸⁹ Magnetic property enhancement has been reported where magnetization values measured of high moment FeCo alloy cubes ($>175 \text{ emu/g}$) lower than when they were self-assembled into FeCo linear chains ($>210 \text{ emu/g}$). The enhanced saturation magnetization values were a result of the high aspect ratio of the chain morphology providing a longitudinal concentration of magnetic flux (Φ) throughout each chain length

enabling the chain to act a single magnet.⁷⁹ In this work, self-assembled cobalt ferrite (CoFe_2O_4) micropillars (CFO MPs) were synthesized using polyol process via hot injection of metallic precursor. An overall magnetic anisotropy is demonstrated making them suitable structures to selective actuation in soft-robot technologies where ferrite particles have been aligned and embedded into a light-weight polymer allowing for selective actuation by varying an external magnetic field.⁷⁴ Further applications of the CFO MPs include ferro-fluids when concentrated to unique light attenuation in fluids, also demonstrated.

6.3 Experimental

Preparation of the CFO MPs involved two steps as shown below.

6.3.1 Precursor A: Oxidation of Triethylene Glycol

First 10 mL of triethylene glycol (Alfa-Aesar) and 7 g of NaOH were mixed with magnetic stirring for about 15 minutes under air with heating up to 150 C. The resulting solution appeared dark brown, precursor A.

6.3.2 Precursor B: Dissolution of Metallic Salts

Into a pyrex beaker, 0.4 g of cobalt (II) acetate tetrahydrate and 0.4 g iron (II) chloride were added to approximately 10 mL of triethylene glycol (TEG) following dissolution by preheating to 80 C while under nitrogen bubbling. Magnetic stirring was done with magnetic stir/hotplate and Teflon stir bar.

6.3.3 Synthesis of Cobalt Ferrite Micropillars

Holding the temperature of precursor A at 150 ± 10 C, and using a 10 mL polypropylene syringe containing precursor B, introduction of precursor B into precursor A was performed. Mixing was facilitated by magnetic stirring. The complete addition of all 10 mL was performed within 1 minute. The solution color became dark brown, then within 1 minute, black. The resulting solution shares properties of a ferro-fluid when a rare magnet is placed near as forced curvature of the liquid-surface interface becomes pronounced when magnetized. In order to separate all particles, repeated washings in MeOH were performed following sonication for 15 minutes.

6.3.4 Characterization

Phase identification of the CFO MPs particles was done so on an X'Pert Pro Panalytical X-ray diffractometer in a Bragg-Brentano (Theta-2Theta) configuration. The CFO MP sample was magnetically manipulated and centered onto a shallow well low background oriented silicon wafer (single crystal) substrate. To investigate the magnetic properties of the CFO sample, magnetic characterization by gathering M-H curves was performed on a Quantum Design VSM (vibrating sample magnetometer) from 3T to -3T. Similar to all procedures previously mentioned in the magnetic characterization of prior chapters, the powder samples were weighed carefully into polypropylene capsules and magnetically aligned using an (rare earth magnet, N55) external field while embedded into formvar polymer. (The formvar powder was cured using chloroform and dried in vacuum for 24 hrs. prior to analysis.) This orientation of the MPs would allow different positions of the high aspect ratio structures with respect to the measuring field of the VSM. For field orientation in the VSM, refer to chapter 2, Characterization Techniques. When properly executed, the samples will maintain respective parallel or perpendicular orientation to the measuring field in the VSM. TEM was employed to investigate

the morphology and to perform phase confirmation using SAED. HRTEM, an interference technique, was performed to measure d-spacing and correlate an observed plane with a Bragg reflection from XRD. In general, larger d-spacing are easier to image and will have lower corresponding 2theta values in XRD diffractograms. To observe topography and confirm structural continuity of the CFO micropillars, a Hitachi SU-70 FE-SEM was used. The sample was drop cast onto a TEM grid and mounted onto a TEM grid sample holder used for STEM analysis. A UV-spectrophotometer Genysys was employed for the UV-vis absorption data acquisition. A rare earth magnet was placed directly above a quartz cell filled with the appropriate dilutions of CFO MPs in alcohol. Three magnet orientations discussed in detail later along with the absence of a magnetic field were maintained during each absorption scan from 1100 to 190 nm using a Xe lamp.

6.4 Results and Discussion

Phase identification of the as-synthesized cobalt ferrite phase is shown below in figure 1 where the calculated crystallite size was around 10 nm by Scherrer analysis of the (311).

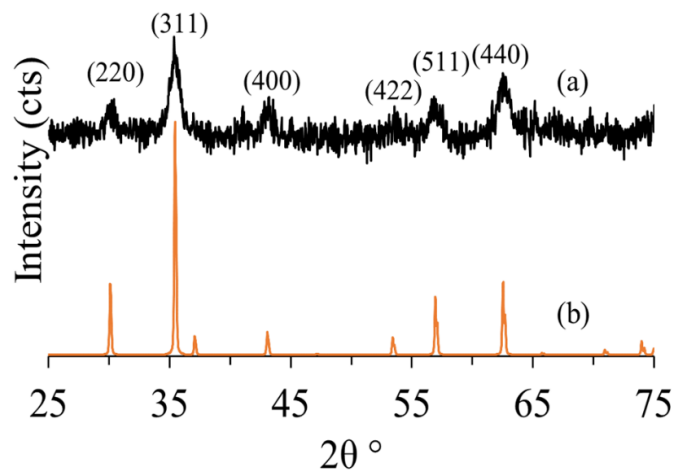


Figure 6.1: XRD of as-synthesized micropillar sample indicating cobalt ferrite phase presence in (a) as compared with ref. scan (pdf: 01-079-1744) in (b).

In order to probe for various CFO MP sizes throughout the sample, a portion of the as-synthesized CFO MP sample was filtered using a 0.45 micron PTFE syringe filter. The resulting solution appears less responsive to an external rare magnet and was further analyzed by TEM and VSM

Structural characterization was probed by TEM (transmission electron microscopy) including SAED (selected area electron diffraction) to further confirm the cobalt ferrite phase shown together with SEM and particle size distribution (inset, d) in figure 6.2. TEMs and SEMs of the as-synthesized cobalt ferrite show high aspect ratio micropillar morphologies having diameters roughly in the 200-300 nm range.

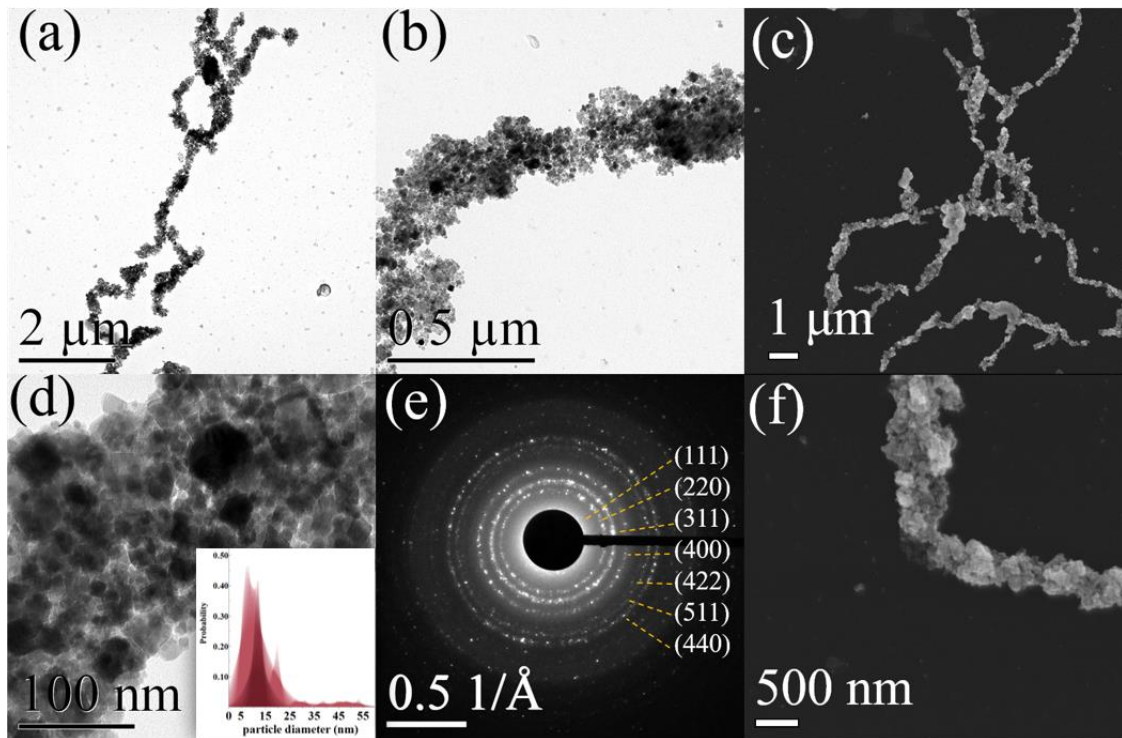


Figure 6.2: TEM images of CFO micropillar (filtered 0.5 μ) shown in (a), (b) and (d) with SAED indicating CFO phase in (e) and SEM images in (c) and (f). Shadowgram given in inset of (d) with average particle diameter at 13 ± 9 nm (filtered with most magnetically responsive particles removed).

The SAED pattern figure 2(e) confirm the cobalt ferrite phase (pdf: 01-079-1744) shown in the XRD of figure 1. The presence of the (111) as seen in figure 2(e) is not shown in figure 1 due scan range starting at 25 2Theta. The average particle diameter size was measured to be ≈ 15 nm (inset, d, figure 2).

Cobalt ferrites may possess magnetic properties ranging from hard to soft depending on the physical properties. The CFO micropillar system synthesized in this work possess magnetically soft properties as indicated by low coercive values ≈ 50 Oe (300 K) from the hysteresis curves in figure 6.3 of two sample orientations, parallel (a) and perpendicular (b) to the measuring field (H_{ext}). The observation of such low H_c indicates a significant population of particles possessing diameters below the single domain limit for cobalt ferrite, $D_{cr} \approx 100$ nm as based on the Kittel formula. It is important to mention that reported values for D_{cr} may vary where for example coercivity measurements were used to estimate a $D_{cr} \approx 70$ nm.⁹⁰ Furthermore, at particle sizes less than D_{cr} and approaching the superparamagnetic diameter for cobalt ferrite, SPM_{cr} , the coercive field decreases as the particle domain wall width becomes larger than the average grain size. Néel theory estimates a $SPM_{cr} \approx 10$ nm for cobalt ferrite of which several particles are observed near or below this diameter shown in the TEM images from figure 2 (d).⁹⁰ These ultrafine particles create SPM relaxations within the CFO MPs accounting for the decreased H_c values observed. Near zero-field, figure 3 inset, indicate remanence in both curves and some hysteresis loss depicting ferro- or ferrimagnetism.

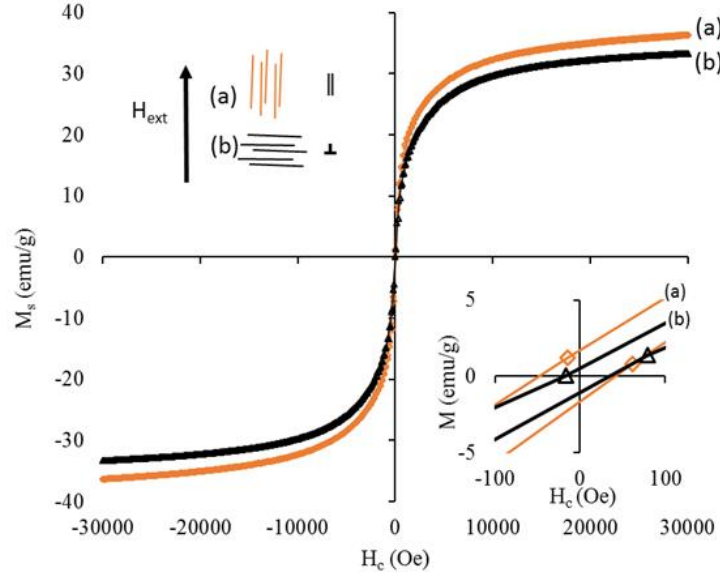


Figure 6.3: Hysteresis curves of CFO micropillars (filtered-0.5 μ and immobilized via formvar) indicating low- H_c and M_s of 33 and 36 emu/g when magnetically oriented perpendicular and parallel to the external measuring field all acquired at 300 K (filtered with most magnetically responsive particles removed).

Hysteresis measurement at 50 K of the non-oriented MP sample possesses an $H_c > 8$ kOe (data not shown) as a result of freezing of the surface spins of the smallest sized CFO nanoparticles. A drop (or kink) in magnetization near $H=0$ Oe indicates presence of a soft phase such as Fe, However, no such phase was detected using diffraction methods.⁵⁴ The freezing of surface spins may occur at temperatures well below the blocking temperature where SPM relaxations no longer occur on the time scale of the measurement but rather are locked into particular magnetizations. The temperature dependent effective magnetic anisotropy constant, $K_{an}(T_b)$, based on Langevin theory where $T_b \approx 350$ K determined by zero-field and field cooled susceptibility measurements was calculated in equation (1) to give a $K_{an}(T_b)=1.91 \times 10^5$ J/m³.^{91,92}

$$K_{an}(T_b) = (19.6 \times 10^5) e^{(-1.9 \times 10^{-5} \times T_b^2)} \frac{erg}{cm^3} \quad (1)$$

Substituting $K_{an}(T_b)$ into equation (2), also from Langevin theory, where k_B is the Boltzmann constant and V is the particle volume, an average cobalt ferrite nanoparticle diameter was calculated to be ≈ 10.7 nm.^{41,93}

$$K_{an}(T_b)V = 25k_B T_b \quad (2)$$

This value is somewhat lower than the diameter determined by TEM however is in good agreement with the average crystallite size as calculated by Scherrer when considering non-magnetic dead layers due to adventitious carbon. Intriguingly however, the CFO MPs possess overall magnetic anisotropy as indicated by the VSM measurements having larger magnetization when the MPs are aligned parallel to external measurement field with saturation magnetization increased up to 10 % from 33 emu/g to above 36 emu/g in figure 3, (b) and (a) respectively. It is also important to mention the slight enhancement in maximum permeability, μ_M , seen from figure 3 (a), inset.

A dilute suspension (MeOH) of CFO MPs was shown to effectively attenuate the incident light (ThermoScientific Genesys 10S UV-Vis, Xenon flash lamp) when the CFO MPs were magnetically oriented using a rare earth magnet. When the micropillars were oriented parallel to the incident wavelength, a decrease in absorbance was observable in the visible up to UV region, while in stark contrast, an increase in the IR region absorbance was detected > 900 nm. A perpendicular orientation of the MPs produced strong absorbance in the visible region up to the UV region while a decrease in absorption of the IR region was observed.

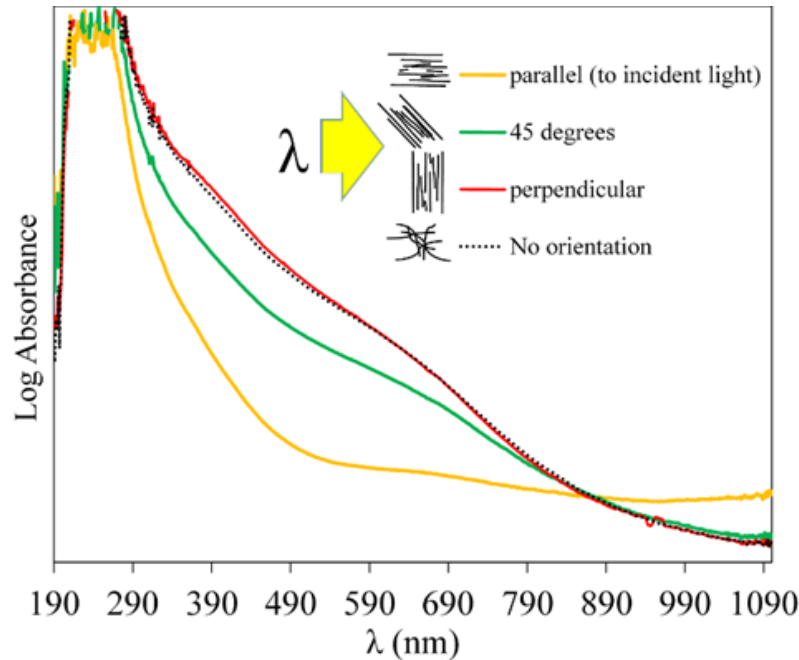


Figure 6.4: UV-vis spectra overlay of magnetically oriented CFO MPs. Parallel (yellow), 45 degrees (green), perpendicular (red) and no orientation (black-dotted) of CFO MPs suspended in R-OH (filtered and the most magnetically responsive particles were removed).

These observations suggest the MPs may have an increase of absorption at incident wavelength in the far-IR and microwave region.⁹⁴ Furthermore, a red-shift from about 630 nm to 670 nm indicates the presence of a magneto-optic effect, in particular, magneto-birefringence. The nanostructure of the CFO micropillars contain particles that are very close in distance to one another and individually behave as oscillating dipoles when polarized by incident light. The particle dipoles interact between particles at very close distances (inversely proportional to d^3). Asymmetry in the oscillating dipole interactions is dependent on the pillar orientation with respect to direction of the polarization of the incident light. This has been referred to as oscillating dipole interaction anisotropy.^{95,96} The magneto-birefringence effect gives a change in refractive index (Δn) between the parallel and perpendicular orientations of the CFO MPs and explains the red shift (inversely proportional) in the UV-vis spectrum between the two CFO MP

orientations.⁹⁵ Figure 6.5 shows the observed color change between perpendicular and parallel magnetic field orientations of dilute and concentrated CFO MP suspensions.

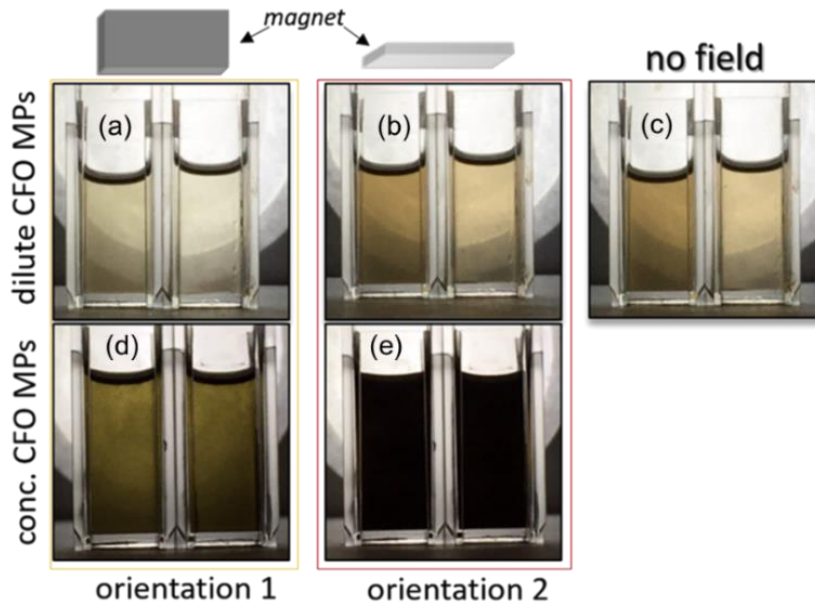


Figure 6.5. Images showing light transmission with two magnet orientations of diluted and concentrated CFO MPs suspended in various short chain alcohols (R-OH). Dilute CFO MPs in (a) and (b) with no magnet presence for dilute CFO MPs in (c) and concentrated CFO MPs in (d) and (e) (all samples shown were filtered with most magnetically responsive particles removed).

The observed red-shift from figure 6.4 (perpendicular) is represented by the flat magnet orientation in (b) and (e) of figure 6.5.

Optical microscopy images were gathered of the filtrate (filtered using 0.45 μm PFTE syringe filter) and those particles responding first to the magnetic field (rare earth magnet) were separated and embedded in transparent acrylic resin shown in figure 6.6 below. Large high aspect ratio CFO pillar-like structures are observed having random orientations. Several structures in figure 6.6 are several microns wide and $> 50 \mu\text{m}$ in length though some appear fragmented due to physical damage caused by mixing and stirring from the spatula.

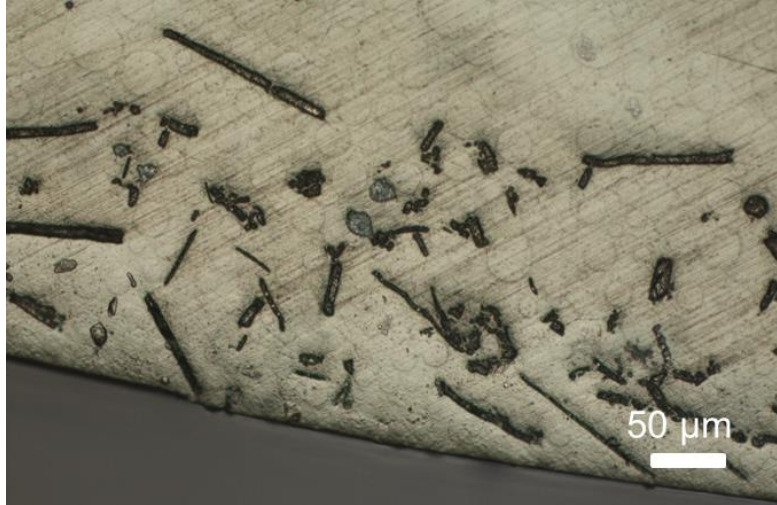


Figure 6.6: Optical microscope image taken of CFO micropillars (unfiltered, as-synthesized) showing the distinct high-aspect ratio morphology as well as a larger size distribution as compared with TEM and SEM images shown in figure 6.2.

HRTEM images were gathered shown in figure 6.7 (a) and (b) of the unfiltered as-synthesized CFO micropillars from figure 6.6. The CFO micropillars were again confirmed having nanostructure of 15-20 nm CFO nanoparticles which formed the overall material.

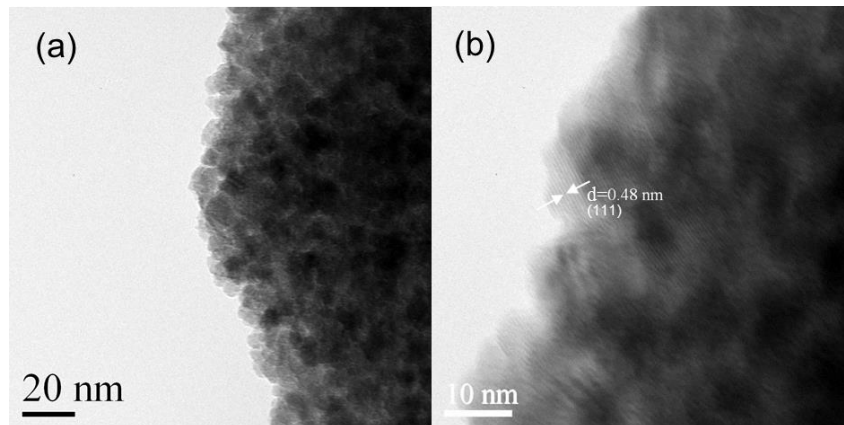


Figure 6.7: TEM images at low magnification (a) and high-resolution (b) showing the nanostructured CFO particles of a single CFO micropillar. HR-TEM in (b) is shows the (111) plane with d-spacing $\approx 0.48\text{nm}$ (unfiltered, as-synthesized).

The HRTEM image in (b) shows d-spacing = 0.48 nm which corresponds to the (111) plane not observed in XRD of figure 6.1 due to the limited scan range taken. M-H curves were acquired of

the as-synthesized CFO MPs at three different temperatures, 300, 250 and 200 K shown in figure 6.8. The H_c is shown at 300 K around 500 Oe, a significant increase from the filtered magnetically unresponsive sample M-H orientation study curves in figure 6.4 (a) and (b), while the M_s value is between the two orientations at 35 emu/g. This value as an intermediate value correlates well with the fact that, roughly 50 % have an orientation parallel and 50 % may have an orientation perpendicular to the measuring field of the VSM. However, the rather large increase in H_c is intriguing. Typically this observation could arise from larger particle sizes approaching the single domain particle diameter limit from the superparamagnetic sizes for CFO around < 10 nm.⁹¹

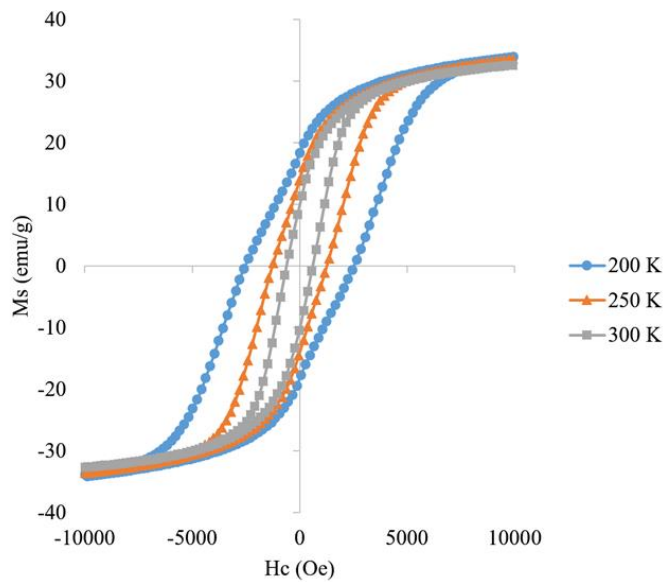


Figure 6.8. Hysteresis overlays at 300, 250 and 200 K demonstrating relative exponential increase of coercivity at lower temperatures of the unfiltered, as-synthesized CFO MPs.

For a detailed discussion involved the two types of CFO MP systems synthesized in this work. A study on the magnetic particle exchange interactions in the particles of cobalt ferrite embedded into the nanostructured micropillars was performed. Isothermal remanence (IRM) curves as well as demagnetization curves (DCD) were acquired of the as-synthesized CFO MP sample at 300 K

using a 2 second delay at each field step in (a), 10 second delay at each field step and at 300 K in (b), and finally 10 second delay at each field step at 320 K in (c). Acquisition of the IRM/DCD curves using VSM was discussed previously in this chapter. From (a), several spikes in M_r are observed smoothing out to a plateau in M_r around 6500 Oe with negligible interaction between particles at higher fields while in (b), a smoother M_r curve is generated with the plateau in M_r occurring at a somewhat lower field of 5500 Oe. This is explained by the increased field-hold time from 2 to 10 seconds used in (b). In (c), the sample was completely demagnetized, and remanence curves were acquired with the same settings as (b) but at slightly elevated temperature of 320 K. A slightly decreased remanence is observed as compared with (b) due to the thermal energy increase effect on the magnetization observed since the remanence is a larger fraction of the normalized magnetization. The remanence gives a marked plateau >5500 Oe as in the case of (b). The change in magnetization (green plots) were plotted for (a), (b) and (c) and indicate a positive exchange interaction at fields equal to 2000 Oe or below and above display random and positive and negative exchange interactions up to several thousand Oe.

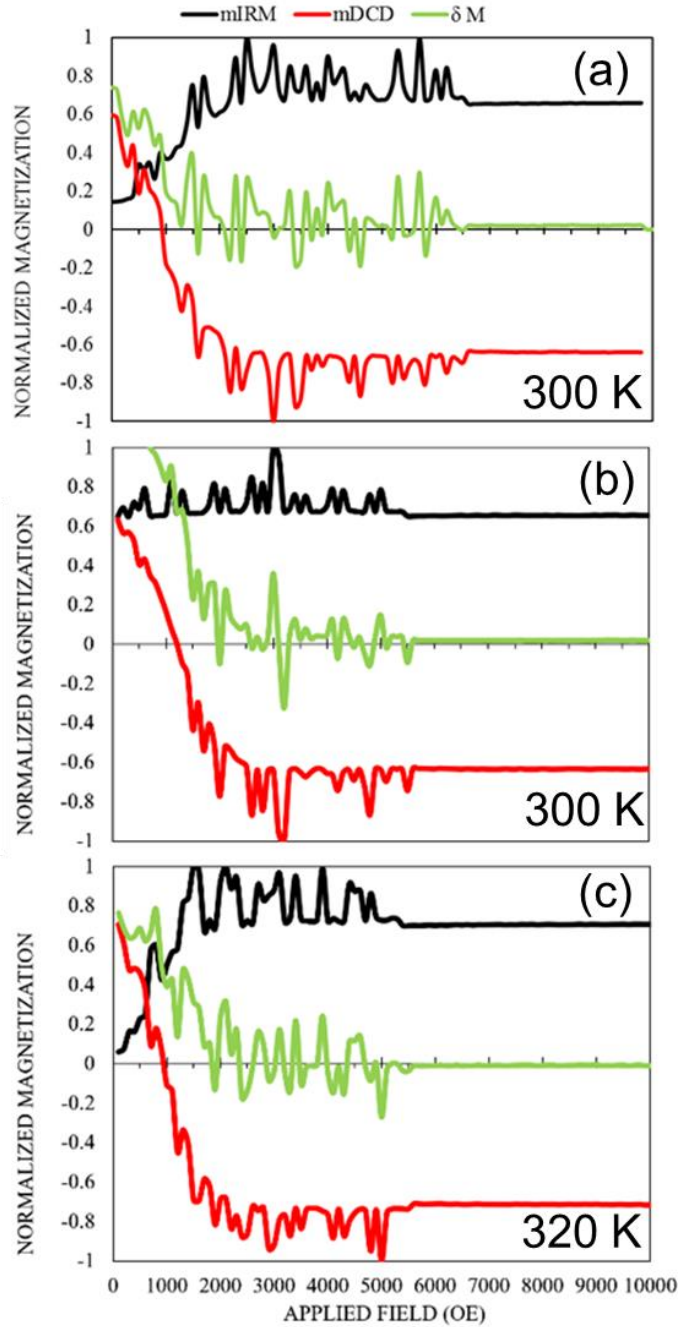


Figure 6.9: Reduced remanence curves, mIRM/mDCD (black/red), with delta M plots (green) overlaid using 2 second delay at 100 Oe steps (300 K) in (a), 10 sec delay at 300 K in (b), and 10 second delay at 320 K (c) performed on free CFO MP powder sample. Delta M indicates positive or negative particle-particle exchange interactions (sample was unfiltered, as-synthesized).

The random spikes in remanence are likely attributed to the relaxation time of cobalt ferrite nanoparticles of small sizes: a significant population approach and are at the superparamagnetic

limit (see inset of shadowgram in (d) figure 6.2). These superparamagnetic relaxations occur intermittently through the remanence measurement while the larger CFO particle volumes present in the nanostructure provide the stable or underlying remanence observed in all of the IRM/DCD plots. The larger particles provide stable moments which may be polarized to saturation due to the (ferri-) ferromagnetic nature of the cobalt ferrite phase.

6.5 Conclusion

We have demonstrated the synthesis of self-assembled cobalt ferrite micropillars using the polyol process via hot injection method. This CFO MPs are nanostructured transition metal oxides of ≈ 15 nm cobalt ferrite particles self-assembled into high aspect ratio micropillars. The CFO micropillars exhibit the magneto-birefringence effect as observed by a wavelength shift in the magnetic orientation UV-vis study. The non-diluted CFO MP solution behaves as a conventional ferro-fluid while subsequent dilution and characterization unveil the CFO micropillar-structure. These magnetic fluids have potential beyond ferro-fluids such as light modulator devices, optic switches and tunable gratings where selective wavelength may be maintained through fiber optics devices.^{96,97} From the structural standpoint, magnetic anisotropy is present in these high aspect ratio CFO MP structures allowing for usage in selective actuation technology when they are oriented appropriately into low density “smart materials”.

Section 2: Continuous Flow: Polyol Process and Aqueous Reduction

Chapter 7. Co Nanoparticle Synthesis in a Microfluidic Reactor

7.1 Overview

In section 1, investigation into high aspect ratio structures of FeCo alloy was performed in chapter 3, 4 and 5 and cobalt ferrite in chapter 6, which all used variations of the polyol process. Section 2 changes the synthetic route to focus on continuous flow syntheses of the premiere soft ferromagnetic materials of Co and FeCo using aqueous reduction and polyol methods respectively. Exploration of non-conventional synthetic approaches, such as flow synthesis of metal nanoparticles can have the benefit of high output demonstration which is a major goal of the last two chapters in the dissertation. A complimentary goal; however, was to demonstrate the novelty the novelty of synthesizing these magnetic nanomaterials using continuous flow synthesis.

7.2 Introduction

Co is a ferromagnetic element with curie point at 1400 K that crystallizing in the hcp or fcc structure.² Bulk Co (hcp) has $K_1=4.12 \times 10^5 \text{ J/m}^3$ higher than that of Fe (bcc) at 4.8×10^4 while at the nanoscale, they possess critical single domain diameters of 96.4 and 19.0 nm respectively.⁹⁸ ^{6,99} Cobalt is crucial and probably one of the most important ferromagnetic elements for enhancing the thermal properties (high Curie point) of several key high permeability magnetic materials such as FeCo-based alloys such as HITPERM.^{11,14,15,18} In addition, switching devices such as reed switches and magnetic sensors operating in high temperature environments are a suitable application for Co NPs.¹⁰⁰

A continuous flow synthesis of a product involves an uninterrupted flow of two or more reaction precursors which meet, react in some mixing zone to form a product of interest. It may be a compound, macromolecule or metal nanoparticle.⁴⁰⁻⁴⁶ Continuous flow syntheses can be used to

perform a variety of organic reactions such as Heck, hydrogenation, click, enolation and halogenation routes to name a few.⁴⁰ Microreactors are also fabricated from virtually any material imaginable in order to withstand harsh chemical and high temperature environments; these construction materials can range from ceramic, glass, plastic, silicon and stainless steel.^{38,40}

Metal nanoparticles of Fe with work-like morphologies have been synthesized at room temperature using microfluidic synthesis.¹⁰¹ Saturation values were reported at about 70 emu/g at 300K. Another microfluidic synthesis reported was that of magnetite-chiton composites capable of drug loading.⁴⁷ No report existed on the synthesis of cobalt nanoparticles using a microfluidic reactor which was a motivating factor for performing this work.

7.3 Experimental

The synthesis of cobalt was performed at room temperature using hazardous chemicals such as hydrazine and caustic sodium hydroxide. The microfluidic assembly chosen to do this work was an Ehrfeld Microtechnik BTS Modular MicroReactor System microreactor with the schematic given below in figure 7.1.

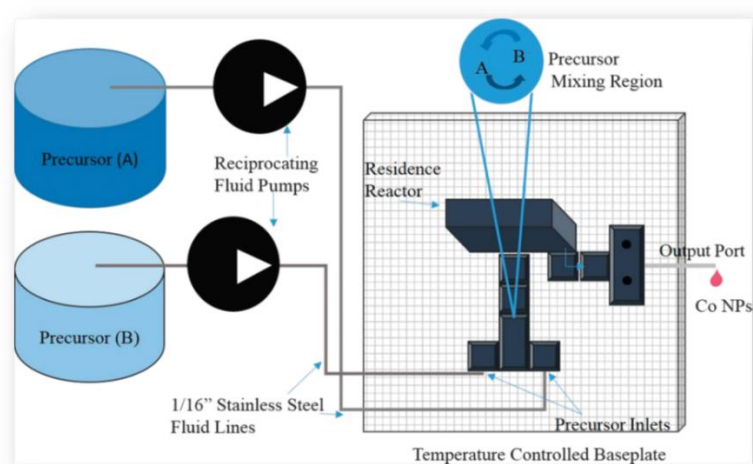


Figure 7.1. Microreactor assembly used to perform the continuous flow synthesis of cobalt nanoparticles.

The assembly had a temperature controlled aluminum base equipped with a grid for component attachment. Both precursors were pumped through 1/16 "OD stainless steel tubing into fluid inlets connected to a mixing chambers where both precursors initially combine. Following this, the reactive media flowed through a residence reactor block following a short residence time of less than 2 minutes.

7.3.1 Synthesis of Co Nanoparticles in Continuous Flow

The metal precursor salt, $\text{CoCl}_2 \cdot 6\text{H}_2\text{O}$, was massed and added to ethanol to give a total concentration of 0.2 M. The resulting color of this solution was a dark blue. A hydrazine alkaline mixture was prepared by cautiously adding hydrazine hydrate (98 %) into about a 25 M NaOH to give a 1:1 hydrazine:OH molar ratio. The overall molar ratio of hydrazine to the metallic salt was 1:18.

Both precursors were pumped using Knauer Smartline 1050 syringe pumps pumped through stainless steel lines to the microreactor inlets. It is important to mention that no heating source was used for this reaction, that is, it was performed at room temperature. Cobalt NP generation occurred within 1-2 minutes after initiating the pumping action of both precursors. A pink solution was pumped from the output port and Co NPs were precipitated using the assistance of a rare earth permanent magnet.

The Co NPs were washed three times with methanol and vacuum dried for 24 hours to remove solvent. Below in figure 7.2, a reaction scheme is presented showing the precursors in 1.) and 2.) and the combination thereof. From figure 7.2, an ethanolic cobalt complex while the strong base deprotonates the hydrazine to form water and provide the electron for reduction of Co^0 releasing nitrogen gas. The entire reaction occurred at room temperature.



Figure 7.2: The reaction scheme if given for the EHAS system used in this work to produce Co NPs.

The Co NPs were synthesized from the output port of the microreactor at a rate that exceeded 1g/hr.

7.3.2 Characterization

The XRD performed in this work was done on a Panalytical MPD X'Pert Pro X-ray diffractometer using a PMT detector with receiving slit at 1° , anti-scatter slit at 1° , programmable divergence slit at 0.5° and a 15 mm mask. The scan range performed in this work was $30 - 80 2\theta^\circ$. The sample was prepared onto a low background Si wafer to reduce parasitic signal from the substrate. The X-ray power conditions were 45kV and $40 \mu\text{A}$ and used a Cu K_α X-ray source. The TEM imaging in this work was acquired using a Zeiss Libra 120 operating at 120 keV. The sample was prepared by traditional drop-cast method where a dilute solution of sample was suspended by sonication in EtOH and 3 drops were placed onto a TEM grid with 5-minute drying intervals. The TEM sample grid used in this work were Ted Pella formvar coated 300 mesh Cu grids. The TEM preparation was allowed to dry in vacuum for 24 hours to ensure solvent removal and stabilization of the Co NPs by physisorption onto the formvar surface.

EFTEM was performed by first confirming presence of Co by acquiring an EELS spectrum. To acquire to EELS spectrum for Co, the zero loss beam was calibrated by centering it with respect to the GATAN camera software. Following this, a turbo spectrum of the ZLP was acquired at lowest illumination angles as to not burn the CCD. The turbo spectrum was centered manually

matching the ZLP peak to 0 eV. Working at 40x (spectrum magnification), the electron loss energy was set to 900 eV manually to ensure capture of the Co edge around 780 eV. An EELS spectrum was acquired which confirmed presence of Co near 780 eV. To acquire an EFTEM, or elemental map, a slit aperture was inserted to the focus on the appropriate energy window for Co which required a slit width of 40 eV. Two pre-edge maps and one post-edge map was acquired and the EELS background was extrapolated, a commonly used EFI (energy filtered imaging) technique method.¹⁰² It is important to note that no overlap from Fe was possible as Fe was not present in the EELS spectrum, a common set-back when acquiring elements having closely related energies.¹⁰³ The Co NPs were mounted onto indium foil and fastened to a sample holder using carbon tape.

X-ray photoelectron spectroscopy is a surface sensitive technique used to probe chemical states and compositions at the first 10 nm under a surface. Photoelectrons are emitted having energies characteristic of not only elements present, but their chemical oxidation states as well making XPS a very powerful tool for surface analysis. XPS (X-ray photoelectron spectroscopy) was performed on a Thermo-Scientific ESCALAB 250 spectrometer equipped with focused monochromatic Al K α X-ray (1486.6 eV) source. The x-ray spot size was equal to 500 μ m. The incident X-ray beam was at 45° from normal to the surface of the sample and the X-ray photoelectron detector was positioned normal to the sample. Ar sputtering could reduce cobalt oxides, the XPS scans acquired in this work were performed using both charge and no charge compensation. Runs performed using charge compensation used both an internal as well as a low energy Ar⁺ external flood gun. Both scan types indicated similar spectra. S/N was increased by use of a large area XL magnetic lens. A constant analyzer energy (CAE) mode was done (pass

energy = 20 eV. For the scan in (B), small a step size of 0.1 eV for the detailed spectra and 1 eV for the survey scan respectively was chosen.

The Co NPs synthesized by continuous flow were magnetically characterizing by vibrating sample magnetometry (VSM). The powder sample was carefully placed into a polypropylene capsule having low magnetic signature and was massed to give a sample mass in the range of 1-10 mg. Too low of a mass requires higher V sensitivity settings in the pickup coils while too high of a mass can saturate the limit of detecting which requires a larger V range. The capsule containing the powder was centered into a snap-tube made of brass, also containing low magnetic signature (emu^{-6}) and threaded onto a VSM fiberglass sample rod quipped with an internal reference magnet. The sample rod was carefully loaded into the instrument and sealed with a cap and evacuated down to about 10 Torr or less. An M-H curve at 300 K was acquired of the centered Co powders in a field from -3 to 3 T at a vibrational frequency of 40 Hz at 2mm amplitude.

7.4 Results and Discussion

In order to investigate the phase, XRD was performed on the as-synthesize Co NPs with a scan from 30 to 80 $^{\circ}2\theta$. Three phases were detected: Co (fcc), Co (hcp) and CoO (shown in figure7.3, Co (fcc) powder-diffraction file: 00-015-0806, Co (hcp) (powder-diffraction file: 00-001-1277) and CoO (powder-diffraction file: 01-076-3829).

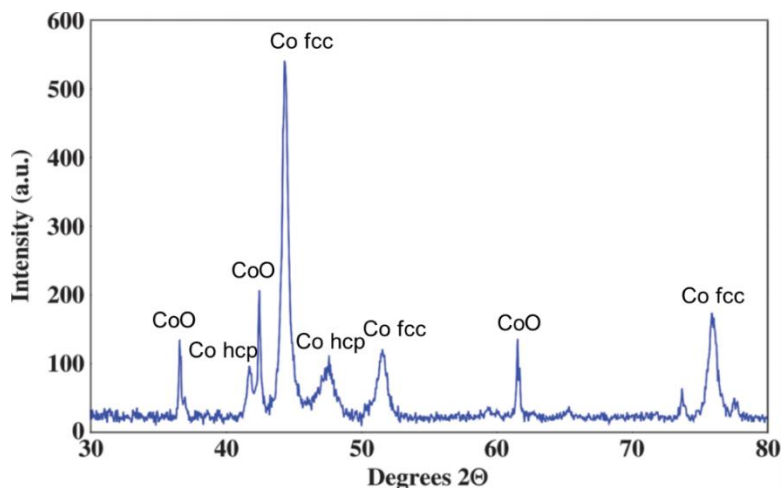


Figure 7.3: XRD of as-synthesized Co NPs showing three phases, Co fcc, Co hcp and CoO.

To investigate the particle morphology, TEM imaging was gathered and shown in figure 7.4 below. A particle diameter average was measure to be 30 ± 10 nm as seen from the PSD plot to the left in figure 7.4. In addition, a Co EFTEM was acquired shown in the inset of the BFTEM image indicating elemental Co is homogenous in the particle sample. Other contaminants are shown in the BFTEM with do not contain cobalt which may be attributed to Na containing reaction by-products.

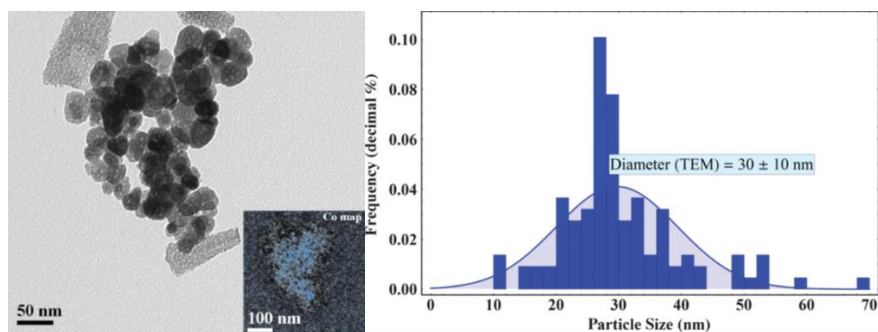


Figure 7.4: BTTEM of Co NPs (as-synthesized) via continuous flow using the EHAS system (a-f) with inset of (d) showing Co EF-TEM.

Characterization of the surface by XPS (x-ray photoelectron spectroscopy) was done to determine if the CoO was an oxide later on all Co particle surfaces or if the oxide phase was in the form of core nanoparticles. The XPS survey scan from 0 – 1300 eV was acquired and is

given in (A) of figure 7.5 along with the Co region scan in (B). Observed binding energies corresponded to the carbon at 284.8 eV. Survey scans show presence of Co, O, C, and also some small amount of Na. Na is a trace of the reactant, which was used for the synthesis. Cobalt 2p_{3/2} spectrum shows a signal having a maximum at 780.1 eV which is correlated with cobalt oxide (CoO).¹⁰⁴⁻¹⁰⁶ The presence of Co²⁺ was substantiated by the small peak at 786.1 eV (given in indicated in (B) of figure 7.5 (by arrow), which is known marker for cobalt (II) oxide.¹⁰⁵ Co⁰ has a peak at 778.3 eV, but this was not observed. However, as it is mentioned above, the presence of metallic Co⁰ in two phases was found with XRD analysis. This leads to the conclusion that Co⁰ is the nanoparticle core under the CoO layer. The Co metal signal is not detected by XPS analysis due to short attenuation lengths of the photoelectrons. In the case of Co, the first 10 nm of the particle surface or less is the sample depth typically detectable by XPS.^{107 b}

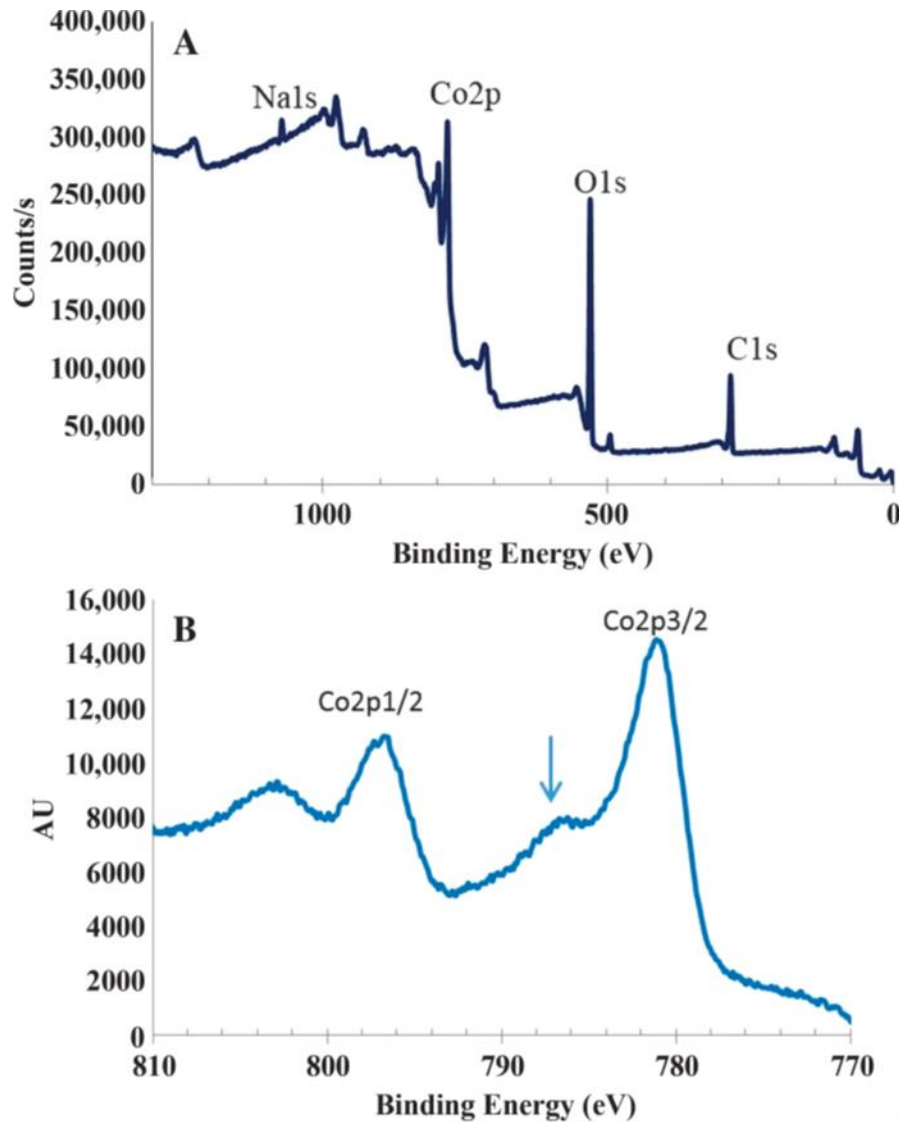


Figure 7.5: XPS spectra of as-synthesized Co NPs indicating Co^{2+} around 786 eV rather than Co^0 attributed to an oxide layer on all particles.^b

An M-H curve was acquired of the as-synthesized Co NPs by vibrating sample magnetometry and was generated at room temperature (300 K) shown in figure 7.6. The Co NPs had an M_s of 125 emu/g and H_c of 120 Oe found by the hysteresis curve in figure 7.6.

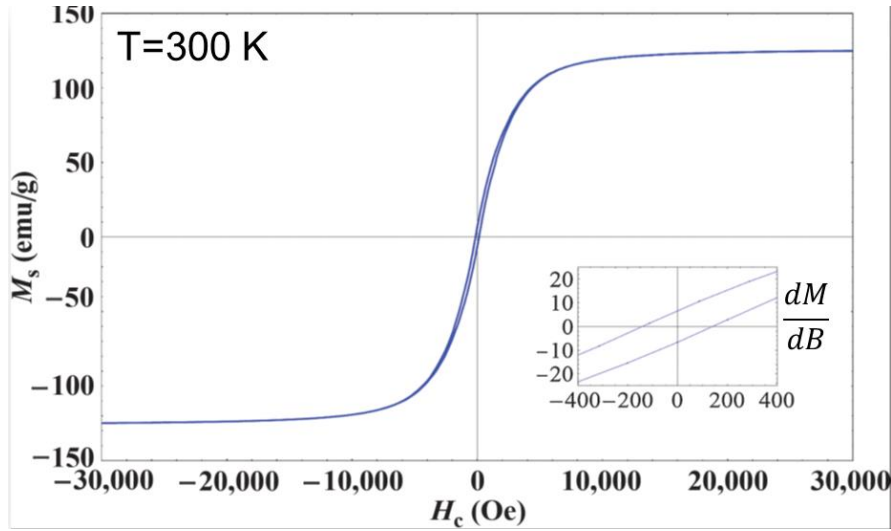


Figure 7.6: Hysteresis curve of as-synthesized Co NPs possessing saturation magnetization of 125 emu/g and H_c of 170 Oe taken at 300 K.

The inset in figure 7.6 (lower left) is that of the near zero field region of the M-H curve of the Co NPs. This estimated slope is mentioned and used for calculations explained below in the discussion section.

The as-synthesized Co NPs produced in this work by continuous flow chemistry possess the appropriate magnetic properties of nanoparticles of this size range. They possess M_s values significantly lower than those from bulk Co (fcc), ≈ 162.5 emu/g, however, this is explained by the presence of CoO layers, an antiferromagnetic below about 290 K.³ This secondary oxide phase decrease the average particle moment compounded with smaller particle volumes where higher surface area promotes dilution of spins per unit volume or mass. An upper bound estimate for the magnetic particle volume moment, μ , can be performed by finding the slope, dM/dB near zero field shown in eq. (1) and (2) below, where saturation magnetization, M_s , Boltzmann constant, kB and the M-H curve measurement temperature, T , are known.

$$\frac{dM}{dB} B \rightarrow 0 = \frac{M_s \mu}{3kBT} \quad (1)$$

$$\mu = \frac{3kBT \left[\frac{dM}{dB} B \rightarrow 0 \right]}{Ms} \quad (2)$$

If the particles are assumed to be spherical, then the relation with the magnetic moment per particle, μ , and the particle volume, V , is given in eq. (3) holds where $M(vol)$ is the volume magnetization.

$$V = \frac{\mu}{M(vol)} = \frac{\pi d^3}{6} \quad (3)$$

The density of Co, ρ , (density for bulk Co) may be incorporated below in eq. (4) in order to convert $M(vol)$ to Ms (by mass) and the upper bound estimate for the magnetic core size, commonly referred to as the domain size was calculated to be ≈ 6 nm.^{41,87,108,109}

$$D(mag. core) = \left[\frac{18 kBT \left[\frac{dM}{dB} \right]}{\rho \pi Ms^2} \right]^{1/3} \quad (4)$$

7.5 Conclusion

Co NPs synthesized were synthesized successfully for the first time using a microfluidic reactor. The Co NPs were produced at a high rate of 1 g/hr which was a secondary goal for performing the work in this chapter; in addition, it proved the concept for this aqueous reduction process for having industrial applicability for scale-up production. This synthetic work is also intended for further study on manipulating magnetic properties in flow by fine-tuning or judicious adjustment of reaction precursors. Extrinsic properties such as coercivity may be tuned. Also incorporation of real-time magnetic analysis as the material is synthesized would also be ideal for quick magnetic characterizations as many products synthesized in flow are routinely analyzed as they are made using UV-vis, FTIR and HPLC etc.^{38,42}

The final chapter of section 2. Chapter 8, concludes the CF work by exploration in the continuous flow synthesis of FeCo alloy. The synthesis work explained in section 1 is based on the previously discussed findings on the polyol process and the local optimizations performed in chapter 3 and 4. Any attempt to incorporate such similar chemistry into a CF scheme is not a trivial task.

Chapter 8. FeCo Nanomaterial Synthesis in Continuous Flow

8.1 Overview

The motivation for this work was to synthesize FeCo alloy as a pure phase using continuous flow (CF) chemistry based on the polyol process synthesis of FeCo performed in chapters 3 and 4. A secondary goal was to synthesize pure phase FeCo alloy as unique high aspect ratio geometries synthesized in chapter 4. In conducting this work, limitations of the CF process were also discovered due to a couple specific factors. One being that CF processes are often difficult tasks when pumping reaction media having higher viscosities than aqueous solvents etc. Polyhydric alcohols in general have a viscosity much higher than water due to the high relative amount of hydrogen bonding and may present difficulties in pumping etc. Other limitations of CF synthesis of FeCo are discussed in this final chapter of the flow chemistry work in section 2.

8.2 Introduction

Interest in exploring FeCo physical, magnetic and morphological properties using CF chemistry may be ideal for controlling these properties by simply varying precursor flow rates. Tunability of particle size and crystallinity are the key responses to target as they determine the overall magnetic properties. However, to control magnetic properties using such as reaction scheme requires that the magnetic phase of interest be synthesized to contain a 100 % composition. By achieving this, the magnetic properties can be directly analyzed for variation corresponding with flow rate adjustment, concentration variation in precursors as well as temperature and residence time (lower or higher flow rates for all precursors).

8.3 Experimental

This work incorporates equipment that is, in general, common to many academic research labs. Equipment required for the CF synthetic approach discussed below employed the use of, syringe

pumps (typically used for LC), peristaltic pumps (require proper diameter Tygon ® tubing for flow rate accuracy), mechanical stirrer, typical laboratory benchtop glassware, a heating source and necessary stainless steel or Tygon ® tubing for directed precursor transfer. The CF setup was manually assembled together component by component since this CF synthesis mandatorily departs from use of the compact Ehrfeld ® microreactor set-up used in chapter 7. This was primarily because of the high viscosity of the ethylene glycol solvent used.

8.3.1 Synthesis of FeCo in Continuous Flow

The metallic salt solution was prepared by massing Iron (II) chloride tetrahydrate and cobalt (II) acetate tetrahydrate to give an overall [Metal] of 0.7 M in ethylene glycol. The molar ratio was kept at 1.5 for Fe:Co. Heating was maintained at a temperature below 100 C for 1 hr. During this time, magnetic stirring by magnetic stir bar ensured complete dissolution while under nitrogen gas bubbling. A translucent fuchsia solution color was observed within 15-minute indicating dissolution had occurred. The initiator solution was prepared by dissolving NaOH pellets may be dissolved into water to achieve 18 M [NaOH].

A single cylindrical PTFE vessel (mounted onto the Argonaut Surveyor, 1” diameter, 8” length) was used to hold the reaction media. The temperature controlled heating jacket was set to 150 C and the aq. hydroxide precursor was pumped into the PTFE vessel at 0.4 mL/min using a sytolic pump (Knauer Smartline 1050) with the metallic precursor flow rate at 0.6 mL/min using a peristaltic pump. Vigorous mechanical stirring was performed after both flow rates were initiated and the temperature ramp rate was kept in the range of 8-13 C/min. Reaction vessel partially sealed purged with N₂ during the course of the continuous flow synthesis. Doing this eliminates excessive glycolaldehyde concentrations from forming as a results of oxidation of ethylene

glycol in air.^{77,110} Total reaction time is typically in the range of 13-25 minutes dependent on temperature ramp rate. Reaction temperature should not exceed 150C.

The reactor set-up is photographed in figure 8.1 below. It gives a perspective on the general layout with the systolic pump shown below used for pumping the hydroxide aqueous solution and the peristaltic pump (above) for pumping the ethylene glycol/metal precursor solution.



Figure 8.1: Photo of the involved continuous flow (CF) reactor set-up shown with systolic and peristaltic pumps (top), mechanical stirrer (top-left), reaction vessel (far left-center) and product vessel/round bottom flask (left-center).

The product is aspirated out of the PTFE reaction vessel after having reacted for the appropriate residence time (about 15 minutes) and is flowed into a holding vessel. From here the newly synthesized nanomaterial may be removed for further analysis using a pipette.

8.3.2 Characterization

X-ray diffractograms were acquired of the most magnetically responsive samples synthesized in the scan range of 30 -85 degrees 2 Theta to account for presence of both cobalt ferrite and FeCo alloy phases. The equipment used was a Panalytical MPD X'Pert Pro X-ray diffractometer equipped with a Pixcel detector and automatic beam attenuator and programmable divergence slits. The settings used for the x-ray diffraction analysis were a 1° receiving slit, 1° anti-scatter

slit and 0.5° programmable divergence slit with a 15 mm mask. All samples were mounted in a consistent manner with previous XRD analysis where the dried powders were placed within the well of a low background Si wafer. Using this substrate provides a smooth background with no parasitic diffraction from the substrate surface. All powders analyzed were washed with MeOH and dried overnight and analyzed within 24 hours of synthesis. SEM imaging was done using a Hitachi SU-70 FE-SEM. All dried magnetic powder samples were mounted onto double-sided carbon tape and mounted onto an aluminum coupon/substrate and threaded onto the appropriate SEM sample holder. All imaging was performed using an electron acceleration voltage of 5 KeV. All sample required no Pt or Au sputter coating deposition as charging artifacts were not present during SEM imaging. This is attributed to properly mounted powders close to the surface which help to promote conductivity within the sample prep curbing electron charge accumulation. Vibrating sample magnetometry was performed using the routine sample prep discussed in previous chapters. First the magnetic powder was dried and mounted into polypropylene capsules that possess low magnetic signature. The mass of the dried powder was recorded for purposes of presenting magnetization by mass. Following the sample preparation, the centering process was performed. The sample was manually snapped into place within a brass (half-moon) low magnetic signature (emu^{-6}) and centered at the 35 mm distance as required by the VSM manufacturer. The magnetometer used for this work was a Quantum Design Versalab with external field capability up to 3 T. Typical M-H curves were acquired of each sample to probe for FeCo alloy formation as demonstrated in the magnetic data X-Y plots in chapter 3.

8.4 Results and Discussion

Initial product generated using typically contained cobalt ferrite-rich materials. This is due to lower than optimum temperatures in the beginning phase of the CF process. It is encouraged to slightly modify flow rates in order to achieve desired product properties as possible. Below, a photograph of newly synthesized magnetic nanomaterial is shown entering a round bottom flask or holding vessel and the product is aspirated through the tubing seen on the right in figure 8.2.



Figure 8.2: Photo of round bottom flask used in the continuous flow synthesis of FeCo/cobalt ferrite product with input tube (left) shown carrying synthesized nanomaterial to a holding vessel with the second tube (right) generating the partial vacuum.

Aliquots were removed at 15 minute intervals and analyzed further. Below in figure 8.3 is an XRD scan of the nanomaterial containing the highest % composition of FeCo alloy. The maximum achieved FeCo alloy composition was approximately 20 %. It was found that this was

an inherent limitation due to the requirement of water as a solvent for the hydroxide initiator.

Water is well-known to catalyze the oxidation of Fe through several proposed mechanisms.^{57,58}

The other composition synthesized was the previously observed cobalt ferrite phase shown below in figure 8.3 at 80 %.

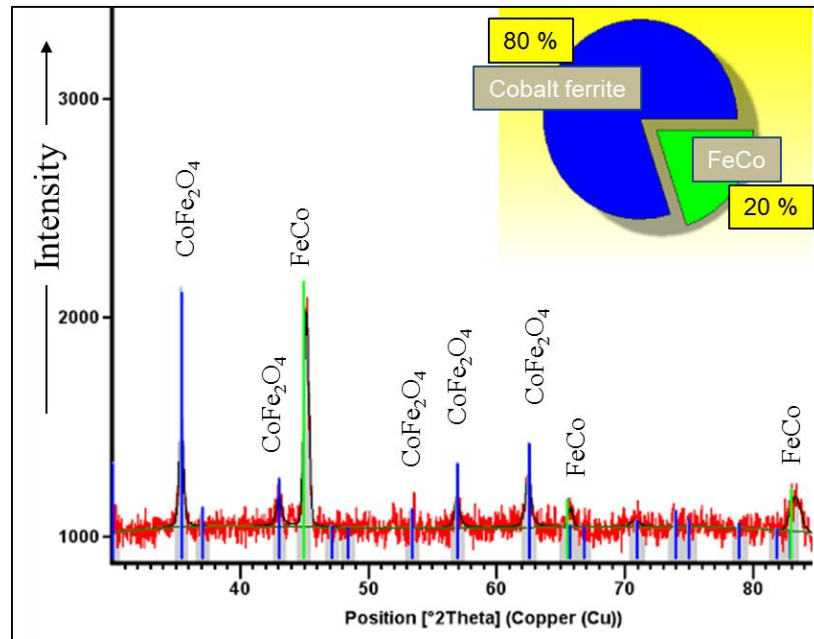


Figure 8.3: XRD showing maximum FeCo % of 20 % and 80 % CFO possible via CF polyol synthesis using 1.75 mL/min flow rate of hydroxide precursor and 0.6 mL/min metal precursor.

A morphological study was performed using various flow rates of the hydroxide precursor and are given below in figure 8.4 where samples were taken of a 0.4 mL/min, 0.6 mL/min, 0.8 mL and a 1.0 mL hydroxide flow rates. From the SEMs it is apparent that there is little to no morphological variation with hydroxide precursor flow rates. All samples produced 20 % FeCo alloy or less similar to the composition analysed in XRD figure 8.3.

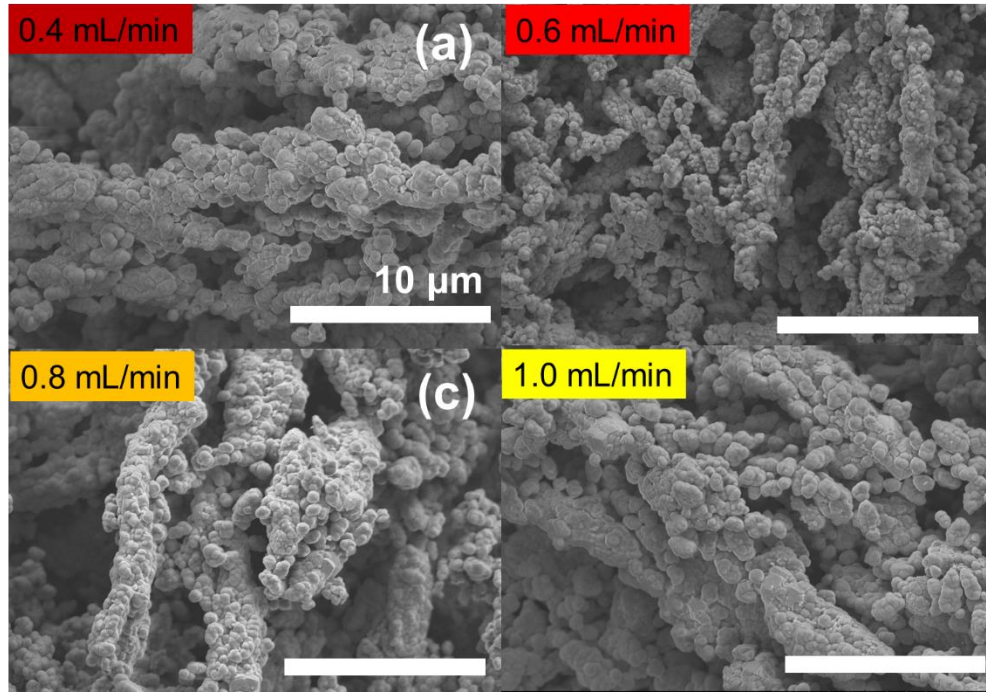


Figure 8.4: SEMs of FeCo/cobalt ferrite composites using 18 M OH with flow rates at 0.4 (a), 0.6 (b), 0.8 (c) and 1.0 mL/min (d) with metal precursor flow rate kept constant at 0.6 mL/min. Scale bars = 10 μ m.

If the flow rates were set at values exceeding those used in this work, the residence time for the reaction was not sufficient and unreacted non-magnetic material would flow into the holding vessel. It is apparent that the limited solubility of NaOH in water will unavoidable introduce excess water into the reaction media. This water accumulation catalyzes the oxidation of Fe in newly form FeCo particles. Methods to circumvent this issue may include cautiously melting NaOH pellets at just above the boiling point (318 C) and adding the liquid dropwise to the reaction media. Limitations on equipment that can perform such as task were realized, however PEEK tubing may be a possible candidate for transferring a melt of NaOH.

M-H curves of all materials had a maximum in saturation magnetization of 120 emu/g. This low value of M_s is indicative of an FeCo poor and CFO-rich mixtures of phases (figure 8.5).

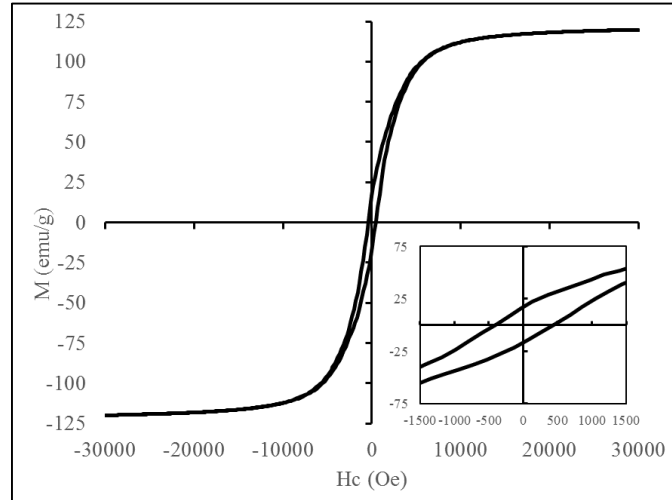


Figure 8.5: Hysteresis curve of 20 % FeCo/ 80% CFO mixture produced by CF with $M_s \approx 120$ emu/g and H_c of about 500 Oe.

8.6 Conclusion

Unfortunately, severe limitations exist when attempting to produce FeCo via continuous flow using the polyol process. The primary obstacle is producing NaOH into a sufficiently concentrated solution having minimal water content. Although synthesis of FeCo was successfully achieved in CF, its composition was not 100 %, with the remaining 80 % confirmed as cobalt ferrite. No other polar solvents are suitable for dissociation of NaOH, or can solubilize NaOH as well as H_2O . The alcohols such as MeOH and EtOH have poorer solubility. A way to address this issue is to completely remove the water content from the hydroxide precursor solution. As mentioned previously, if NaOH pellets could be heated to $> 318^\circ C$ above their boiling point and fed dropwise, or gravity fed, the success of synthesizing a pure phase FeCo in

flow using the polyol process may be achieved. This task is encouraged for future synthetic chemists experimenting with flow chemistry.

Chapter 9. Summary

The major goal of the work in this dissertation is to research the late transition elements of Co and Fe by taking a step back to perform non-conventional ways to synthesize these elements into nanomaterials. The non-conventional routes used for this magnetic nanomaterial research, involved high throughput experimentation focused on in section 1. This is a synthetic practice routinely limited to industrial usage; however, the availability of a process reactor, capable of producing 10 simultaneous reactions were available, allowed for high throughput. In section 2, continuous flow chemistry routes using two sub-types were employed, a microfluidic reactor and a large-scale modified CF assembly, which allow for further study of these magnetic nanomaterials.

As mentioned above, the work of this dissertation was centered on researching primarily Fe and Co nanomaterial synthesis to garnering a deeper understanding of their magnetic properties. In almost every chapter, unusual synthetic approaches or novel routes, based on re-engineering principles, are highlighted for producing magnetic nanomaterials. By usage of these approaches, several goals and morphological findings were achieved and are summarized below.

- 1.) Knowledge was acquired on the reaction factors that dominate phase control of cobalt ferrite and FeCo alloy. The chemistry was controlled to synthesis pure phase FeCo alloy with high magnetization saturation values. In addition, consistency from batch to batch in magnetic properties was demonstrated, gaining a further understanding for the synthetic chemist for synthesizing these magnetic nanomaterials.
- 2.) Discovery of a novel high aspect ratio geometry of pure phase FeCo alloy was performed. The synthesis of this structure was elucidated as FeCo nuclei forming growth into linear chains, locking each particle segment by their interfaces forming the linear morphologies. In addition, continuous microwire formation was realized of the FeCo

linear chains through annealing, a common treatment for processing and compaction of magnetic powders into magnets. The high aspect ratio FeCo chains are suitable as precursors for nanocrystalline amorphous alloys which require high Curie points and high saturation induction values.

- 3.) Nucleation agents such as Ag, Ru and Pt were used to control physical properties of FeCo chains such as diameter (nm) and crystallite size (nm) using the polyol process. The Ag provided the most tailorability of diameter and was therefore used in a DOE study to determine factors that control the FeCo phase, diameter, crystallite size and morphology.
- 4.) Cobalt ferrite (CFO) high aspect ratio geometries were realized by using trimethylene glycol as a solvent in the polyol process. This was the next research goal immediately after achieving the high aspect ratio morphologies of the FeCo alloy. These interesting CFO linear assemblies were observed to be nanostructured assemblies of CFO NPs under TEM with many particles possessing sizes in the superparamagnetic regime. The CFO exhibit a magneto-birefringence effect from magnetically induced optical anisotropy observable via UV-vis studies. The CFO MPs show promise for several new optical applications including light modulators and optical switches to ferro-fluids for bearing seals and loudspeakers.
- 5.) Cobalt nanoparticles were synthesized for the first time using continuous flow chemistry. The nanoparticle possessed high magnetization up to 125 emu/g and were produced at a rate exceeding 1g/hr using the ethanol hydrazine alkaline system. This CF approach demonstrates efficient production of highly magnetic Co NPs, a viable approach for industrial scale-up.

6.) FeCo alloy was successfully synthesized using a well-designed continuous flow apparatus based on the similar polyol chemistry method as discussed previously in the early chapters. The synthesis of pure phase FeCo was not attainable giving a maximum of 20 % FeCo alloy by XRD. The remainder of the composition was confirmed to be CFO. By finding a suitable alternative that avoids H₂O introduction, pure phase FeCo nanomaterials may be synthesized having tunable magnetic properties thru judicious control of the precursor flow rates.

High aspect ratio geometries of both pure phase FeCo and cobalt ferrite were achieved. Though often serendipitous at times, demonstration of morphological control using bottom-up wet-chemical methods was performed, garnering an appreciable understanding of the mechanism as well as the magnetic, structural and physical properties along the way. Exploration into synthesis of ferromagnetic nanoparticles via continuous methods was also performed opening up avenues for future continuous synthetic work of simple magnetic elements along with their binary and ternary alloys. Perhaps soon, magnetic nanomaterial syntheses will incorporate flow rate recipes which are tailored toward the extrinsic magnetic properties desired.

List of References

- (1) Miyazaki, T. *The physics of ferromagnetism*; Heidelberg ; New York : Springer: Heidelberg ; New York, 2012.
- (2) Bozorth, R. M. *Ferromagnetism*; New York : Van Nostrand: New York, 1951.
- (3) Martin, D. H. *Magnetism in solids*; London, Iliffe: London, 1967.
- (4) Stefanita, C.-G. *From bulk to nano : the many sides of magnetism*; Berlin ; London : Springer: Berlin ; [London], 2008.
- (5) Leslie-Pelecky, D. L.; Rieke, R. D. *Chem. Mater.* **1996**, *8*, 1770.
- (6) Guimarães, A. P. *Principles of nanomagnetism*; Heidelberg Germany ; New York : Springer: Heidelberg [Germany] ; New York, 2009.
- (7) Myohga, O.; Igarashi, H.; Kubo, Y. *Journal of Applied Physics* **1985**, *57*, 4164.
- (8) Long, G. J.; Grandjean, F. *Supermagnets, hard magnetic materials*; Dordrecht ; Boston : Kluwer Academic Publishers : Published in cooperation with NATO Scientific Affairs Division: Dordrecht ; Boston, 1991.
- (9) Zhdanova, O.; Lyakhova, M.; Pastushenkov, Y. *Phys. Metals Metallogr.* **2013**, *114*, 553.
- (10) Ikuo Ohnuma; Hirotohi Enoki; Osamu Ikeda; Ryosuke Kainuma; Hiroshi Ohtanib; Bo Sundman; Ishida, K. *Acta Materialia* **2002**, *50*, 379.
- (11) McHenry, M. E. W., M. A. and Laughlin, D. E. *Progress in Materials Science* **1999**, *44*, 291.
- (12) Feng, W. C.; Li, W.; Liu, X. M.; Liu, T.; Li, X. M. *Journal of Magnetism and Magnetic Materials* **2007**, *310*, 2584.
- (13) Chinnasamy, C.; Malallah, Y.; Jasinski, M. M.; Daryoush, A. S. *Applied Surface Science* **2015**, *334*, 58.
- (14) Johnson, F.; Hughes, P.; Gallagher, R.; Laughlin, D. E.; McHenry, M. E.; Willard, M. A.; Harris, V. G. *Magnetics, IEEE Transactions on* **2001**, *37*, 2261.
- (15) Herzer, G. *IEEE TRANSACTIONS ON MAGNETICS* **1990**, *26*.
- (16) Herzer, G. *IEEE TRANSACTIONS ON MAGNETICS* **1989**, *25*.
- (17) Peng, D.; Wang, X.; Wang, W.; Yue, G.; Chen, Y.; Hihara, T.; Sumiyama, K. *Science in China Series E (Technological Sciences)* **2010**, *53*, 1501.
- (18) Herzer, G. *Journal of Magnetism and Magnetic Materials* **1992**, *112*.
- (19) Herzer, G. *Scripta Metallurgica* **1995**, *33*.
- (20) Bez, R.; Zehani, K.; Boutahar, A.; Elamiri, A.; Hlil, E. K.; Lassri, H.; Moscovici, J.; Mliki, N.; Bessais, L. *Journal of Superconductivity and Novel Magnetism* **2015**, *28*, 3439.
- (21) Fernand Fievet, F. F.-V., Jean-Pierre Lagier, Bernard Dumontb; Figlarzb, a. M. *J. Mater. Chem. C* **1993**, *3*.
- (22) Joseyphus, R. J.; Matsumoto, T.; Takahashi, H.; Kodama, D.; Tohji, K.; Jeyadevan, B. *Journal of Solid State Chemistry* **2007**, *180*, 3008.
- (23) Matsumoto, T.; Takahashi, K.; Kitagishi, K.; Shinoda, K.; Cuya Huaman, J. L.; Piquemal, J.-Y.; Jeyadevan, B. *New Journal of Chemistry* **2015**, *39*, 5008.
- (24) Cho, U. R.; Lee, Y. M.; Kumar, S.; Lee, C. G.; Koo, B. H. *Science in China Series E: Technological Sciences* **2009**, *52*, 19.
- (25) Uk-Rae Cho, K. W., Geun-Woo Kim and Bon-Heun Koo *Journal of Material Science and Technology* **2010**, *26*.
- (26) Cuncheng Li; Kevin L. Shuford; Minghai Chen; Eun Je Lee; Cho, a. S. O. *Nanoletters* **2008**, *2*.
- (27) Zehani, K.; Bez, R.; Moscovici, J.; Mazaleyrat, F.; Mliki, N.; Bessais, L. *IEEE Transactions on Magnetics* **2014**, *50*, 1.

- (28) F. FIEVET, J. P. L., B. BLIN *Solid State Ionics* **1989**, 32.
- (29) Kodama, D.; Shinoda, K.; Sato, K.; Sato, Y.; Tohji, K.; Jeyadevan, B. **2007**, 898, 126.
- (30) B. Jeyadevan, K. S., K. Sato, Y. Sato and K. Tohji *Intermag* **2006**.
- (31) Dong, H.; Chen, Y. C.; Feldmann, C. *Green Chem.* **2015**, 17, 4107.
- (32) F. FIEVET, J. P. L., B. BLIN *Solid State Ionics* **1989**, 32, 198.
- (33) Fiévet, F.; Brayner, R. **2013**, 1.
- (34) Willard, M. A.; Kurihara, L. K.; Carpenter, E. E.; Calvin, S.; Harris, V. G. *International Materials Reviews* **2004**, 49, 125.
- (35) Carroll, K. J.; Reveles, J. U.; Shultz, M. D.; Khanna, S. N.; Carpenter, E. E. *The Journal of Physical Chemistry C* **2011**, 115, 2656.
- (36) Feldmann, C. *Adv. Func. Mater.* **2003**, 13.
- (37) SANDERS, F. B. L. C. A. J. K. M. *Acc. Chem. Res.* **2011**.
- (38) Watts, P.; Haswell, S. J. *Current Opinion in Chemical Biology* **2003**, 7, 380.
- (39) Kodadek, T. *Chem Commun (Camb)* **2011**, 47, 9757.
- (40) McMullen, J. P.; Jensen, K. F. In *Annu. Rev. Anal. Chem.* 2010; Vol. 3, p 19.
- (41) Clifford, D. M.; El-Gendy, A. A.; Lu, A. J.; Pestov, D.; Carpenter, E. E. *Journal of Flow Chemistry* **2014**, 4, 148.
- (42) McQuade, D. T.; Seeberger, P. H. *J Org Chem* **2013**, 78, 6384.
- (43) Michael Köhler, J.; Kraus, I.; Faerber, J.; Serra, C. *Journal of Materials Science* **2012**, 48, 2158.
- (44) Hafermann, L.; Köhler, J. M. *Chemical Engineering & Technology* **2015**, 38, 1138.
- (45) Abou Hassan, A.; Sandre, O.; Cabuil, V.; Tabeling, P. *Chemical Communications* **2008**, 1783.
- (46) Marre, S.; Jensen, K. F. *Chemical Society Reviews* **2010**, 39, 1183.
- (47) Yang, C.-H.; Wang, C.-Y.; Huang, K.-S.; Kung, C.-P.; Chang, Y.-C.; Shaw, J.-F. *International Journal of Pharmaceutics* **2014**, 463, 155.
- (48) Holladay, J. D.; Wang, Y.; Jones, E. *Chemical reviews* **2004**, 104, 4767.
- (49) García-Otero, J.; Porto, M.; Rivas, J. *Journal of Applied Physics* **2000**, 87, 7376.
- (50) Haffer, S.; Walther, T.; Köferstein, R.; Ebbinghaus, S. G.; Tiemann, M. *The Journal of Physical Chemistry C* **2013**, 117, 24471.
- (51) Ajroudi, L.; Villain, S.; Madigou, V.; Mliki, N.; Leroux, C. *Journal of Crystal Growth* **2010**, 312, 2465.
- (52) Goodarz Naseri, M.; Saion, E. B.; Abbastabar Ahangar, H.; Shaari, A. H.; Hashim, M. *Journal of Nanomaterials* **2010**, 2010, 1.
- (53) Kamali, S.; Pouryazdan, M.; Ghafari, M.; Itou, M.; Rahman, M.; Stroeve, P.; Hahn, H.; Sakurai, Y. *Journal of Magnetism and Magnetic Materials* **2016**, 404, 143.
- (54) Zhang, Y.; Liu, Y.; Fei, C.; Yang, Z.; Lu, Z.; Xiong, R.; Yin, D.; Shi, J. *Journal of Applied Physics* **2010**, 108, 084312.
- (55) Bi, Y.; Ren, Y.; Bi, F.; He, T. *Journal of Alloys and Compounds* **2015**, 646, 827.
- (56) Herrera, A. P.; Polo-Corrales, L.; Chavez, E.; Cabarcas-Bolivar, J.; Uwakweh, O. N. C.; Rinaldi, C. *Journal of Magnetism and Magnetic Materials* **2013**, 328, 41.
- (57) A. A. Vostrikov, A. V. S., O. N. Fedyaeva, M. Ya. Sokol, and A. V. Zaikovskii *Russian Chemical Bulletin* **2012**, 61.
- (58) Grosvenor, A. P.; Kobe, B. A.; McIntyre, N. S. *Surface Science* **2004**, 572, 217.
- (59) May, J. E.; de Oliveira, M. F.; Kuri, S. E. *Materials Science and Engineering: A* **2003**, 361, 179.
- (60) Balela, M. D. L.; Yagi, S.; Matsubara, E. *Journal of The Electrochemical Society* **2011**, 158, D210.

- (61) López-Ruiz, R.; Magén, C.; Luis, F.; Bartolomé, J. *Journal of Applied Physics* **2012**, *112*, 073906.
- (62) Li, M.; Xie, K.; Wu, Y.; Yang, Q.; Liao, L. *Materials Letters* **2013**, *111*, 185.
- (63) A. L. Elias, J. A. R.-M., M. R. McCartney, D. Golberg, A. Zamudio, S. E. Baltazar, F. L.-U., E. Munoz-Sandoval, L. Gu, C. C. Tang, D. J. Smith, Y. B., H. Terrones, and M. Terrones *Nanoletters* **2005**, *5*.
- (64) Farghaly, A. A.; Huba, Z. J.; Carpenter, E. E. *Journal of Nanoparticle Research* **2012**, *14*.
- (65) Takagaki, Y.; Herfort, J.; Ploog, K. H. *Journal of Applied Physics* **2005**, *98*, 093901.
- (66) Huba, Z. J.; Carroll, K. J.; Carpenter, E. E. *Journal of Applied Physics* **2011**, *109*, 07B514.
- (67) Jianmin, B.; Yun-Hao, X.; Jian-Ping, W. *IEEE Transactions on Magnetism* **2007**, *43*, 3340.
- (68) Sundar, R. S.; Deevi, S. C. *International Materials Reviews* **2005**, *50*, 157.
- (69) Bottauscio, O. G., S.; Zucca, M.; Chiampi, M. *IEEE Transactions on Magnetism* **2014**, *50*.
- (70) Azzaza, S.; Alleg, S.; Moumeni, H.; Nemamcha, A. R.; Rehspringer, J. L.; Greneche, J. M. *Journal of Physics: Condensed Matter* **2006**, *18*, 7257.
- (71) Laala-Bouali, H.; Bentayeb, F. Z.; Loudi, S.; Guo, X.; Tria, S.; Suñol, J. J.; Escoda, L. *Advanced Powder Technology* **2013**, *24*, 168.
- (72) Carta, D.; Mountjoy, G.; Gass, M.; Navarra, G.; Casula, M. F.; Corrias, A. *J Chem Phys* **2007**, *127*, 204705.
- (73) Dong, L.; Liu, S.; Gao, H.; Ding, N.; Tremel, W.; Xiong, C.; Zhu, Q.; Knoll, W. *Small* **2009**, *5*, 1153.
- (74) Mishra, S. R.; Dickey, M. D.; Velez, O. D.; Tracy, J. B. *Nanoscale* **2016**.
- (75) Leardi, R. *Anal Chim Acta* **2009**, *652*, 161.
- (76) Yang, X. T. a. H. *J Am Chem Soc* **2003**, *125*.
- (77) SARA E. SKRABALAK, J. C., † YUGANG SUN,†; XIANMAO LU, L. A., † CLAIRE M. COBLEY,‡ AND; XIA, Y. *Acc. Chem. Res.* **2008**, *41*.
- (78) Yue, H.; Zhao, Y.; Ma, X.; Gong, J. *Chem Soc Rev* **2012**, *41*, 4218.
- (79) Clifford, D. M.; Castano, C. E.; Lu, A. J.; Carpenter, E. E. *J. Mater. Chem. C* **2015**, *3*, 11029.
- (80) Larcher, D.; Patrice, R. *Journal of Solid State Chemistry* **2000**, *154*, 405.
- (81) Dunin-Borkowski, R. E.; Kasama, T.; Wei, A.; Tripp, S. L.; Hýtch, M. J.; Snoeck, E.; Harrison, R. J.; Putnis, A. *Microscopy Research and Technique* **2004**, *64*, 390.
- (82) Tripp, S. L.; Dunin-Borkowski, R. E.; Wei, A. *Angewandte Chemie International Edition* **2003**, *42*, 5591.
- (83) Wei, A.; Kasama, T.; Dunin-Borkowski, R. E. *Journal of Materials Chemistry* **2011**, *21*, 16686.
- (84) Cunha, I. T.; Teixeira, I. F.; Albuquerque, A. S.; Ardisson, J. D.; Macedo, W. A. A.; Oliveira, H. S.; Tristão, J. C.; Sapag, K.; Lago, R. M. *Catalysis Today* **2016**, *259*, 222.
- (85) Dai, Q.; Berman, D.; Virwani, K.; Frommer, J.; Jubert, P. O.; Lam, M.; Topuria, T.; Imaino, W.; Nelson, A. *Nano Lett* **2010**, *10*, 3216.
- (86) *Magnetism, IEEE Transactions on* **2013**, *49*, 467.
- (87) Carpenter, E. E. *Journal of Magnetism and Magnetic Materials* **2001**, *225*, 17.
- (88) John, L. S. *Physics Today* **1995**, *48*, 26.
- (89) Liu, H. J.; Tra, V. T.; Chen, Y. J.; Huang, R.; Duan, C. G.; Hsieh, Y. H.; Lin, H. J.; Lin, J. Y.; Chen, C. T.; Ikuhara, Y.; Chu, Y. H. *Adv Mater* **2013**, *25*, 4753.
- (90) M. Grigorova, H. J. B., V. Blaskov, V. Rusanov, V. Petkov, V. Masheva, D. Nihtianova, L. M. M., J.S. Munoz and M. Mikhov *Journal of Magnetism and Magnetic Materials* **1998**, *183*, 163—172.
- (91) J.P. Vejpravovz, V. S. *WDS'05 Proceedings of Contributed Papers* **2005**, *3*.
- (92) Kim, D. K.; Zhang, Y.; Voit, W.; Rao, K. V.; Muhammed, M. *Journal of Magnetism and Magnetic Materials* **2001**, *225*, 30.
- (93) Yoon, S. *Journal of Magnetism and Magnetic Materials* **2012**, *324*, 2620.

- (94) Che, R. C.; Zhi, C. Y.; Liang, C. Y.; Zhou, X. G. *Applied Physics Letters* **2006**, *88*, 033105.
- (95) Schulten, P. C. *IEEE Transactions on Magnetics* **1980**, *2*.
- (96) Lin, J.-F.; Lee, M.-Z. *Optics Communications* **2012**, *285*, 1669.
- (97) Lin, J.-F. *Optik - International Journal for Light and Electron Optics* **2010**, *121*, 2144.
- (98) Yi Li *, C. P., D. Riegel *Journal of Magnetism and Magnetic Materials* **1997**, *165*.
- (99) Wang, J.; Albina, J.-M.; Iwasaki, T.; Moriya, H.; Umeno, Y. *Journal of Materials Research* **2013**, *28*, 1559.
- (100) Shishkina, L.; Lokshtanova, O.; Karabanov, S. *Coatings* **2012**, *2*, 1.
- (101) Song, Y.; Jin, P.; Zhang, T. *Materials Letters* **2010**, *64*, 1789.
- (102) Kuo, J. *Electron microscopy methods and protocols*; 3rd ed. / edited by John Kuo.. ed.; New York : Humana Press : Springer: New York, 2014.
- (103) Kothleitner, G.; Schaffer, B. *Microscopy and Microanalysis* **2007**, *13*, 156.
- (104) Shea, J. J. USA, 2003; Vol. 19, p 73.
- (105) Biesinger, M. C.; Payne, B. P.; Grosvenor, A. P.; Lau, L. W. M.; Gerson, A. R.; Smart, R. S. *Applied Surface Science* **2011**, *257*, 2717.
- (106) Barr, T. *Journal of Physical Chemistry* **1978**, *82*, 1801.
- (107) Péter, L.; Csik, A.; Vad, K.; Tóth-Kádár, E.; Pekker, Á.; Molnár, G. *Electrochimica Acta* **2010**, *55*, 4734.
- (108) Yaacob, I. I.; Nunes, A. C.; Bose, A.; Shah, D. O. *Journal of Colloid And Interface Science* **1994**, *168*, 289.
- (109) Crangle, J. *The magnetic properties of solids*; London : Edward Arnold: London, 1977.
- (110) Sara E. Skrabalak, ‡ Benjamin J. Wiley, †, § Munho Kim, | Eric V. Formo, |; Xia*, a. Y. *Nanoletters* **2008**, *8*.

Vita

Dustin Michael Clifford was born in Temple, TX and grew up in the Rio Grande Valley of South Texas. He earned his Bachelors of Science in Chemistry at Baylor University in 2007. From 2008-2011 he worked for Allergan as a chemistry laboratory technician testing prescription ophthalmics in quality control. He moved to Richmond, VA in 2011 and began working for Pharmaceutical Product Development (PPD) as a technical trainer. Shortly thereafter, he began pursuing his Ph. D. at Virginia Commonwealth University. He joined Prof. Carpenter's Research Lab in 2012 and began working as a research associate at VCU's Nanomaterial Characterization Center (NCC) in 2013 until graduating in 2016 with a Ph. D. in Nanoscience and Nanotechnology.